THE FRACTURED ICE SHELL OF SATURN'S MOON ENCELADUS: INSIGHTS INTO
THE GLOBAL STRESS HISTORY AND INTERIOR STRUCTURE

A Dissertation

Presented in Partial Fulfillment of the Requirements for the

Degree of Doctorate of Philosophy

with a

Major in Geology

in the

College of Graduate Studies

University of Idaho

by

Emily S. Martin

May 2014

Major Professor: Simon A. Kattenhorn, Ph. D.

Authorization to Submit Dissertation

This dissertation of Emily S. Martin, submitted for the degree of Doctor of Philosophy with a major in Geology and titled "The fractured ice shell of Saturn's moon Enceladus: Insights into the global stress history and interior structure," has been reviewed in final form. Permission, as indicated by the signatures and dates below, is now granted to submit final copies to the college of Graduate Studies for approval.

Major Professor: _____ Date: _____
        Dr. Simon A. Kattenhorn

Committee
Members: _____ Date: _____
        Dr. Leslie L. Baker

_____ Date: _____
        Dr. Gwen D. Barnes

_____ Date: _____
        Dr. Jerry P. Fairley

Department
Administrator: _____ Date: _____
        Dr. Mickey E. Gunter

Discipline's
College Dean: _____ Date: _____
        Dr. Paul Joyce

Final Approval and Acceptance

Dean of the College
Of Graduate Studies: _____ Date: _____
        Dr. Jie Chen

Abstract

The warm south polar terrain (SPT) and associated plume activity make Enceladus an exciting target for astrobiological research. Previous work on Enceladus has focused almost exclusively on the geologically active SPT, however, to understand the Enceladus system as a whole, a complete history of the geologic processes that have shaped Enceladus through time must be resolved. With this work, I look at the global stress history on Enceladus by focusing on the recent tectonic dissection of the cratered terrains by features called pit chains. I assess the global distribution of pit chains and find that they fall into 7 unique sets with distinct orientations consistent with sequential formation in an nonsynchronous rotation stress field which implies a global liquid ocean rather than a regional south polar sea. I present a new mechanism for the unique way in which craters and pit chains interact on Enceladus by modeling additional heat generated from an impact event in a thermally unstable ice shell creating a localized zone of rising warm ice beneath a crater. Results suggest that it is the relative amounts of differential stress and fluid pressure that dictates crater-fracture interactions. I show that pit chains are among the youngest tectonic features on Enceladus's surface and that they can be used to directly infer regolith thickness across these terrains. The distribution pit depths (inferred from pit diameter and slope angles) indicate a heterogeneous distribution of regolith thicknesses across the surface. Finally we use secondary fractures, tailcracks and en echelon cracks, to identify strike-slip faults on Enceladus, and produce the first ever global map of strike-slip fault distributions on Enceladus. Additionally find that strike-slip faults fall into three classes: tectonic domain boundaries, reactivated linear features, and primary strike-slip faults. Their distributions and sense of slip are inconsistent with having formed due to a nonsynchronous rotation stress field which has been previously attributed to the formation of fracture patterns within the south polar terrain and pit chains in the cratered terrains. This result reveals that additional mechanisms are driving fracture formation on the surface of Enceladus.

Acknowledgements

It takes a village to inspire and produce a dissertation and I have been fortunate to be surrounded and encouraged by a truly influential support system. Compiling a list of those who have helped me achieve my goals is overwhelming and humbling to say the least. First, I want to thank and acknowledge the guidance of Simon Kattenhorn, my major professor. Simon was the advisor I needed. He identified and nurtured my weaknesses, but also encouraged and enhanced my strengths. I was introduced to Simon (and to planetary science) by my undergraduate professor Geoff Collins, whose mentorship and guidance has been invaluable and grounding. Thank you Simon and Geoff for the instrumental rolls you played in my life and education.

I would like to thank the members of my committee: Leslie Baker, Gwen Barnes, and Jerry Fairley. I would also like to thank John Watkinson who sat on my committee during my proposal defense. They all provided valuable insights and guidance throughout my time at the University of Idaho.

I joined the Geomechanics Research Group during the time when Jon Kay, Jane Barnes, Rachel (Daly) Hobbs, June Clevy, Matt Blakeslee, and Alex Patthoff made up a cohesive and supportive unit. There was a special bond within the Geomechanics Research Group, only to be improved upon by the addition of Amy McMillan, Matt Pendleton, James Muirhead, and Alexa Van Eaton (honorary). I can't emphasize enough how grateful I was for the dynamism, camaraderie, and energy within this group and how it contributed to my success. I especially want to thank Alex Patthoff for innumerable brainstorming sessions, pep-talks, collaborations, and technical support with ArcGIS and ISIS. Amanda Nahm, the newest addition to the Geomechanics group, spent many hours editing manuscripts, proposals, all of my thesis chapters, and silly questions.

Thank you to the Planetary Science Journal Club, especially Casey Cook, Shannon (Mackenzie) France, and Graham Vixie. Planetary science at the University of Idaho is interdepartmental, and these three in particular were influential in supporting me through my dissertation.

I'd like to thank the Department of Geological Sciences at the University of Idaho for their support, especially Mickey Gunter and Debbie Jensen for helping me to navigate the often-complicated logistics that accompany graduate school.

Table of Contents

ix

List of Figures

List of Tables

Chapter 1

Geologically recent ice shell deformation above a global ocean on Enceladus

Abstract

We report the detection of tectonic dissection of the cratered terrains of Enceladus and present a detailed global map of fractures that formed antipodal, systematic sets. The fracture sets have distinct orientations consistent with sequential formation in a temporally changing stress field. The orientations vary through time in a manner consistent with nonsynchronous rotation of the ice shell about its interior. This rotation implies a global, rather than regional, liquid ocean beneath the ice shell, making Enceladus an important target for future astrobiological studies.

1.1 Introduction

Although the old cratered terrains on Enceladus have been historically overlooked as being tectonized, they are pervasively dissected by geologically recent fracture systems called pit chains (Fig. 1.1), which are unique to Enceladus in the outer solar system [*Michaud et al.,* 2008; *Martin & Kattenhorn,* 2013; 2014]. Fracture patterns described within Enceladus's south polar terrain [*Patthoff & Kattenhorn,* 2011] comprise four systematic fracture sets with distinct orientations that are attributed to a changing global stress field. A strong candidate for this stress pattern is nonsynchronous rotation (NSR),
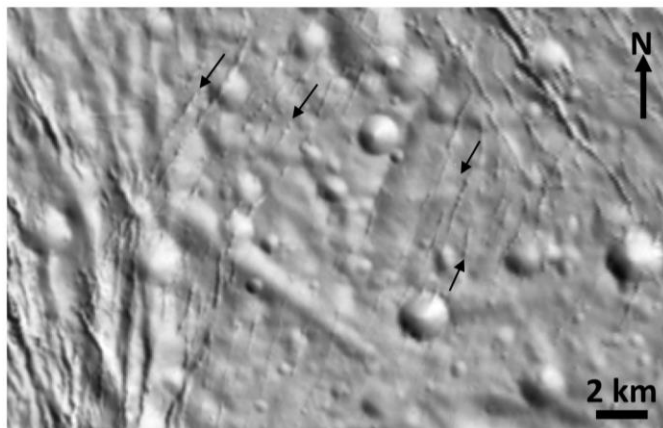
Figure 1.1: A region within the cratered terrains on Enceladus (centered at 150°E 8°N). Pit chains are indicated by arrows, showing chains of isolated to partially merged pits. Cassini ISS image N1489050144.

whereby a decoupled ice shell rotates faster than the solid interior over long time scales, and which implies a global subsurface ocean [*Patthoff & Kattenhorn,* 2011]. Comparatively, a

global ocean is hypothesized to exist beneath the ice shell of Europa based upon (among other lines of evidence) the analysis of fracture patterns [*e.g. McEwen,* 1986; *Hoppa et al.,* 1999, 2001], some of which may be related to NSR [*Kattenhorn,* 2002; *Figueredo & Greeley,* 2000; *Groenleer & Kattenhorn,* 2008].

Analysis of the pattern of fractures within ice shells is a robust technique for resolving the stress field in which they formed. With the exception of *Patthoff & Kattenhorn* [2011], there is no documented geologic evidence for a global ocean on Enceladus. A regional ocean, first suggested by *Collins & Goodman* [2007], could explain the measured south polar negative mass anomaly but this observational evidence cannot rule out a global ocean [*Iess et al.,* 2014]. Reconciling a global or local ocean hypothesis is important for resolving the source of the material for the plume activity in the SPT, the internal structure and evolution of Enceladus, and its astrobiological potential.

We aim to map the global distribution of pit chains on the surface of Enceladus and determine by which global stress mechanism they likely formed. We then assess the implications of the resulting formation mechanisms and its implications for the global geologic history of Enceladus.

1.2 Background

Enceladus's surface can be broadly separated into three terrain types: the south polar terrain (SPT), the tectonized terrains in the leading and trailing hemispheres, and the cratered terrains in the Saturn and anti-Saturn hemispheres (Fig. 1.2). The SPT is bounded by the south polar dichotomy, or the southern curvilinear terrain [*Crow-Willard & Pappalardo,* 2010; *Patthoff & Kattenhorn,* 2011], composed primarily of scarp complexes and corrugated ridges [*Nahm & Kattenhorn,* 2014]. Within the SPT, four prominent fractures called 'tiger stripes' [*Porco et al.,* 2006] are the source of the plume activity [*Spitale & Porco,* 2007] and are associated with the south polar thermal anomaly [*Porco et al,* 2006; *Spencer et al.,* 2006]. The ongoing geologic activity and dearth of craters in the SPT suggest that these terrains are extremely young [*Porco et al.,* 2006]. Similarly, the lack of craters within the tectonized terrains indicates that they are also likely young, on the order of 0.2–2 Ga [*Kirchoff & Schenk,* 2009]. The cratered terrains are considered to be ancient terrains (0.6-4.6 Ga [*Kirchoff & Schenk,* 2009]) due to the highest crater densities. We will show that the cratered

terrains have been tectonized recently by pit chain fracture sets, in a different way than the whole-scale tectonic resurfacing experienced by the tectonized terrains.
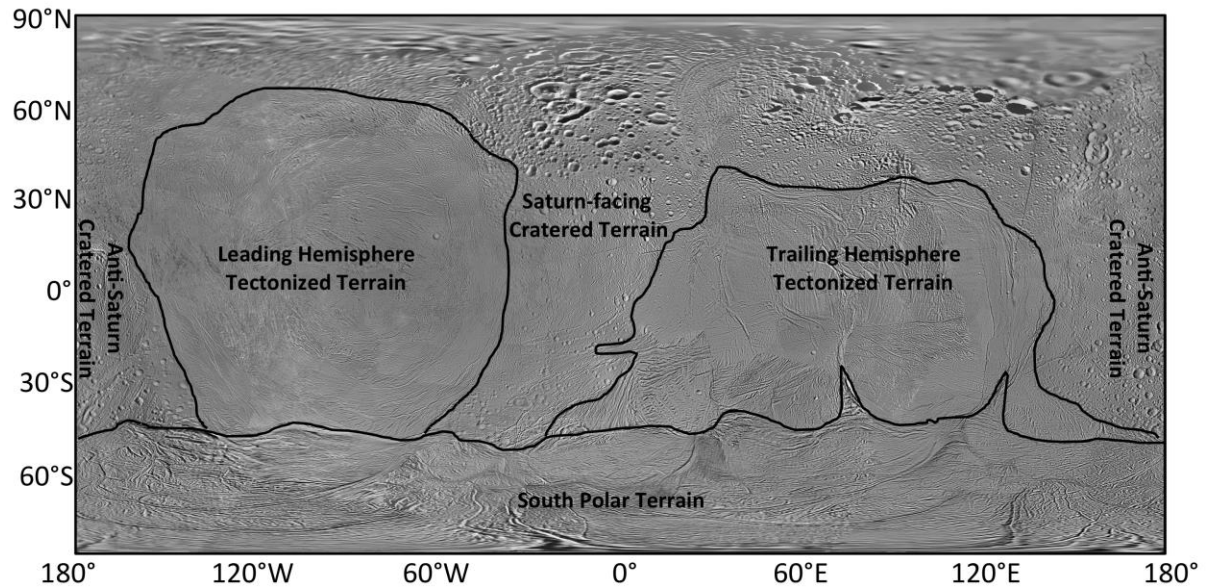
Figure 1.2: Three broad surface terrain types of Enceladus. The south polar terrain is bounded by the south polar dichotomy. The tectonized terrains are in the leading and trailing hemispheres, whereas the cratered terrains are in the Saturn-facing and anti-Saturn hemispheres. Image credit: NASA/JPL-Caltech/SSI. Mosaic by *Roatsch et al.* [2013].

1.2.1 Pit chains

Pit chains (Fig. 1.1) are among the youngest features on Enceladus outside of the SPT [*Michaud et al.* 2008; *Martin & Kattenhorn*, 2013, 2014]. Detailed observations of pit chains and analog models show that they form by the drainage of loose material into a void formed by tension cracking or dilational faulting [*Michaud et al.,* 2008; *Wyrick et al.,* 2004; *Ferrill et al.,* 2004]. Therefore, the orientation of a pit chain is indicative of the orientation of the principal stresses at the time of formation. If there is a discrepancy between the orientation of a pit chain and a candidate stress field, it is likely that the pit chain did not form at that longitude. They are found predominantly within the cratered terrains, but have also been observed crosscutting tectonized terrains and the south polar dichotomy [*Martin & Kattenhorn,* 2013, 2014]. Pit chains take on a variety of morphologies, dictated by how much dilation the underlying fracture has experienced [*Ferrill et al.,* 2004], starting as isolated pits and ending as fully merged pit chains that form characteristic troughs with scalloped rims [*Wyrick et al.,* 2004; *Ferrill et al.,* 2004]. Individual pit chains are highly segmented features

that can be found to represent all aforementioned morphologies within close proximity. Diameters of individual, isolated pits range in size from 0.01–1 km. Regolith on the surface of Enceladus is primarily sourced from fall-back material from the plumes, but may also include E-ring material as well as impact-generated regolith [*Bland et al.,* 2012; *Kirchoff & Schenk*, 2009].

1.2.2 Global Stress Fields and Interior Structure

Icy shells can preserve a record of tectonic deformation in patterns of fractures. Large-scale tectonic deformation of icy shells may be in response to stresses caused by true polar wander, despinning, changes in volume caused by freezing or thawing of a subsurface ocean, orbital recession/decay, diurnal tidal forcing, and nonsynchronous rotation (NSR) [*Collins et al.,* 2010*; Kattenhorn & Hurford,* 2009]. Each of these forcing mechanisms is associated with unique patterns of global stress. Fracture patterns can therefore be diagnostic of the stress mechanism based upon the inferred stress field within which they formed. NSR has been suggested as the likely stress mechanism responsible for forming four systematic fracture sets observed within the SPT, which show distinct set orientations that progressively changed through time [*Patthoff & Kattenhorn,* 2011].

For NSR to occur, three criteria must be met: the satellite must reside in an eccentric orbit, there can be no permanent mass asymmetry, and the ice shell must be decoupled from the inner core, likely by a global ocean [*Greenberg & Weidenschilling,* 1984]. The existence of a global liquid layer has been suggested for Jupiter's moon Europa (which meets all three criteria) based on magnetic field data [*Khurana et al.,* 1998; *Pappalardo et al.,* 1999] as well as geological lines of evidence such as crater morphologies and a variety of tectonic features [*Pappalardo et al.,* 1999]. Similarly, Enceladus meets all three criteria; however, the presence or longevity of a global ocean is difficult to sustain even with alternative chemical compositions which might lower freezing points [*Roberts & Nimmo,* 2008].

NSR is one of the few global stress mechanisms that can produce stresses large enough to overcome the tensile strength of ice. Diurnal tidal stresses on Enceladus produce stresses on the order of kilopascals [*Hurford et al.,* 2007; 2012; *Smith-Konter & Pappalardo,* 2008]. The tensile strength of ice is ~2 MPa [*Schulson & Duvall,* 2009], an order of magnitude larger than diurnal stresses. Ice shell thickening is likely the only other mechanism capable of

producing high enough stresses; however, the predicted fracture patterns would consist of a random distribution of orientations with an absence of consistent relative ages [*Collins et al.,* 2010; *Kattenhorn & Hurford,* 2009], unless superposed on an extant deviatoric stress field caused by some other forcing mechanism.

1.2 Detailed fracture mapping

1.2.1 Mapping

High-resolution Cassini Imaging Science Subsystem (ISS) camera images were obtained from the Planetary Data System (PDS) archive (40–200 m/pixel) and used to produce global maps created in an ArcGIS environment, highlighting the distribution of pit chain sets across Enceladus. Mapped fractures were assigned into sets based on their average strike orientation, with fractures in a single set having differences in strike of no more than ±5°. If a fracture did not fit within one of the established fracture sets, a new set was designated.

1.2.2 Establishing a relative age sequence

To establish a relative age sequence, crosscutting relationships were used (Fig. 1.3): in the absence of crosscutting relationships, fracture orientations were used to assign a fracture into a set. For example, for the case of opening fractures, younger fractures commonly terminate against older, pre-existing fractures (Fig. 1.3a). An older set may also be disrupted by a newer set (Fig. 1.3b), and in the case where the older fracture has completely annealed, the younger fracture can propagate across the older fracture. Similar relationships observed on Earth have been used to determine the age sequence of joint sets [e.g., *Cruikshank & Aydin*, 1992]. For each hemisphere, we made observations of stratigraphic relationships in regions where two sets were within proximity to each other. Each intersection was assigned an identifying number and confidence level (1[low] - 5 [high]) based on the quality of the crosscutting relationship. Fig. 1.3 demonstrates crosscutting relationships that warrant a confidence level of 5. Analyses of crosscutting relationships were completed independently for each hemisphere in which pit chain sets occur to eliminate bias. Because no single pit chain set intersects every other set, this approach meant that for each hemisphere, there multiple solutions for the relative age sequence that fit within the context of the observed

crosscutting relationships and their designated confidence levels. Each age sequence was evaluated independently and for each hemisphere. Although each age sequence is feasible, we selected the relative age sequence that represented the minimum amount orientation change between the oldest and youngest fracture set.
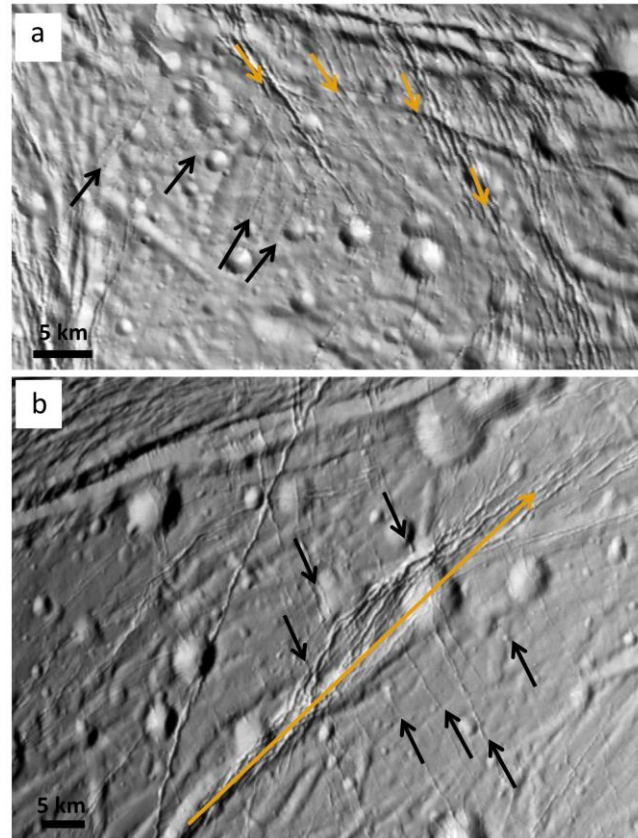
Figure 1.3: Two examples of crosscutting relationships on Enceladus. a. Two sets of pit chains with orientations highlighted by arrows. The set oriented NW-SE formed first as indicated by the younger NE-SW set terminating against the pre-existing set. Additionally, the more prominent NW-SE set is better developed than the NE-SW set suggestive of its advanced age, Cassini ISS image N1489050144 (centered at 152°E 15°N). b. Pit chains oriented NW-SE are disrupted by the formation of a newer set of pit chains oriented NE-SW. Cassini ISS image N1637465942 (centered at 5°W 14°S).

1.2.3 Modeling

We utilized the viscoelastic stress modeling program SatStressGUI [*Wahr et al.,* 2009; *Kay & Kattenhorn*, 2010] which can calculate global stress fields (including the magnitude and orientation of the maximum and minimum tensile stresses) due to nonsynchronous rotation and/or diurnal tidal stresses for a four-layer satellite. The thickness and rheological properties of each layer can be defined. We assume a global subsurface ocean underneath a thick, 86 km ice shell to produce conservative estimates of stress magnitudes. Rheological

properties of the ice shell were selected based in-line with previous work assuming a brittle upper ice shell and a thicker, more ductile lower ice shell. [*Nimmo et al.* 2007; *Smith-Konter & Pappalardo,* 2008; *Olgin et al.* 2011; *Patthoff & Kattenhonr,* 2011]. We test whether the predicted fracture patterns produced with SatStressGUI match the observed fracture patterns in order to determine the likelihood that NSR stresses were responsible for pit chain formation and orientation variability through time at specific locations on the surface of Enceladus.
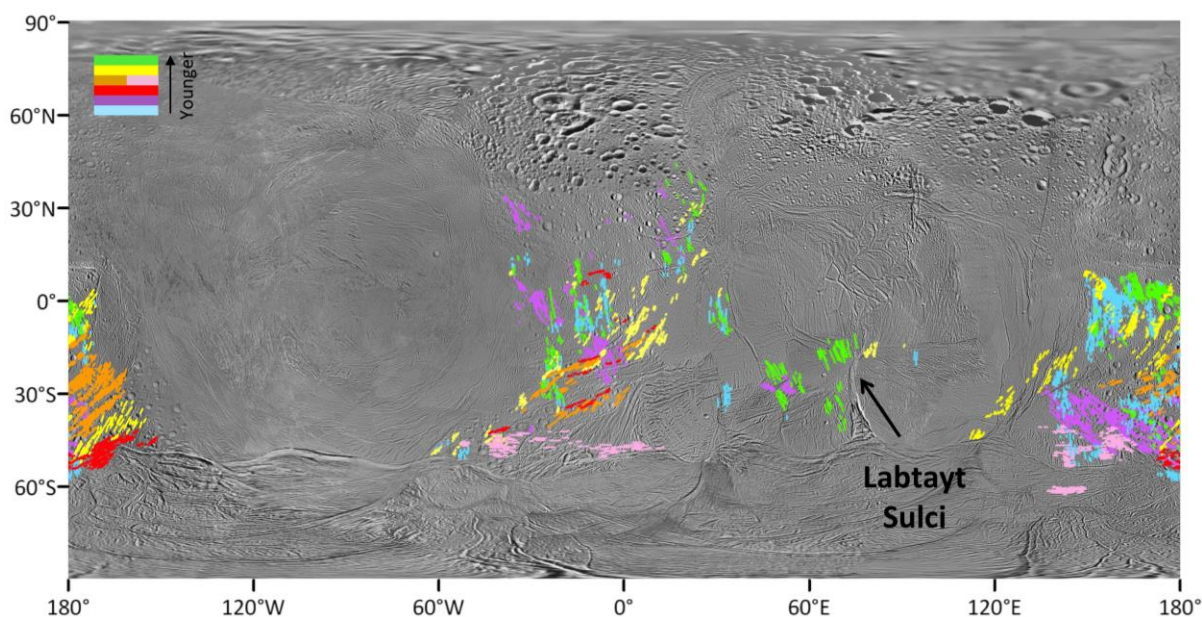
Figure 1.4: The global distribution of pit chain fracture sets overlain on the global mosaic of Enceladus. Pit chains are primarily concentrated in the cratered terrains with the exception of those near 60°E. The color of each pit chain set indicates its placement in the age sequence from oldest to youngest: blue, purple, red, orange/pink, yellow, green. Image credit: NASA/JPL-Caltech/SSI, Mosaic by *Roatsch et al.,* [2013].

1.3 Analysis of fracture sets in an NSR stress field

1.3.1 Pit chain sets and relative ages

Seven individual fracture sets with distinct orientations were observed within each of the cratered terrains (Fig. 1.4). After establishing the relative age sequence of pit chains independently within each of the anti-podal cratered terrains, we observed that sets that fell within the same place in the relative age sequence had similar orientations. For example the oldest set of pit chains on the anti-Saturn cratered terrains were roughly oriented N-S, as were the oldest pit chain set in the Saturn cratered terrains. We concluded that these two sets

are likely contemporaneous with one another. We therefore establish the unified color scheme in Fig. 1.4, in which sets of the same color (i.e., relative age) each have antipodal correlatives with the same orientation. Many sets have broad spatial extents, especially sets 5 and 6 (on both hemispheres), which cross the equator and extend into the trailing hemisphere tectonized terrain. Despite the broad spatial extent, fracture orientations are reasonably consistent in part due to the ±5° criterion established for assigning fractures in to a set.
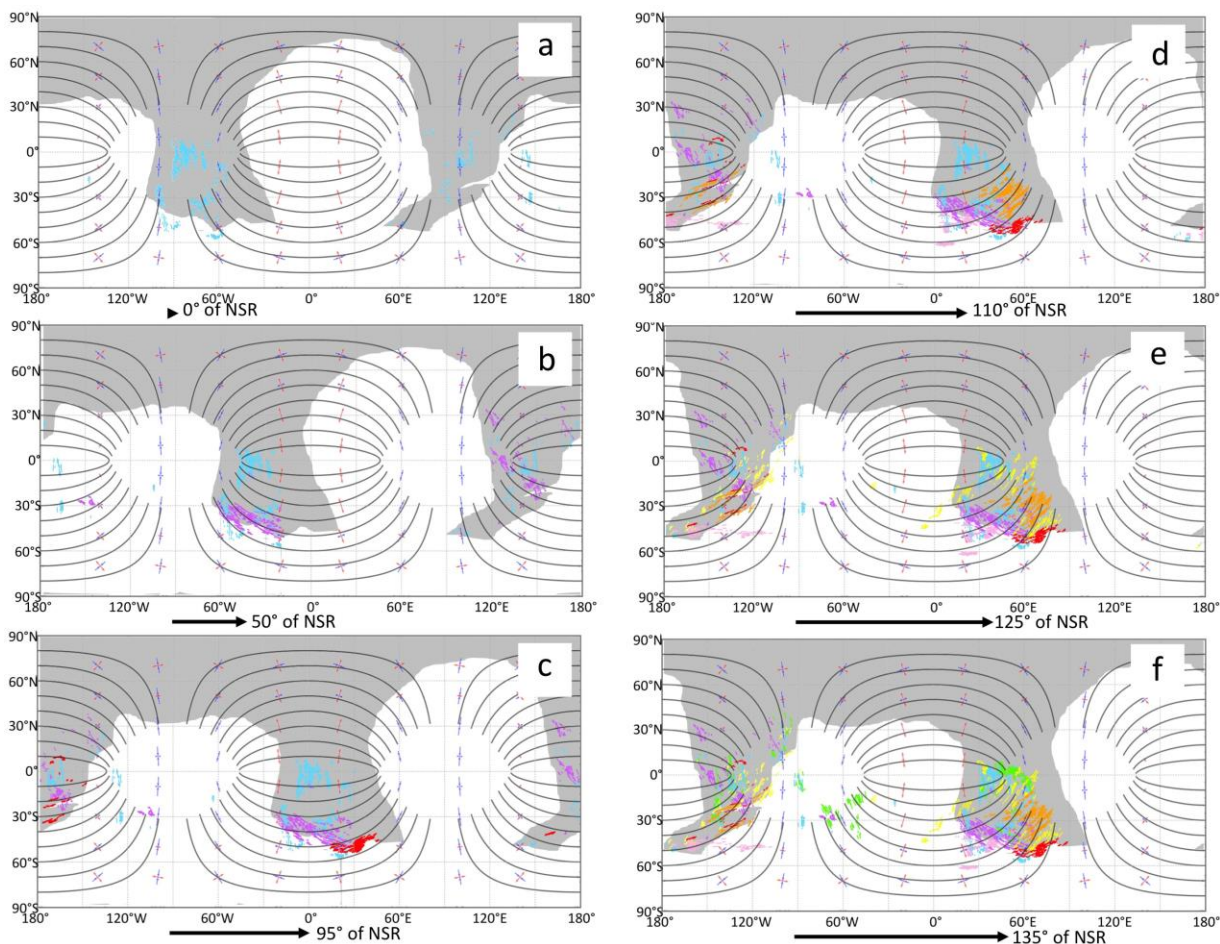
Figure 1.5: Global theoretical NSR stress field with a period of 1 Myr and predicted orientations of extension fractures (black lines). Overlays of mapped pit chain fracture sets are shown in color. The gray regions indicate the locations of the cratered terrains. Red and blue ticks indicate the orientations of the principal stresses (red is tension; blue is compression). Extension fractures form perpendicular to the maximum tension. As nonsynchronous rotation occurs, the ice shell moves toward the east relative to the longitudinal reference frame; however, the NSR stress field and predicted fracture pattern is locked to the Saturn direction. Panels a-f show sets 1 (oldest) through 6 (youngest) forming sequentially through time as the ice shell rotates eastward. Arrows beneath each panel indicate the cumulative minimum amount of shell rotation required to account for the orientations of all six fracture sets (135° of total rotation). In all panels, 0° represents the Saturn-facing direction.

1.3.2 Comparison with NSR stress fields

A theoretical NSR stress field was generated using SatStressGUI [*Wahr et al.,* 2009; *Kay & Kattenhorn, 2010] for a 1 Myr period. An NSR period of 1 Myr is consistent with the findings of *Patthoff* [2013], however NSR periods between 10 Kyr and 10 Myr produce stresses great enough to overcome the tensile strength of ice (1-3 MPa [*Schulson & Duvall,* 2009]), but a 10 Myr period approaches the viscous relaxation time at which point the stresses built up in the ice shell can relax away. Black lineaments indicate the predicted orientations of theoretical extension fractures that would form. The fractures form concentric patterns centered on the Saturn and anti-Saturn points. As NSR occurs, the ice shell will progressively migrate eastward through time, so a point on the surface moves longitudinally through the NSR whereby experiencing changes in the orientations and magnitudes of stresses with time. These lineaments were used to match the orientation of pit chain sets to determine the minimum amount of NSR that would have occurred to form all of the observed sets of pit chains. For fracture sets with broad spatial extents, the predicted global fracture pattern at a particular point in the NSR cycle cannot match all parts of a particular fracture set simultaneously. In such cases, the regions of each set with the highest fracture density were used to match against the NSR stress field in Fig. 1.5. Considering that pit chains were assigned into sets based only on their orientation, regardless of geographical location, the broad extent of some sets indicates that different portions of these sets may have formed at slightly different times during the NSR cycle.

To produce all fracture sets sequentially, Enceladus's ice shell must have rotated longitudinally a minimum of 135° relative to the solid interior of the moon. However, an additional amount of NSR is required to rotate the fracture sets into their current longitudinal positions, about 120°. Therefore 255° of total rotation is needed to form all 7 pit chain sets in their present longitudes. For comparison, *Patthoff & Kattenhorn* [2011] suggest a minimum of 153° of rotation based on changing fracture patterns in the SPT. We emphasize that our estimate is a minimum, as it is not possible to determine the exact amount of shell rotation that occurred between the formation of individual sets (given the east-west hemispheric reflection symmetry in the stress field, a match is theoretically possible at any selected match-point modulo 180°).

1.4 Discussion

Based on our mapping, crosscutting relationship analysis, and theoretical stress modeling results, NSR is a viable mechanism for forming pit chains within the cratered terrains on Enceladus. This result is independently supported by previous work in the SPT where systematic changes in fracture set orientation, including the present day tiger stripes, were observed and attributed to a changing stress field due to NSR [*Patthoff & Kattenhorn,* 2011]. The recent geologic record preserved over much of Enceladus's surface is consistent with NSR and is the only global stress mechanism that is capable of producing symmetric, contemporaneous antipodal fracture patterns in combination with sufficiently high stress magnitudes to fracture the ice shell.

Table 1.1: Summary of mapping results providing the spatial extent and average orientation for each mapped pit chain set. Color refers to fracture set color in Figs. 4 and 5. Spatial extent includes the eastern- and western-most longitudes and the southern- and northern-most latitudes. The relative ages of sets are ordered from oldest (those that occurred first) to youngest (the pit chains to form most recently).

Relative Age	Set	Color	Saturn Side		Anti-Saturn Side	
			Average Orientation	Spatial Extent	Average Orientation	Spatial Extent
Oldest ------------- Youngest	1	Blue	175°	55°W to 34°E 50°S to 25°N	180°	94°E to 171°W 58°S to 9°N
	2	Purple	135°	36°W to 54°E 42°S to 38°W	140°	138°E to 173°W 54°S to 7°S
	3	Red	75°	43°W to 9°E 43°S to 9°N	60°	171°E to 151°W 55°S to 41°S
	4/5	Orange/ Pink	45°/90°	52°W to 11°E 50°S to13°S	45°/90°	130°E to 160°W 60°S to 7°S
	6	Yellow	35°	62°W to 31°E 50°S to 31°N	30°	76°E to 155°W 52°S to 8°N
	7	Green	165°	26°W to 74°E 42°W to 40°N	165°	150°E to 173°W 48°S to 8°S

Fig. 1.5 demonstrates the interpreted series of events in which to produce the observed anti-podal pattern of pit chains (results summarized in Table 1.1). Step one shows N-S oriented pit chains forming in a region where no theoretical lineaments are predicted to form based on a tensile failure criterion that is not fulfilled. However, we assume that pit chains are likely dilational cracks above subsurface normal faults [*Wyrick et al.,* 2004; *Ferrill et al.,* 2004]. As normal faults can form in regions of compression, as predicted by NSR, the lack of the predicted tensile cracks in these regions is not inconsistent. Rather, subsurface normal faults experience dilation along the fault plane as near the surface, creating a dilational space for regolith to drain into thus forming pit chains [*e.g. Grant & Kattenhorn,* 2004]. The next

set (Fig. 1.5b) to form (purple) fits with predicted lineaments well near 50°W, but the anti-podal set do not fit as well with predicted lineaments. It is likely that the unmatched pit chains formed at a slightly different time in the sequence as is the case with the subsequent set (red) in Fig. 1.5c. The following sets (Fig. 1.5d) appear to match predicted lineaments east of 0° and likely formed contemporaneously. However the two sets with similar orientations on the other hemisphere, near 150°W may not have formed contemporaneously. The E-W oriented set never quite matches with predicted lineaments however, this set crosscuts the south polar dichotomy, which likely has an inherited crustal fabric that is affecting or driving this set of pit chains to form. The penultimate set (Fig. 1.5e) in the series matches predicted lineaments well south of the equator, but again, their broad spatial extent suggests that some of these pit chains likely formed at a different point in the NSR stress field. The final set (Fig. 1.5f) to form (green) has a similar match to predicted lineaments as in the previous set. The formation of these 7 sets results in a minimum of 135° of ice shell rotation, however an additional 120° is required to emplace the pit chains at their present day longitude. This is not meant to suggest that the formation of pit chains ceased during this 120°. It is possible that the ice shell effectively thickened lowering the magnitudes of the stresses such that the ice shell could not be fractured. A slow-down in the NSR rate also could have occurred causing the built up stresses to relax away. But we must also consider that the NSR stress is also anti-podal capable of producing symmetrical fracture sets. Therefore pit chain sets that were formed near the anti-Saturn side, with and additional 120° of rotation, will likely encounter a familiar stress field. This would act to effectively reactivate pre-existing sets of pit chains which is more efficient than creating new pit chains sets. This interpretation would be consistent with the observation of all stages of pit chain formation within each set.

If NSR is occurring on Enceladus, the most likely mechanism for decoupling the ice shell from its core is the presence of a global liquid ocean. A regional, south polar ocean has been suggested to reconcile the topographic depression and gravity anomaly observed at the south pole [*Collins & Goodman,* 2007; *Iess et al.,* 2014]. However, models of a regional south polar sea are not incompatible with the hypothesis of a global ocean. The ice shell is likely thinner in the SPT as evidenced by a 0.4 km difference between the SPT and the best-fit ellipsoid to Enceladus's shape [*Porco et al.,* 2006; *Collins & Goodman*, 2007]. This

topographically lower region might be indicative of a deeper ocean at the base of the ice shell, which would be consistent with the observed gravity anomaly of *Iess et al.,* [2014]. This observation however would not negate the possibility of a global ocean. If Enceladus has, or recently had, a global liquid ocean, it may become an important target for future astrobiological exploration, particularly considering Enceladus's unique and intense thermal history [*Spencer et al.,* 2006; 2013*; Howett et al*., 2011*; Bland et al.,* 2007; 2012].

Although our observations provide strong evidence for NSR being a valid mechanism for producing the pattern of pit chains across Enceladus's surface, we nonetheless address some possible contradictions that could be interpreted to suggest NSR is unlikely. For example, Enceladus exhibits distinct antipodal geologic terrains, with cratered terrains centered on the Saturn and anti-Saturn points and tectonic terrains centered on the leading and trailing axes. One might suggest that this configuration is more than a coincidence and therefore difficult to reconcile with a model in which NSR has been slowly rotating the ice shell. In actuality, however, cratered terrains are centered near 20°W and 160°E longitude and the bounding extents of the cratered terrains are abrupt and irregular. The sub-Saturn cratered terrains extend as far west as 60°W. Formation of the anti-podal tectonized terrains have been hypothesized to be related to low-order convection and reorientation during differentiation [*Pappalardo & Schubert,* 2013]. However there seems to be basis for preferential reorientation of the tectonized terrains to their current locations on the leading and trailing points. Furthermore, as the dearth of craters within the tectonized terrains suggests, these terrains are relatively young [*Kirchoff & Schenk*, 2009] rather than being associated with differentiation, which likely occurred early on in Enceladus's formation. Additionally, if the alignment of the terrains was indicative of their formation *in situ*, one might predict the most heavily cratered terrain to be on the leading and trailing hemispheres [*e.g. Zahnle et al.,* 2003], yet they are orthogonal to these directions. Although the approximate alignments of the cratered and tectonized terrains with the tidal and orbital axes would thus need to be considered coincidental in the event that NSR is occurring, a minimum amount of rotation of 273° (this study) to 153° [*Patthoff & Kattenhorn*, 2011] would imply that the cratered terrains have passed through their current alignment at least once rendering the coincidence more likely. If NSR has occurred for a large fraction of Enceladus's history, than a

longitudinally homogenous distribution of cratering might be expected which may not be the case if the period of bombardment was relatively short-lived with respect to the NSR rate.

Although pit chains have been observed within the tectonized terrains, especially in the region of Labtayt Sulci, the focus of this work was the cratered terrains where the highest concentrations of pit chains have been observed. The lack of pit chains in the tectonized terrains may be due to recent tectonic resurfacing which may also explain the lack of craters within the tectonized terrains despite NSR. Alternatively, a limited supply of regolith to these regions may cause dilational cracks to take on different morphologies to pit chains. Additionally, the available image resolutions may be insufficient to distinguish pit chains from the myriad other fractures within the tectonized terrains, especially if the regolith is thin and the pit diameters consequently small. The high occurrence of pit chains within the cratered terrains indicates that these terrains are undergoing tectonic dissection, but not by the whole-scale resurfacing processes experienced by the tectonized terrains. Furthermore, experimental work by *Wyrick* [2012] suggests that a cratered surface deformed by dilational cracks cannot completely erase the cratering record as has been done in the tectonized terrains. Therefore craters that likely pre-dated the tectonized terrains could not have been eliminated by the formation of dilational fractures (i. e. pit chains) alone and may have required another mechanism like closely spaced faults at the surface to completely eliminate the surface manifestation of previous cratering.

Conclusions

We report the detection of geologically recent tectonic disruption outside of the SP localized primarily within the cratered terrains by features called pit chains, which has not been previously documented. Pit chains in Enceladus's cratered terrains can be divided into 7 symmetric and anti-podal sets, each with distinct orientations, showing a systematic change in fracture orientation through time. The orientations of the pit chain sets are consistent with nonsynchronous rotation, in which the ice shell is necessarily detached from the core, which allows the shell to move independently likely by a global subsurface ocean. Therefore the fracture history is suggestive of a global subsurface liquid layer, which is critical for understanding the source material for the plume activity and overall history of Enceladus. A localized subsurface ocean beneath the SPT is not sufficient to decouple Enceladus's ice

shell. The patterns of pit chains are consistent with a global stress field that would be produced by nonsynchronous rotation, which requires that the ice shell be decoupled most likely by a global liquid ocean, in agreement with previous work [*Patthoff & Kattenhorn*, 2011]. The existence of a global subsurface ocean on Enceladus, combined with spacecraft measurements that suggest a contemporary high heat flow, makes it one of the few bodies in the outer solar system that may provide a habitable environment with astrobiological potential.

Acknowledgments

References

Bland, M. T., R. A. Beyer, A. P. Showman, (2007), Unstable extension of Enceladus' lithosphere. *Icarus*, 192, p92-105.

Bland, M. T., K. N. Singer, W. B. McKinnon, P. M. Schenk, (2012), Enceladus' extreme heat flux as revealed by its relaxed craters. *Geophys. Res. Lett., 39,* L17204, doi:10.1029/2012GL052736.

Collins, G. C. and J. C. Goodman, (2007), Enceladus' south polar sea. *Icarus*, 189, p. 72-82. doi:10.1016/j.icarus.2007.01.010.

Collins, G., W. McKinnon, J. Moore, F. Nimmo, R. Pappalardo, L. Prockter, P. Schenk, (2010), Tectonics of the outer planet satellites, in *Planetary Tectonics*, 264-350, Cambridge University Press.

Crow-Willard, E. N. and R. T. Pappalardo, (2010), Global Geological Mapping of Enceladus. *41st Lunar and Planetary Science Conference,* Abstracts #2715.

Cruikshank, K. M. and A. Aydin, (1995), Unweaving the joints in Entrada Sandstone, Arches National Park, Utah, U.S.A. *J. Struct. Geol.*, 17, 409-421.

Ferrill, D. A., A. P. Morris, D. Y. Wyrick, D. W. Sims, N. M. Franklin, (2004), Dilational fault slip and pit chain formation on Mars. *GSA Today, 14 (*10), 4-12, doi:10.1130/1052-5173(2004)014<4:DFSAPC>2.0.CO;2.

Figueredo, P. H., and R. Greeley, (2000), Geologic mapping of the nrorthern leading hemisphere of Europa from Galileo sold-state imaging data. *J. Geophys. Res*., 105, 22,629-22,646.

Grant, J. V. and S. A. Kattenhorn, (2004), Evolution of vertical faults at an extensional plate boundary, southwest Iceland. *J. Struct. Geol.*, 26, 537-557. doi:10.1016/j.jsg.2003.07.003.

Greenberg, R. P., and S. J. Weidenschilling, (1984), How fast do Galilean satellites spin? *Icarus* 58, 186-196.

Groenleer, J. M., and S. A. Kattenhorn, (2008), Cycloid crack sequences on Europa: Relationship to stress history and constraints on growth mechanics based on cusp angles. *Icarus,* 193, 158-181. doi:10.1016/j.icarus.2007.08.032.

Hoppa, G., B. R. Tufts, R. Greenberg, P. Geissler, (1999), Strike-slip faults on Europa: Global shear patterns driven by tidal stress. *Icarus*, 141, 287-298. doi:10.1006/icar.1999.6185.

Hoppa, G. B., B. R. Tufts, T. A. Hurford, D. P. O'Brien, P. E. Geissler, (2001), Europa's rate of rotation derived from the tectonic sequence in the Astypalaea region. *Icarus,* 153, 208-213. doi:10.1006/icar.001.6663.

Howett, C. J. A., J. R. Spencer, J. Pearl, M. Segura, (2011), High heat flow from Enceladus' south polar region measured using 10-600 cm^{-1} Cassini/CIRS data. *J. Geophys. Res., 116,* E03003. doi:10.1029/2010JE003718.

Hurford, T. A., P. Helfenstein, G. V. Hoppa, R. Greenberg, B. G. Bills, (2007), Eruptions arising from tidally controlled periodic openings of rifts on Enceladus. *Nature*, 447. 293-294. doi:10.1038/nature05821.

Hurford, T. A., P. Helfenstein, J. N. Spitale, (2012), Tidal control of jet eruptions on Enceladus as observed by Cassini ISS between 2005 and 2007. *Icarus*, 220, 896-903, doi:10.1016/j.icarus2010.06.022.

Iess, L., D. J. Stevenson, M. Parisi, D. Hemingway, R. A. Jacobson, J. I. Lunine, F. Nimmo, J. W. Armstrong, S. W. Asmar, M. Ducci, P. Tortora, (2014), The gravity field and interior structure of Enceladus. *Science,* 344, p. 78-80. doi:10.1126/science.1250551.

Kattenhorn, S. A., (2002), Nonsynchronous rotation evidence and fracture history in the Bright Plains region, Europa. *Icarus*, 157, 490-506. doi:10.1006/icar.2002.6825.

Kattenhorn, S. A. and T. A. Hurford, (2009), Tectonics of Europa. *In*: Europa, Pappalardo, R. T., McKinnon, W. B., and K. Khurana, eds, University of Arizona Press, 199-236.

Kay, J. P., and S. A. Kattenhorn, (2010), An open-source GUI for calculating icy moon tidal stresses using SatStress. *41ˢᵗ Lunar and Planetary Science Conference*, Abstract #2046.

Kirchoff, M. R., and P. Schenk, (2009), Crater modification and geologic activity in Enceladus' heavily cratered plains: Evidence from the impact crater distribution. *Icarus*, *202*, 656-668. doi:10.1016/j.icarus.2009.03.034.

Khurana, K. K., M. G. Kivelson, D. J. Stevenson, G. Schubert, C. T. Russel, R. J. Walker, C. Polanskey, (1998), Induced magnetic fields as evidence for subsurface oceans in Europa and Callisto. *Nature*, 395, 777-780. doi:10.1038/27394

Martin, E. S. and S. A. Kattenhorn, (2013), Estimating regolith thickness on Enceladus using the angle of repose of individual pits within pit chains. *Geological Society of America Abstracts with Programs* Vol. 45, No. 7, p.704, Paper #305-4.

Martin, E. S. and S. A. Kattenhorn, (2014), A history of pit chain formation within Enceladus's cratered terrains suggests a nonsynchronous rotation stress field. *45ᵗʰ Lunar and Planetary Science Conference,* Abstracts #1083.

McEwen, A. S., (1986), Tidal reorientation and the fracturing of Juipter's moon Europa. *Nature,* 321, 49-51. doi:10.1038/321049a0.

Michaud, R. L., R. T. Pappalardo, G. C. Collins, (2008), Pit chains on Enceladus: a discussion of their origin. *39ᵗʰ Lunar and Planetary Science Conference*, Abstract #1678.

Nahm, L. A. and S. A. Kattenhorn, (2014), A Classification and Characterization scheme for tectonic structures on Enceladus. *45ᵗʰ Lunar and Planetary Science Conference,* Abstract #1072.

Nimmo, F., J. R. Spencer, R. T. Pappalardo, M. E. Mullen, (2007), Shear heating as the origin of the plumes and heat flux on Enceladus. Nature, 447, 289-291.

Olgin, J. G., B. R. Smith-Konter, R. T. Pappalardo, (2011), Limits of Enceladus's ice shell thickness from tidally driven tiger stripe shear failure. *Geophy.l Res. Let.*, 38, L02201. doi:10.1029/2010GL044950.

Pappalardo, R. T., and G. Schubert, (2013), Enceladus and Miranda: Similar histories of low-order convection and reorientation during differentiation. *44ᵗʰ Lunar and Planetary Science Conference*, Abstract #2808.

Pappalardo, R. T., M. J. S. Belton, H. H. Breneman, M. H. Carr, C. R. Chapman, G. C. Collins, T. Dent, S. Fagents, P. E. Geissler, B. Giese, R, Greeley, R. Greenberg, J. W. Head, P. Helfenstein, G. Hoppa, S. D. Kadel, K. P. Klaasen, J. E. Klemaszewski, K. Magee, A. S. McEwen, J. M. Moore, W. B. Moore, G. Neukum, C. B. Phillips, L. M. Prockter, G. Schubert, D. A. Senske, R. J. Sullivan, B. R. Tufts, E. P. Turtle, R. Wagoner, K. K. Williams, (1999), Does Europa have a subsurface ocean? Evaluation of the geological evidence. *J. Geophys. Res.* 104 (E10), 24,015-24,055.

Patthoff, D. A., (2013), Tectonic history of the south polar terrain of Saturn's moon Enceladus and evidence for a global ocean. (Unpublished doctoral dissertation). University of Idaho, Moscow, ID.

Patthoff, D. A., Kattenhorn, S. A., (2011), A fracture history on Enceladus provides evidence for a global ocean. *Geophys. Res. Let.*, 38, L18201. doi:10.1029/2011GL048387.

Porco, C. C., P. Helfenstein, P. C. Thomas, A. P. Ingersoll, J. Wisdom, R. West, G. Neukum, T. Denk, R. Wagner, T. Roatsch, S. Kieffer, E. Turtle, A. McEwen, T. V. Johnson, J. Rathbun, J. Veverka, D. Wilson, J. Perry, J. Spitale, A. Brahic, J. A. Burns, A. D. DelGenio, L. Dones, C. D. Murray, S. Squyres, (2006), Cassini observes the active south pole of Enceladus. *Science*, 311, 1393-1401. doi:10.1126/science.1123013.

Roberts, J. H., and F. Nimmo, (2008), Tidal heating and the long-term stability of a subsurface ocean on Enceladus. *Icarus*, 194, p. 675-689. doi:10.1016/j.icarus.2007.11.010.

Roatsch, T. E. Kersten, A. Hoffmeister, M. Wahlisch, K. D. Matz, C. C. Porco, (2013), Recent improvements of the Saturnian satellites atlases: Mimas, Enceladus, and Dione. *Planetary and Space Science*, 77, 118-125. doi:10.1016/j.pss.2012.02.016.

Schulson, E. M., and P. Duvall (2009), Creep and Fracture of Ice, 416 pp., Cambridge Univ. Press, Cambridge, U. K., doi:10.1017/CBO9780511581397.

Smith-Konter, B., and Pappalardo, R. T. (2008), Tidally driven stress accumulation and shear failure of Enceladus's tiger stripes. *Icarus*, 198, 435-451.

Spencer, J. R., J. C. Pearl, M. Segura, F. M. Flasar, A. Mamoutkine, P. Romani, B. J. Buratti, A. R. Hendrix, L. J. Spilker, R. M. C. Lopes. (2006), Cassini encounters Enceladus: Background and the discovery of a south polar hot spot. *Science, 311*, 5766, 1401-1405. doi:10.1126/science.1121661.

Spencer, J. R., C. J. A. Howett, A. Verbiscer, T. A. Hurford, M. Segura, D. C. Spencer, (2013), Enceladus heat flow from high spatial resolution thermal emission observations. *European Planetary Science Congress*, v.8 EPSC2013-840-1.

Spitale, J. N. and C. C. Porco, (2007), Association of the jets of Enceladus with the warmest regions on its south-polar fractures. *Nature*, 449, 695-697. doi:10.1038/nature06217.

Wahr, J., Z. A. Selvens, M. E. Mullen, A. C. Barr, G. C. Collins, M. M. Selvans, R. T. Pappalardo, (2009), Modeling stresses on satellites due to nonsynchronous rotation and orbital eccentricity using gravitational potential theory. *Icarus,* 200 (1), 188-206. doi:10.1016/j.icarus.2008.11.002.

Wyrick, D., D. A. Ferrill, A. P. Morris, S. L. Colton, D. W. Sims, (2004), Distribution, morphology, and origins of Martian pit crater chains. *J. Geophys. Res., 109,* E06005. doi:10.1029/2004JE002240.

Wyrick, D. Y. (2012), Analog models of tectonic resurfacing and impact structures on Ganymede. *Geological Society of America Abstracts with Programs*. Vol. 44, No. 7, p.328.

Zahnle, K., P. Schenk, H. Levison, L. Dones, (2003), Cratering rates in the outer Solar System. *Icarus*, 163, 263-289. doi:10.1016/S0019-1035(03)00048-4.

Chapter 2

Characterization of crater-fracture interactions highlights heterogeneities within Enceladus's global stress field

Abstract

We present a new mechanism for the unique way in which craters and fractures interact on Enceladus where additional heat generated from an impact event in a thermally unstable ice shell creates a localized zone of rising warm ice beneath a crater. This warmer ice exerts a uniform outward pressure on surrounding colder ice concentrating stress beneath and around the crater. We conceptualize the buoyant ice to a first order as a pressurized cylindrical body rising beneath the crater. Simple two-dimensional models of vertical, cylindrical bodies filled with a pressurized fluid, located directly below craters, were developed to explore the crater-fracture interactions at the surface. Modeled stress fields produce fracture patterns similar to those observed, assuming a global stress field generated by nonsynchronous rotation of the ice shell about the moon's interior.

2.1 Introduction

Examples of crater-fracture interactions within the solar system are found on Dione (Fig. 2.1a), Ganymede (Fig. 1b) [*Pappalardo & Collins,* 2005], and Venus (Fig. 2.1c) [*Solomon et al.,* 1992; *Rathbun et al.,* 1999] and are characterized by craters that are disrupted by later crosscutting fractures (Fig. 2.1). These fractures are typically systems of normal faults, the growth of which were unaffected by the craters themselves. In contrast, fractures on Enceladus are commonly reoriented as they approach craters. The mutually parallel trend of fractures within regionally extensive fracture sets locally changes with increasing proximity to a crater, converging toward the crater in a broadly radial pattern (Fig. 2.1d). The fractures visibly cut through each crater and must thus postdate crater formation; however, the craters nonetheless induced local perturbations to the regional stress field at the time of fracture growth. Explicit controls on this phenomenon are unknown, as well as why is it not observed elsewhere in the solar system. In this work, we examine Enceladus's cratered terrains to

determine the driving mechanism for crater-induced fracture reorientation in a locally perturbed stress field.
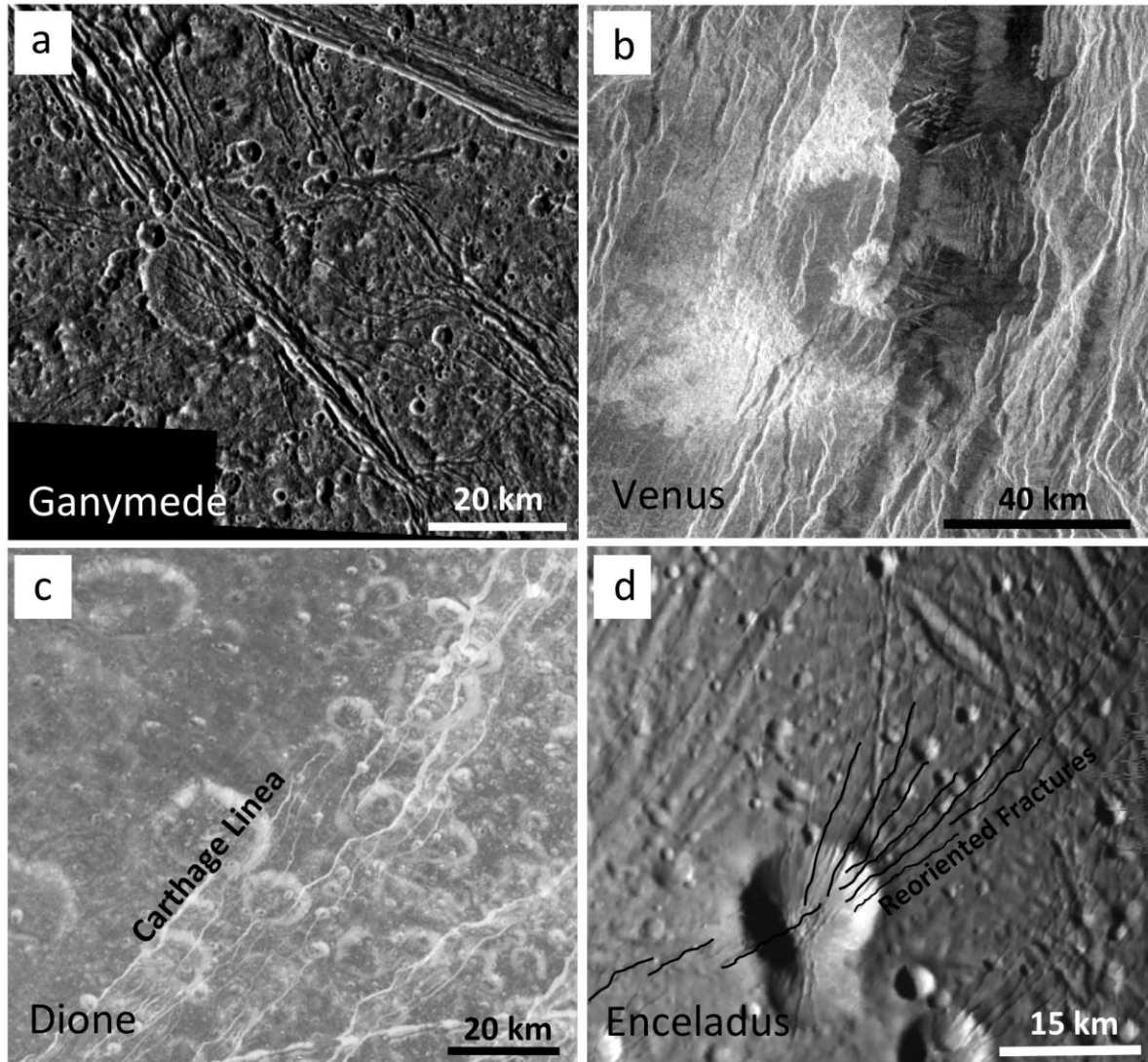
Figure 2.1: Crater-fracture interactions in the solar system. a) Strained crater on Ganymede. Image G8GSANSHAR01. b) Balch crater, a greatly disrupted crater on Venus (40 km; 29.9°N, 282.9°E). c) Craters disrupted by fault scarps on Dione. Image PIA07638. d) Crater-induced fracture reorientation on Enceladus. Image N1500060254.

2.2 Background and Approach

Enceladus's crater-fracture interactions are found predominantly within the cratered terrains on the Saturnian and anti-Saturnian hemispheres, centered at 0° and 180°

respectively. Both simple and complex craters perturb fractures [*Bray et al.,* 2007*; Kirchoff & Schenk,* 2009]. The fractures that experience reorientation by craters are features called pit chains: linear troughs composed of circular or elliptical depressions, and interpreted to represent some of the youngest features on Enceladus's surface [*Michaud et al*., 2008; *Martin & Kattenhorn*, 2013]. Pit chains are found across the inner solar system, including Earth [*Grant & Kattenhorn,* 2004], Mars [*Wyrick et al.,* 2004; *Ferrill et al.,* 2004], and Vesta [*Jaumann et al., 2012*]; however, Enceladus is the only body in the outer solar system where pit chains have been described [*Michaud et al.,* 2008], although pit chains have been suggested to exist on Tethys [*Schenk & Moore,* 2014], Europa, Ganymede, and Dione [*Wyrick et al.,* 2010].

Crater-fracture interactions on Enceladus have been previously examined [*Barnash et al.,* 2006; *Bray et al.,* 2007; *Miller et al.,* 2007] and several mechanisms for crater induced fracture reorientation have been proposed. *Miller et al.* [2007] suggest that topographic loading by the crater rim may perturb fracture growth; however, rim topography (simple lunar craters have rim heights ~4% of their rim-to-rim diameters [*Melosh,* 1989]) is not likely to influence the local stress field at the observed distances of at least two crater diameters, what we here after refer to as the 'radius of influence'. The radius of influence is the maximum distance at which a stress perturbation can extend; on Enceladus, the minimum radius of influence is two crater diameters. Beyond two crater diameters, the influence of additional craters and fractures become possible influences on fracture reorientation, and thus only a minimum may be observed. *Bray et al.* [2007] suggest that the relationship between crater depth and fracture depth may induce fracture reorientation. We propose a new hypothesis in which heat generated by an impact event creates a localized zone of thermally mobilized ice beneath the newly formed crater. The perturbation to the regional stress field as a result of this warmer ice would have the same effect as a pressurized cylindrical hole (for which simple analytical stress solutions exist), which acts to deviate fractures toward the hole, or in this scenario, the crater.

We present detailed fracture maps around select craters to establish the regional tectonic history of the cratered terrains, and use these maps to characterize crater-fracture interactions. These observations were used for comparison against fracture patterns generated with a simple two-dimensional analytical model of a pressurized cylindrical hole. The high heat

fluxes experienced in Enceladus's past, as evidenced by the viscous relaxation of craters [*Bland et al*., 2012; *Kirchoff & Schenk,* 2009], supports the generation and retention of warm ice beneath an impact crater.

2.2.1 Regional Tectonic History

Detailed regional fracture maps were created prior to analysis of crater-fracture interactions. If the tectonic history local to a crater is not well characterized, the influence of craters on proximal fractures may be difficult to isolate from the influence of the regional stress field on fracture development. Detailed fracture maps were created of select regions within the cratered terrains centered at 180° (Fig 2. 2). Mapped fractures were placed into fracture sets based on crosscutting relationships, fracture orientation, and morphology. In the absence of clearly defined crosscutting relationships, fracture orientation and morphology are used to assign a fracture into a particular set. Maps were composed primarily of features
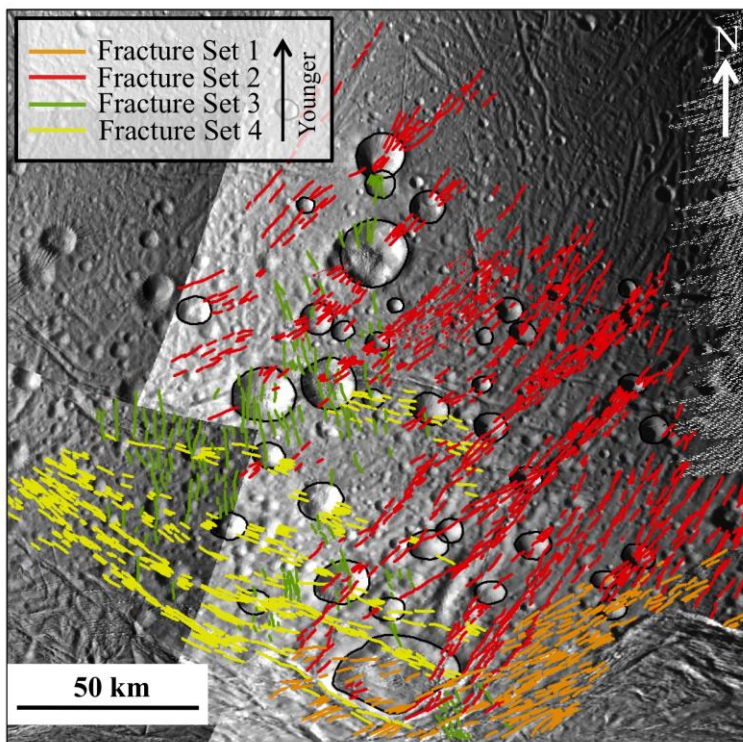
Figure 2.1: Regional fracture map of Enceladus, centered at 30°S, 180°W. Four systematic fracture sets with distinct orientations suggest a relative rotation of the stress field through time. Crosscutting relationships indicate a relative age sequence; from oldest to youngest, yellow formed first, then green, red, and orange. Mosaic created from Cassini image numbers N1500061634, N1500060345, N1500061010, N1500060254, and N1489050409.

called pit chains, which are linear arrangements of circular to elliptical pits, which form from the drainage of loose material overlying a subsurface dilational crack [*Michaud et al.,* 2008; *Ferrill et al.,* 2004; 2004; *Wyrick et al.,* 2004]. Pit chains take on a variety of morphologies, which depend on the amount of dilation along the crack. Chains of isolated pits represent the early stages of dilation and fully merged pit chains characterized by troughs with scalloped

rims, represent a later stage of evolution where more dilation has accumulated along the crack [*Michaud et al.,* 2008; *Ferrill et al.,* 2004; 2004; *Wyrick et al.,* 2004]. Pit chains are isolated primarily within the cratered terrains near the Saturn and anti-Saturn points [*Michaud et al.,* 2008], but have also been observed within the trailing hemisphere tectonized terrains [*Martin & Kattenhorn,* 2013]. Pit chains are some of the youngest features on Enceladus's surface [*Michaud et al.,* 2008; *Martin & Kattenhorn,* 2013] and are the types of fractures that interact with craters within the cratered terrains and were therefore the focus of the detailed fracture maps. As pit chains were being mapped, they were divided into sets based primarily on their orientation.
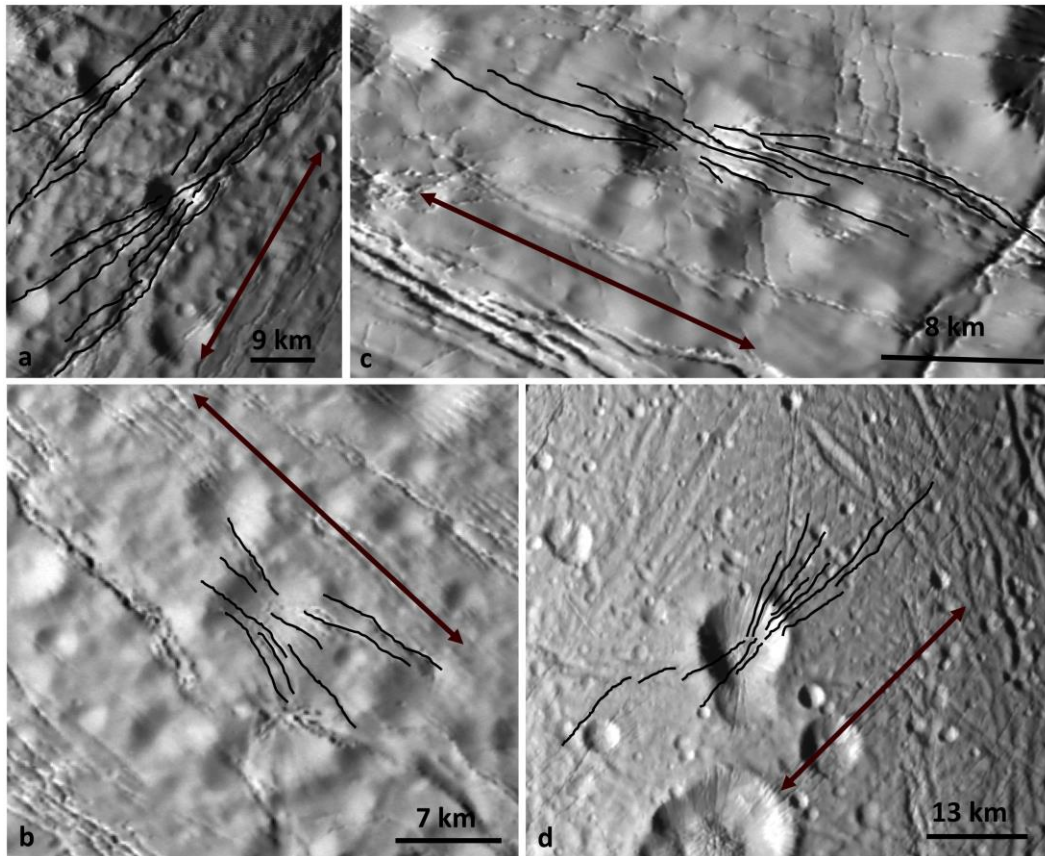
Figure 2.2: Examples of crater-fracture interactions across Enceladus. Black lines highlight fractures within one fracture set experiencing some amount of reorientation. Red arrows indicate the average set orientation. a. In some cases fractures cluster near craters. Image No. N1500060254 at 37°S and 172°W. b. Some craters affect fractures only within one crater diameter called the radius of influence in part due to near-by craters or tectonic structures. Image No. N150061634 at 38°S and 152°E. c. Some craters have a more subtle effect on fracture reorientation. Image No. N1500062382 at 45°S and 170°E. d. Image. No. N1500060254 at 15°S and 179°E.

2.2.2 Characterizing crater-fracture interactions

Crater fracture interactions are characterized by at least one set of fractures that are reoriented away from the average orientation of the fracture set at or near a crater (Fig. 2.3). The amount of reorientation varies; Fig. 2.3a, b, & d demonstrate a greater angular deviation from the average orientation of the fracture set than is observed in Fig. 2.3c. But in all cases, fractures within one set as they approach the crater, no longer represent the average orientation of the set. Two craters in Fig. 2.3a demonstrate a unique characteristic of some interactions between craters and fractures where fractures break into closely spaced clusters of fractures focused and reoriented towards individual craters.

The maximum distance at which a crater can perturb a fracture is called the *radius of influence.* We observe a radius of influence for most craters of up to two crater diameters in all directions away from the crater rim. Beyond two crater diameters it is not possible to isolate the influence of crater-induced fracture reorientation to the crater: frequently the presence of another crater(s) or tectonic structures occur.

Some fractures are affected by the presence of the crater; however, mapping indicates that in some instances interacting fracture sets can give the appearance of reorientation (Fig. 2.4). A crater that gives the outward appearance of influencing fracture orientations proximal to the crater (Fig. 2.4a) is instead interacting

Figure 2.3: a) An example of apparent crater-induced fracture reorientation revealed to be two interacting, systematic fracture sets within the cratered terrains mapped based on crosscutting relationships, fracture orientation, and morphologies. However, the arrow indicates one arcuate fracture that is likely being reoriented. Image centered at 2°N, 162°W. Image No. N1489050254. b) A fracture (indicated by black arrow), mapped based on orientation and morphology (in the absence of crosscutting relationships), and may not have undergone reorientation. Centered at -4.7°S, 161.9°E. Image No. N1489050442.

fracture sets in the vicinity of the crater. However, crater induced fracture reorientation is the likely driving mechanism for the large actuate fracture indicated in Fig. 2.4a. Similarly, a fracture indicated by the arrow in Fig. 2.4b was placed into a fracture set based on orientation and morphology, as crosscutting relationships were non-existent. What appears to be a reoriented fracture may in fact belong to a fracture set with a different orientation. These examples (Fig. 2.4) illustrate the importance of considering the regional geologic history local to each crater.

2.2.3 Controls on Crater-Fracture Interactions

Explicit controls on crater-fracture interactions can be determined by considering crater size, fracture spacing, and amount of fracture reorientation. We selected a population of craters for this analysis based on their state of degradation, image resolution, and relative age relationship between the crater and crosscutting fractures. A crater was selected if a younger fracture was observed crosscutting the crater rim in two places and if the image resolution was sufficient to resolve the fracture passing through the interior of the crater. Without these qualifications, it was not possible to verify the relative
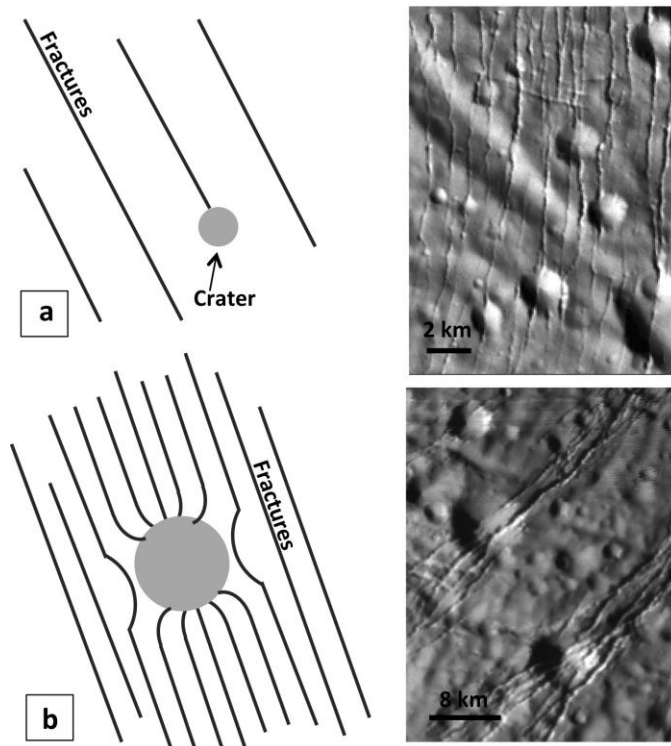
Figure 2.4: Conceptualized crater-fracture interactions. (a) Craters with small diameters relative to fracture spacing have a minimal effect on fracture reorientation. (b) Craters with diameters much larger than fracture spacing noticeably perturb fractures.

age of the crater with respect to the fracture to ensure that the crater pre-dated the fracture. Craters that appeared heavily degraded were also excluded as these craters preserve a complex history of modification by viscous relaxation, mantling by plume material [*Kirchoff & Schenk*, 2009; *Bray et al.,* 2007; *Bland et al.,* 2012], or interruption by older fractures and impacts. A population of 83 craters met these criteria.

Of the sample population identified, craters were divided into two sub-populations: those with reoriented fractures (69 craters) and those without reoriented fractures (14 craters). The mean diameter of craters that reorient fractures is 6.8 km (with crater diameters ranging from 1.8–18.4 km) and the mean diameter for craters that do not reorient fractures is 4 km (with crater diameters ranging from 1.9–6.3 km). Therefore, we find craters of all sizes can influence fracture growth but there is a diameter threshold of ~7 km above which craters are likely to reorient fractures.

This crater-size threshold may be a result of the relationship between the crater size and fracture spacing (Fig. 2.5). A crater that is small with respect to the fracture spacing may not have a large enough radius of influence to perturb the regional stress field to a great enough extent to reorient fractures, whereas a crater that is large with respect to fracture spacing will be more likely to intersect a fracture and influence its orientation. Fracture spacings were measured perpendicular to strike, and averaged resulting in ranges from 0.5-1.25 km for fracture sets around a small subset of craters. This range is very near the threshold of the diameter of the smallest craters in the population in this study and means that smaller craters may not intersect more than one or two fractures.

2.2.4 Formation of pit chains in the cratered terrains

Enceladus's cratered terrains are some of the oldest and most heavily cratered regions on the surface are estimated to be between 4.2-1.7 Ga [*Porco et al.,* 2006] and 4.6-0.6 Ga [*Kirchoff & Schenk,* 2009], and are overlooked as being tectonized [*Martin & Kattenhorn,* 2014]. While there are tectonic structures that appear to have formed prior to the cratered terrains, the most prominent tectonic features in these regions are called pit chains. First reported to exist on Enceladus by *Michaud et al.,* [2008], pit chains are some of the youngest features on the surface and are closely associated with the cratered terrains on both the Saturn and anti-Saturn sides [*Martin & Kattenhorn,* 2013; 2014]. Pit chains fall into 6 individual sets, each with distinct orientations and cross cutting relationships which suggest sequential formation in a temporally changing stress field likely due to nonsynchronous rotation [*Martin & Kattenhorn*, 2014], consistent with previous investigations of *Patthoff & Kattenhorn,* [2011]. The question remains, how do craters influence the orientation of geologically young pit chains, which are forming in response to a global stress field? Heat is produced during an

impact event, which could preferentially produce a region of localized upwelling, or diapirism, beneath a crater. This thermally mobilized ice would act to concentrate the stresses from the remote stress field, generated by nonsynchronous rotation, which might be sufficient to locally reorient the fractures away from their propagation direction. We test the likelihood that stress being produced by a nonsynchronous rotation stress (NSR) field can be perturbed sufficiently to locally affect fracture growth by conceptualizing the system as a pressurized cylindrical body.

2.3 Modeling the regional stress field around a crater

We propose that heat introduced by an impacting event will significantly change the local thermal structure, creating a zone of thermally mobilized ice (a diapir) that locally perturbs the stresses below and around the crater. This perturbation may then reorient fractures away from an orientation that would otherwise be produced by the regional stress field, into a more radial pattern about the region of warmer ice. Furthermore, the formation of an impact may concentrate heat flux within the ice shell by effectively thinning the ice shell at the impact site. This effect may contribute or possibly control the local thermal structure at the crater, however testing a thermal model is beyond the scope of this work. We test an elastic model of the stress field for a cylindrical body which is described by simple analytical solutions from *Jaeger et al.,* [2007]. Pressurized cylindrical bodies are a first order approximation of thermally mobilized ice: there is no available data to suggest the structure of the underlying bodies. Similar fracture patterns have been observed around prehistoric volcanic pipes (e.g., Shiprock, New Mexico, [*Delaney & Pollard,* 1981] and Spanish Peaks, Colorado [*Muller & Pollard,* 1977]) and are common in hydrofractures around pressurized cylindrical body [*Haimson & Fairhurst*, 1967]. Terrestrial analogs for impact-induced diapirism include Upheaval Dome in Canyonlands National Park, Utah [*Daly,* 2010]. *Daly,* [2010] found that an impact event at Upheaval Dome induced circular salt diapirism producing radial and concentric stress fields. We the geometry of a pressurized cylindrical body as a first-order approximation of a pressurized body in the thermally perturbed ice shell beneath an impact site.

The 2D state of stress around pressurized cylindrical body is well characterized by a series of equations for each of the three stress components in a polar coordinate system [*Jaeger et al.*, 2007]:

$$\sigma_{rr} = -\frac{1}{2}(S_H + S_h)\left[1 - \left(\frac{a}{r}\right)^2\right] - P_f\left(\frac{a}{r}\right)^2 - \frac{1}{2}(S_H - S_h)\left[1 + 3\left(\frac{a}{r}\right)^4 - 4\left(\frac{a}{r}\right)^2\right]cos2\theta \qquad (1)$$

$$\sigma_{\theta\theta} = -\frac{1}{2}(S_H + S_h)\left[1 + \left(\frac{a}{r}\right)^2\right] + P_f\left(\frac{a}{r}\right)^2 + \frac{1}{2}(S_H + S_h)\left[1 + 3\left(\frac{a}{r}\right)^4\right]cos2\theta \qquad (2)$$

$$\sigma_{r\theta} = \frac{1}{2}(S_H - S_h)\left[1 + 2\left(\frac{a}{r}\right)^2 - 3\left(\frac{a}{r}\right)^4\right]cos2\theta \qquad (3)$$

where σ_{rr} is the radial stress, $\sigma_{\theta\theta}$ is the circumferential stress, $\sigma_{r\theta}$ is the shear stress, S_H and S_h are the regional maximum and minimum horizontal stresses respectively, a is the radius of the cylindrical body, and r is the radial distance from the hole. From these equations, the magnitude of the radial and circumferential stresses may be calculated with respect to distance from the hole due to a regional stress field like NSR.

Table 2.1: Parameters used to calculate point stresses at Enceladus's surface using SatStressGUI [*Wahr et al.*, 2009; *Kay & Kattenhorn*, 2010]. ρ is density, G is the shear modulus, λ is the Lamé Parameter, η is the viscosity, E is Young's Modulus, and ν is Poisson's Ratio. Rheological properties consistent with previous work [*Olgin et al.*, 2011; *Smith-Konter & Pappalardo* 2008; *Nimmo et al.*, 2007]

	ρ(kg/m^3)	G (Pa)	λ (Pa)	Thickness	η (Pa·s)	E	ν (Pa)
Upper Ice Shell	917	3.5×10^9	6.8×10^9	2×10^3-8×10^3	1×10^{23}	9.3107×10^9	3.301×10^{-1}
Lower Ice Shell	917	3.5×10^9	6.8×10^9	2.2×10^4-7.8×10^4	1×10^{17}	9.3107×10^9	3.301×10^{-1}
Ocean	1000	-	2×10^9	1×10^4- 7.2×10^4	-	-	-
Core	3500	1×10^{12}	4×10^{10}	1.56×10^5	-	-	-

We use a simple, two-dimensional model formulated for use in Matlab$^\circledR$ [modified from *Pollard & Fletcher,* 2005], and based on equations (1) to (3), to calculate the orientations of fractures around a pressurized hole in a biaxial stress field (S_H and S_h; representing the horizontal stresses in the ice shell of Enceladus) and compare them with observed fracture patterns around craters. The pressurized hole is used as a first-order approximation of a rising diapir of warm ice located directly beneath a crater. The fluid pressure within the body exerts an outward force evenly against the walls of the cylindrical body in the same way a localized

region of warm buoyant ice would exert a force on the surrounding colder ice. Hereafter, we refer to the warm buoyant ice as a fluid for the purposes of discussion of the model results.

S_H and S_h were obtained using SatStressGUI, a graphics user interface developed by *Kay & Kattenhorn* [2010] based on SatStress [*Wahr et al.*, 2009], an analytical model for calculating tidally-induced stresses at the surface of a planetary body at prescribed locations. SatStress assumes a 4-layer differentiated body and allows the user to define the satellite's interior structure, the rheological properties of each layer, and the source of stress (diurnal or NSR) (Table 2.1). Diurnal stresses are not included in our reported results because the derived magnitudes are insufficient to overcome the tensile strength of ice (1-3 MPa [*Schulson & Duvall,* 2009]). We do not suggest that diurnal stresses are not contributing to Enceladus's global stress field, rather NSR stresses are the primary control on the fracture patterns manifested on Enceladus's surface [*Patthoff & Kattenhorn,* 2011; *Martin & Kattenhorn,* 2014], which has also been suggested for Europa [e.g., *Kattenhorn,* 2002; *Pappalardo et al.,* 1999]. We therefore include a global ocean because the existence of a global liquid layer is the most likely way of decoupling the ice shell from the interior allowing the ice shell to rotate nonsynchronously [e.g. *Patthoff & Kattenhorn,* 2011; *Greenberg & Weidenschilling,* 1984].

We evaluated 11 craters in SatStressGUI to observe the difference in stress magnitudes due to NSR stresses in a variety of locations. Using the latitude and longitude of the crater center, the SatStressGUI point calculator allows the user to calculate the principal stresses at specific locations. Stresses at each crater were calculated for two different NSR periods (1×10^6 and 1×10^7 years), three different ice shell thicknesses (24 km, 46 km, and 86 km), and varying amounts of NSR (30°, 60°, 90°, and 120°) to determine how the magnitudes of the principal stresses were affected. The stress magnitudes were consistently high enough to fracture the ice shell, and covered a range of differential stresses (the difference between S_H and S_h), and created both tensile and compressional stress regimes. However, with the myriad free parameters, one crater was selected as a representation of the crater population as a whole to be modeled as a pressurized cylindrical body. For this crater we used an NSR period of 1×10^6: a period of 1×10^7 is long enough that stresses will begin to relax away. We used ice shell thickness of 86 km, which is a conservative estimate, as a thicker ice shell is more difficult to fracture. The pore fluid pressures ranged from 1 to 15 MPa.
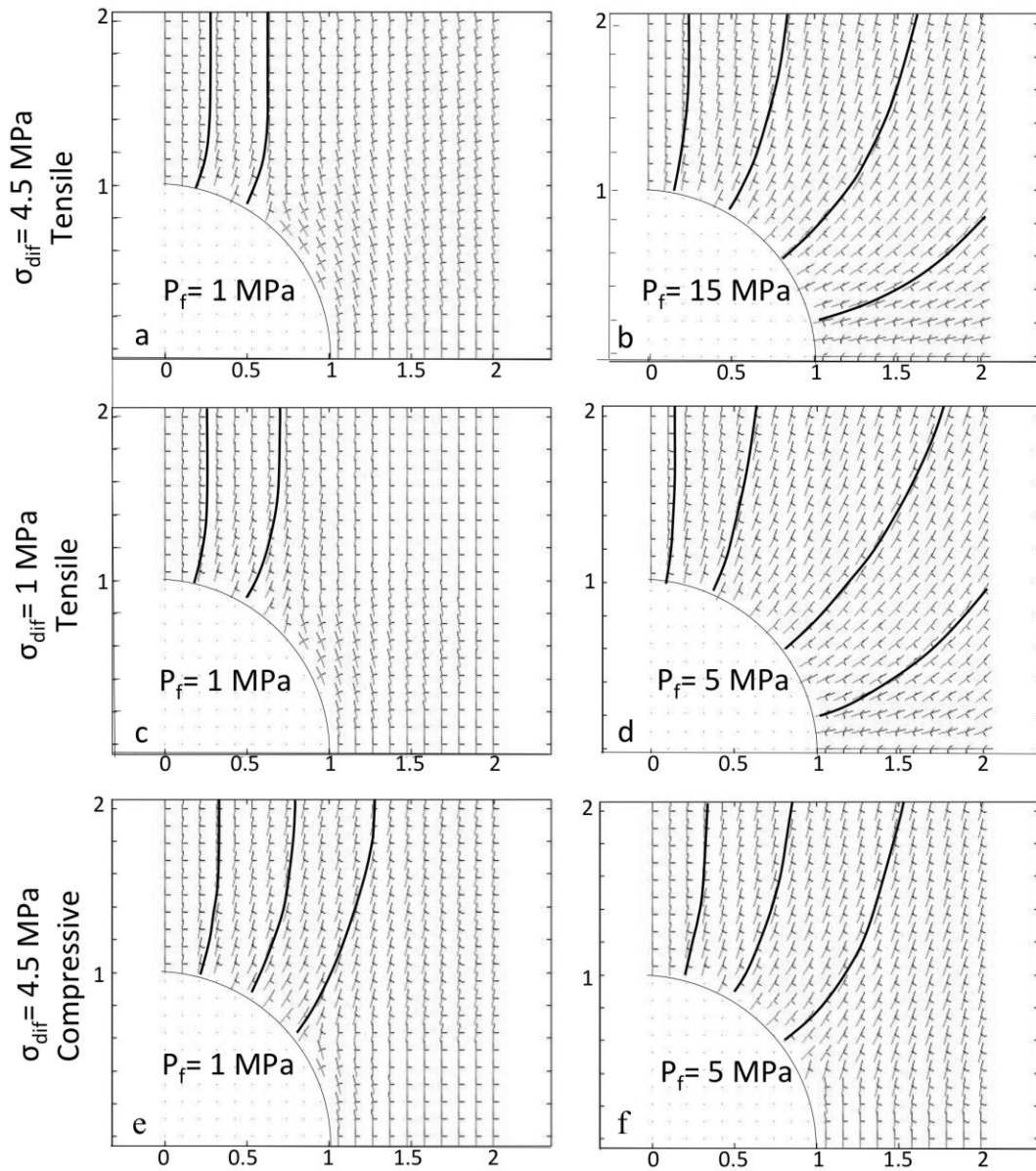
Figure 2.5: A summary of results demonstrating modeled fracture patterns around one crater modeled within a nonsynchronous rotation stress field (see main text for details). From the magnitudes of principal stresses measured at a crater center in SatStressGUI, the orientation of the principle stresses around the crater were calculated and plotted. Long ticks are the direction of the minimum tension and short ticks are the maximum tension. (a) tensile regimes with large differential stresses (b) require unrealistic pore fluid pressures to produce radial fracture patterns; (c) tensile regimes with smaller differential stresses (c) requiring smaller pore fluid pressures (d) to produce similar fracture patterns. (e) a compressive stress field which produces radial fracture patterns with higher differential stresses which (f) require pore fluid pressures lower than in b.

For each stage of NSR, the S_H and S_h were calculated with SatStressGUI, and were input into our 2D model of a pressurized cylindrical body. Our 2D approach invokes a symmetry boundary assumption which means that results are reflected across the x and y axes, so it is only necessary to calculate stresses for one quarter of the hole. Each model output plots the trajectories of the stresses around the cylindrical body rather than the magnitudes. Fracture patterns are inferred from the output by tracing a path dictated by the maximum compressive stress: in a tension positive sign convention, maximum compression (σ_3), indicated by the long tick (Fig 2.5 & 2.6). Pit chains are likely the result of subsurface dilational cracks [*Michaud et al.,* 2008; *Wyrick et al.,* 2004] and will form parallel to the direction of σ_3.

2.4 Model Results

Stress trajectories around a 2 km crater, located at 159.19°E and 0.17°S were modeled with varying amounts of NSR: 30°, 60°, 90°, and 120° degrees of ice shell rotation. Changes in amounts of NSR (varies with the longitude of the crater) changes the orientations and magnitudes of the principal stresses of the remote stress field around the cylindrical body resulting in changes in the differential stress (the difference between the maximum and minimum horizontal stress). The change in the amount of ice shell rotation also can affect whether the stress regime is tensile (S_H is positive) or compressive (S_H is negative). A sample of results for this crater is shown in Fig. 2.6. At the current location of the crater, Fig. 2.6 a & b, the crater resides in a tensile stress regime, which we modeled with various fluid pressures to achieve different fracture patterns. We illustrate two examples of different fluid pressures, 1 MPa (Fig. 2.6a) and 15 MPa (Fig. 2.6b). We observe that in a tensile remote stress field with differential stresses ~4-9 MPa, pore fluid pressures of 15-20 MPa are required to produce fracture patterns similar to those observed. However, fluid pressures of 15-20 MPa are unrealistic: magma chambers from Icelandic volcanoes infer magmatic pressures of 5 MPa prior to rupture [*Gudmundsson*, 1998]. This suggests that fracture formation around this crater (Fig. 2.6) did not initiate while the crater was in its present location (Fig. 2.6 a &b), but likely earlier. By back-rotating the ice shell, at the same crater, the magnitudes (and orientations) of the principal stresses change which change the differential stress while still in a tensile stress regime (Fig. 2.6 c & d). With a differential stress of 1 MPa, more realistic fluid pressures of 5 MPa (Fig. 2.6d) [*e.g., Gudmundsson*, 1998] produce realistic fracture

patterns. This is reasonable because the pore fluid pressure must first overcome the least tensile stress before it can perturb the orientation of fracture growth. Therefore it is possible for fracture patterns to form in a tensile stress regime if the differential stresses are near 1 MPa. Further back-rotation of Enceladus's ice shell achieves a compressional stress regime (Fig. 2.6 e & f) where a pore fluid pressure of 5 MPa (Fig. 2.6f) produces fracture patterns similar to those observed. While the differential stresses are greater than those in Fig. 2.6 c & d, it takes a similar 5 MPa to overcome the compressive remote stresses. We therefore find that there multiple stress regimes that are capable of producing realistic fracture patterns, but not at the present longitude. Inducing ice shell rotation caused by NSR, we are able to reconcile the fracture patterns within multiple stress regimes.
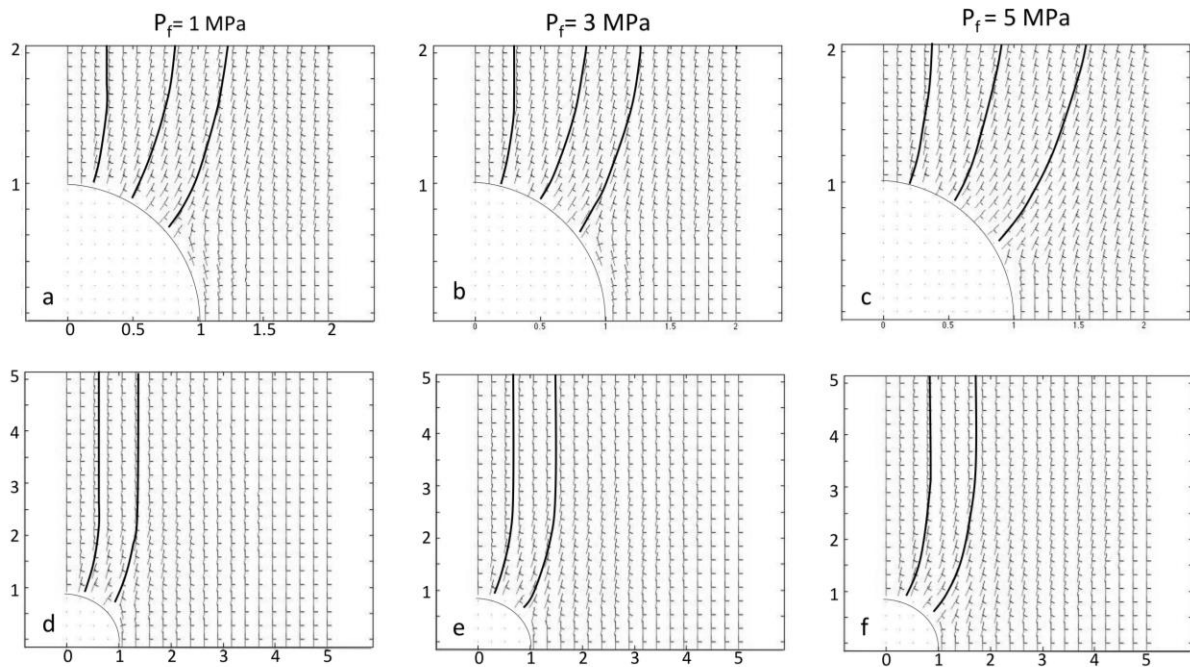
Figure 2.6: A radius of influence of up to two crater diameters is observed on Enceladus, and matches models of crater-fracture interactions driven by thermally mobilized ice beneath a crater. Tick marks indicate the orientation of the principal stresses; long ticks indicate the orientation of minimum tension and short ticks indicate the orientation of maximum tension. We show the effect of fluid pressure on the radius of influence, and for each pressure and find that the radius of influence increases with increasing fluid pressure. The same model output is shown at two different scales to illustrate how fracture patterns change with proximity to the crater.

In addition to producing the observed fracture patterns, the hypothesis of thermally mobilized ice is must explain the radius of influence. We model a rising diapir beneath a crater as a pressurized cylindrical body, to determine if it is capable of producing the

observed minimum radius of influence of two crater diameters. Additionally, it was necessary to understand how the pore fluid pressure would affect the radius of influence. We modeled the same 2 km diameter crater varying pore fluid pressures ranging from 1-5 MPa (Fig. 2.7), and extending the field of view to encompass fractures at one crater diameter (Fig. 2.7 a, b, & c) to four crater diameters (Fig. 2.7 d, e, & f) to observe how far from the crater fracture orientations could be perturbed. We also note that increasing pore fluid pressure increases the radius of influence, but that a fluid pressure of 1 MPa (Fig. 2.7d) may not be sufficient to perturb fracture orientations as far as two crater diameters. A fluid pressure of 3 MPa is able to perturb fracture orientations up to two crater diameters (Fig. 2.7e) and a fluid pressure of 5 MPa can affect fracture orientations up to 3 crater diameters, which exceeds what is observable on Enceladus.

Model results demonstrate that thermally mobilized ice will sufficiently perturb fracture orientations under certain conditions, which can be achieved if Enceladus's ice shell has undergone NSR. Furthermore, a rising diapir of warm ice is able to produce a radius of influence of at least two crater diameters.

2.5 Discussion

For an impact event on Enceladus to trigger a zone of localized upwelling with sufficient buoyancy-driven, outward pressure to regionally perturb the regional stress field, Enceladus's ice shell was likely already in a convective state or on the threshold of convection.

Thermally-driven ice diapirism has been suggested to produce Europa's pits, spots, and domes (PSD) [*Pappalardo et al.,* 1998; *Rathbun et al.,* 1998; *Sotin et al.,* 2002; *Schenk & Pappalardo,* 2004]. *Rathbun et al*. [1998] concluded that to produce a PSD, the diapir must form on short timescales (10^3 – 10^4 years), and initiate at depths of 10s of kilometers. Thermo-compositional diapirism and brine mobilization are also possible mechanisms for producing pits and domes on Europa [*Han & Showman,* 2005; *Showman & Han,* 2004; *Pappalardo & Barr,* 2004; *Head & Pappalardo,* 1999]. Diapirism driven by compositional layering on Triton has been suggested as a mechanism driving the formation of the cantaloupe terrain (Schenk & Jackson, 1993). Europa's pits, spots, and domes, and Triton's cantaloupe terrain likely represent diapirs that reached the satellite's surface; however, this may not be required to produce the observed crater-fracture interactions on Enceladus.

Rather, a diapir that ascends into Enceladus's ice shell may only be required to reach a depth shallow enough to locally perturb the stress field driving fracture reorientation.

The conditions for initiating convective processes have previously been considered for Enceladus [*Barr & McKinnon,* 2007; *Roberts & Nimmo*, 2008 b; *Mitri & Showman,* 2008 a, b; *Grott*, 2007], including mobile lid convection in Enceladus's south polar terrain [*Barr,* 2008] and episodic overturn of sections of a rigid lid [*O'Neill & Nimmo*, 2010]. Previous work has shown that the conditions for convection rely on ice shell thickness, viscosity, and heat flux [*Barr & McKinnon,* 2007]. Regardless of the style of convection, these previous studies suggest that it is possible to induce convection within the ice shell of Enceladus, but how these process are manifested on Enceladus's surface has not been documented.

Enceladus's anomalously high heat flows have been inferred from observational data, both within and outside of the SPT. The Cassini Composite Infrared Spectrometer (CIRS) observed the SPT, and inferred associated heat flows range from ~4.7 GW [*Spencer et al.,* 2013] to 5.8 ± 1.9 GW [*Spencer et al.,* 2006] to as high as 15.8 ± 3.1 GW [*Howett et al.,* 2011] (which may need to be revised downward [*Spencer et al.,* 2013]). Averaged over the area of the SPT, these results correspond to heat flows as high as 400 mWm^{-2} [*Bland et al.,* 2012]. Observations of relaxed craters within Enceladus's cratered terrains suggest heat fluxes on the order of 150 mWm^{-2} [*Bland et al.,* 2012], consistent with heat fluxes inferred from select tectonized regions ranging from 110–220 mWm^{-2} [*Bland et al.,* 2007] and 200–270 mWm^{-2} [*Giese et al.,* 2008]. The source of these heat fluxes and heat flows from CIRS and observational studies have yet to be accounted for, but it is clear that Enceladus has sustained a varied and intense thermal history.

Our conceptual model for crater-fracture interactions on Enceladus is predicated on the assumption that the ice is sufficiently thick and thermally unstable to allow triggering of diapirism beneath impact sites. This process is assumed to occur outside of the SPT only, reflecting disparate ice shell conditions. In the case of the SPT, the eruptive tiger stripe fractures must extend deep enough to access the reservoir of water exuded from the plumes. The depth of the cracks depends on the thickness of the brittle layer in which they reside, and how much stress is available to fracture the brittle layer. *Patthoff* [2013] suggests that the outer brittle layer of the ice shell in the SPT is 3-4 km thick, whereas in regions outside of the SPT, Enceladus's outer ice shell is 6-8 km thick. The difference between the two regions is

attributed to the differences in the heat flux between the SPT and the region to the north. A heat flow of 15.8 ± 1.3 GW (~400 mWm^{-2} [*Bland et al.,* 2012]) has been inferred within the SPT [*Howett et al.,* 2011] whereas heat fluxes beyond the SPT, specifically within Sarandib and Diyar Planitia regions, range from 110-270 mWm^{-2} [*Bland et al.,* 2007; *Giese et al.,* 2008]. *Bland et al.,* [2012] demonstrates that if the upper, brittle portion of the ice shell within the cratered terrains is thick enough to support craters with lunar-like depth to diameter ratios of 0.2, then for craters up to 34 km in diameter, the brittle ice layer must be ~6-8 km thick. This is consistent with the independent conclusions of *Patthoff* [2013]. If the heat generated by an impact can penetrate the ~6-8 km thick brittle ice layer, it may access the underlying, less viscous ice which will be less resistant to upwelling, promote convection, and possibly affect the orientation of nearby fractures. Additionally, the thickness of the brittle ice shell above a less viscous ice layer are perhaps conditions unique to Enceladus reconciling the lack of this unique style of crater-fracture interactions elsewhere in the solar system.

Enceladus's cratered plains may be as young as 1 Gya or as old as 4 Gya, demonstrating an extensive and complex cratering history [*Kirchoff & Schenk,* 2009]. If these regions indeed have 6-8 km upper brittle layer, we would expect them to be pervasively fractured due to sustained cratering events. If the ice shell had been previously weakened by a period of intense cratering, the more viscous, possibly convecting lower ice shell, can make use of these weak spots for more efficient heat loss and induced upwellings. Furthermore, if Enceladus's ice shell was undergoing mobile lid convection at the time of the formation of the cratered terrains, the surface would have generated higher heat flows than if the ice shell were in a state of stagnant lid convection [*Barr,* 2008]. If Enceladus's ice shell is prone to episodic convection [*O'Neill & Nimmo,* 2010], the high heat fluxes recorded by relaxed craters in Enceladus's cratered terrains imply that these terrains have experienced episodes of higher heat fluxes [*Bland et al.,* 2012].

The heat flow around Enceladus's craters differs from other regions, as evidenced by viscously relaxed craters, and we can infer that periods of high heat flow beneath Enceladus's craters have occurred [*Bland et al.,* 2012]. If these periods of high heat flux coincide with the timing of the formation of the cratered terrains, the thermal conditions of Enceladus's ice shell are likely sufficient to maintain warmer ice beneath a crater.

Conclusions

In our sample of 83 craters, we find that crater-induced fracture reorientation produces near-radial- fracture patterns within increasing proximity to craters. Craters of all sizes are found to perturb fracture orientations, however craters above 7 km in diameter will always perturb fractures. This size threshold may be a factor of the relationship between crater size and fracture spacing: fracture spacings are typically on the order of 0.5-1.25 km which is less than the smallest crater in our sample. However, it does suggest that smaller craters are likely to interact fewer fractures due to their small size. We find thermally mobilized ice beneath a crater, modeled as a pressurized cylindrical body, with a remote stress field produced by nonsynchronous rotation, produces fracture patterns similar to observed crater-induced fracture perturbations within Enceladus's cratered terrains under certain conditions. Radial fracture patterns were produced with a radius of influence of two crater diameters in tensile regimes with low differential stresses (~1 MPa) and compressional regimes, with fluid pressures of 1-5 MPa. It is possible that the source of the remote stress field is something other than nonsynchronous rotation. Our results suggest that it is the relative amounts of differential stress and fluid pressure that dictates crater-fracture interactions.

Acknowledgments

References

Barnash, A. N., J. A. Rathbun, E. P. Turtle, and S. W. Squyres, (2006), Interactions between impact craters and tectonic fractures on Enceladus, paper presented at 38th *Annual Division of Planetary Sciences Meeting,* in Pasadena, California, *Bulletin of the American Astronomical Society* 38(3), 522.

Barr, A. C., (2008), Mobile lid convection beneath Enceladus' south polar terrain, *J. Geophys. Res. 113,* E07009. doi:10.1029/2008JE003114.

Barr, A. C., and W. B. McKinnon, (2007a), Convection in ice I shells and mantles with self-consistent grain size, *J. Geophys. Res., 112,* E02012. doi:10.1029/2006JE002781.

Barr, A. C., and W. B. McKinnon, (2007b), Convection in Enceladus' ice shell: Conditions for initiation, *Geophys. Res. Let., 34,* L09202. doi: 10.1029/2006GL028799.

Bland, M. T., K. N. Singer, W. B. McKinnon, P. M. Schenk, (2012), Enceladus' extreme heat flux as revealed by its relaxed craters. *Geophys. Res. Let., 39,* L17204. doi:10.1029/2012GL052736.

Bray, V. J., D. E. Smith, E. P. Turtle, J. E. Perry, J. A. Rathbun, A. N. Barnash, P. Helfenstein, C. C. Porco, (2007), Impact crater morphology variations on Enceladus, paper presented at *38th Lunar and Planetary Science Conference*, in Houston, Texas, Abstract #1873.

Carr, M. H., Belton, M. J. S., Chapman, C. R., Davies, M. E., Geissler, P., Greenberg, R., McEwen, A. S., Tufts, B. R., Greeley, R., Sullivan, R., Head, J. W., Pappalardo, R. T., Klaasen, K. P., Johnson, T. V., Kaufman, J., Senske, D., Moore, J., Neukum, G., Schubert, G., Burns, J. A., Thomas, P., and Veverka, J. (1998), Evidence for a subsurface ocean on Europa, *Nature,* 391, 363-365. doi:10.1038/34857.

Cassen, P., Reynolds, R. T., Peale, S. J. (1979), Is there liquid water on Europa?, *Geophys. Res. Let.*, 6, 731-734. doi:10.1029/GL006i009p00731.

Daly, R. G., (2010), Fracture styles at Upheaval Dome, Canyonlands National Park, Utah, imply both meteorite impact and salt diapirism. (Unpublished Master's Thesis). University of Idaho, Moscow, ID.

Delaney, P. T., and D. D. Pollard, (1981), Deformation of host rocks and flow of magma during growth of minette dikes and breccia-bearing intrusions near Ship Rock, New Mexico. *U. S. Geological Survey Professional Paper,* 1202.

Ferrill, D. A., A. P. Morris, D. Y. Wyrick, D. W. Sims, N. M. Franklin, (2004), Dilational fault slip and pit chain formation on Mars. *GSA Today, 14 (*10), 4-12. doi:10.1130/1052-5173(2004)014<4:DFSAPC>2.0.CO;2.

Grant, J. V., and S. A. Kattenhorn, (2004), Evolution of vertical faults at an extensional plate boundary, southwest Iceland. *J. Struct. Geol., 26*(3), 537-557. doi:10.1016/j.jsg.2003.07.003.

Greenberg, R., and S. J. Weidenschilling, (1984), How fast do Galilean satellites spin? *Icarus*, 58, 186-196. doi:10.1016/0019-1035(84)90038-1.

Grott, M., F. Sohl, H. Hussmann, (2007), Degree-one convection and the origin of Enceladus' dichotomy, *Icarus, 191,* 203–210. doi:10.1016/j.icarus.2007.05.001.

Gudmundsson, Agust, (1998), Magma chambers modeled as cavities explain the formation of rift zone central volcanoes and their eruption and intrusion statistics. *J. Geophys. Res.,* 104, 7401-7412. doi:10.1029/97JB03747.

Haimson, B. C., and C. Fairhurst, (1967), Initiation and extension of hydraulic fractures in rocks. *Soc. of Pet. Eng. J.*, September: 310-318. doi:10.2118/1710-PA.

Head, J. W., Pappalardo, R. T., Greeley, R., Sullivan, R. J., Pilcher, C., Schubert, G., Moore, W., Carr, M., Moore, J., Belton, M. (1997), Evidence for recent solid-state convection on Europa: The nature of pits, domes, spots, and ridges. *Bull. Of the Am. Astron. Soc.* 19(3), 983.

Howett, C. J. A., J. R. Spencer, J. Pearl, M. Segura, (2011), High heat flow from Enceladus' south polar region measured using 10-600 cm^{-1} Cassini/CIRS data. *J. Geophys. Res.,* 116. E03003. doi:10.1029/2010JE003718.

Jaeger, J. C., N. G. W., Cook, R. Zimmerman (2007), *Fundamentals of Rock Mechanics*, 4th Edition. Blackwell Publishing, Malden, MA.

Jaumann, R., D. A. Williams, D. L. Buczkowski, R. A. Yingst, F. Preusker, H. Hiesinger, N. Schmedemann, T. Kneissl, J. B. Vincent, D. T. Blewett, B. J. Buratti, U. Carsenty, B. W. Denevi, M C. De Sanctis, W. B. Garry, H. U. Keller, E. Kersten, K. Krohn, J.-Y. Li, S. Marchi, K. D. Matz, T. B. McCord, H. Y. McSween, S. C. Mest, D. W. Mittlefehldt, S. Mottola, A. Nathues, G. Neukum, D. P. O'Brien, C. M. Pieters, T. H. Prettyman, C. A. Raymond, T. Roatsch, C. T. Russell, P. Schenk, B. E. Schmidt, F. Scholten, K. Stephan, M. V. Sykes, P. Tricarico, R. Wagner, M. T. Zuber, H. Sierks, (2012), Vesta's shape and morphology. *Science,* 336, 687. doi: 10.1126/science.1219122.

Kattenhorn, S. A., (2002), Nonsynchronous rotation evidence and fracture history in the Bright Plains region, Europa. *Icarus,* 157, 2, 490-506. doi:10.1006/icar.2002.6825.

Kattenhorn, S. A., Hurford, T. A. 2009. Tectonics of Europa. In: Pappalardo, R. t., Mckinnon, W. B., Khurana, K., eds., Europa, University of Arizona Press, 199-236.

Kay, J. P., and S. A. Kattenhorn, (2010), An open-source GUI for calculating icy moon tidal stresses using SatStress, paper presented at *41ˢᵗ Lunar and Planetary Science Conference*, in Houston, Texas, Abstract #2046.

Kirchoff, M. R., and P. Schenk, (2009), Crater modification and geologic activity in Enceladus' heavily cratered plains: Evidence from the impact crater distribution, *Icarus*, *202*, 656-668. doi:10.1016/j.icarus.2009.03.034.

Martin, E. S. and S. A. Kattenhorn, (2013), Probing regolith depths on Enceladus by exploring a pit chain proxy, paper presented at 44ᵗʰ *Lunar and Planetary Science Conference*, Houston, Texas, Abstract #2047.

Martin, E. S. and S. A. Kattenhorn, (2014), A history of pit chain formation within Enceladus's cratered terrains suggests a nonsynchronous rotation stress field, paper presented at *45ᵗʰ Lunar and Planetary Science Conference,* Abstract # 1083.

McKinnon, W. B., (1999), Convective instability in Europa's floating ice shell. *Geophys. Res. Let.*, 26 (7), 951-954. doi: 10.1029/1999EL900125.

Melosh, H. J., (1989), Impact Cratering a Geologic Process. Oxford University Press, New York. p. 88.

Michaud, R. L., R. T. Pappalardo, and G. C. Collins, (2008), Pit chains on Enceladus: a discussion of their origin, paper presented at *39ᵗʰ Lunar and Planetary Science Conference*, in Houston, Texas, Abstract #1678.

Miller, D. J., A. N. Barnash, V. J. Bray, E. P. Turtle, P. Helfenstein, S. W. Squyres, J. A. Rathbun, (2007), Interactions between impact craters and tectonic fractures on Enceladus and Dione, paper presented at *Workshop on Ices, Oceans, and Fire: Satellites of the Outer Solar System,* Boulder, Colorado, Abstract #6007.

Mitri, G., and A. P. Showman, (2008a), Thermal convection in ice-I shells of Titan and Enceladus. *Icarus,* 193, 387-396. doi:10.1016/j.icarus.2007.07.016.

Mitri, G., and A. P. Showman, (2008b), A model for the temperature-dependence of tidal dissipation in convective plumes on icy satellites: Implications for Europa and Enceladus. *Icarus,* 195, 758-764. doi:10.1016/j.icarus.2008.01.010.

Muller, O. H., and D. D. Pollard, (1977), The stress stat near Spanish Peaks, Colorado determined from a dike pattern. *Pure and Applied Geophysics*, 115, 69-86. doi:10.1007/BF01637098.

Nimmo, F., and R. T., Pappalardo, (2006), Diapir-induced reorientation of Saturn's moon Enceladus, *Nature 441,* 614–616. doi:10.1038/nature04821

Nimmo, F., J. R. Spencer, R. T. Pappalardo, M. E. Mullen. (2007), Shear heating as the origin of the plumes and heat flux on Enceladus. *Nature*, 447 289-291. doi:10.1038/nature05783.

Ojakangas, G. W., Stevenson, D. J. (1989), Thermal state of an ice shell on Europa. *Icarus,* 81, 220-241. doi:10.1016/0019-1035(89)90052-3.

Olgin, J. G., B. R. Smith-Konter, R. T. Pappalardo, (2011), Limits of Enceladus's ice shell thickness from tidally driven tiger stripe shear failure. *Geophys Res. Let.,* 38, L02201. doi:10.1029/2010GL044950.

Pappalardo, R. T., and G. C. Collins, (2005), Strained craters on Ganymede, *J. Struct. Geol.*, *27,* 827-838. doi:10.1016/j.jsg.2004.11.010.

Pappalardo, R. T., J. W. Head, R. Greeley, R. J. Sullivan, C. Pilcher, G. Schubert, W. B. Moore, M. H. Carr, J. M. Moore, M. J. S. Belton, D. L. Goldsby, (1998), Geological evidence for solid-state convection in Europa's ice shell, *Nature*, *391,* 365-368. doi:10.1038/34862.

Pappalardo, R. T., Belton, M. J. S., Breneman, H. H., Car, M. H., Chapman, C. R., Collins, G. C., Dent, T., Fagents, S., Geissler, P. E., Giese, B., Greeley, R., Greenberg, R., Head, J. W., Helfenstein, P., Hoppa, G., Kadel, S. D., Klaasen, K. P., Klemaszewski, J. E., Magee, K., McEwen, A. S., Moore, J. M., Moore, W. B., Neukum, G., Phillips, C. B., Procketer, L. M., Schubert, G., Senske, D. A., Sullivan, R. J., Tufts, B. R., Turtle, E. P., Wagoner, R., Williams, K. K. (1999), Does Europa have a subsurface ocean? Evaluation of the geological evidence. *J. of Geophys. Res.* 104 (E10), 24,015-24,055. doi:10.1029/1998JE000628.

Patthoff, D. A., and S. A. Kattenhorn, (2011), A fracture history on Enceladus provides evidence for a global ocean, *Geophys. Res. Let.*, 38, L18201. doi:10.1029/2011GL048387.

Patthoff, D. A. (2013), Tectonic history of the south polar terrain of Saturn's moon Enceladus and evidence for a global ocean. (Unpublished doctoral dissertation). University of Idaho, Moscow, ID.

Pollard, D. D., and R. C. Fletcher, (2005), *Fundamentals of Structural Geology,* Cambridge University Press, New York. Online Supplemental materials: https://pangea.stanford.edu/projects/structural_geology/ Chapter 6 Scripts.

Porco, C. C., P. Helfenstein, P. C. Thomas, A. P. Ingersoll, J. Wisdom, R. West, G. Neukum, T. Denk, R. Wagner, T. Roatsch, S. Kieffer, E. Turtle, A. McEwen, T. V. Johnson, J. Rathbun, J. Veverka, D. Wilson, J. Perry, J. Spitale, A. Brahic, J. A. Burns, A. D. DelGenio, L. Dones, C. D. Murray, S. Squyres, (2006), Cassini observes the active south pole of Enceladus, *Science,* 311(5766), 1393-1401. doi:10.1126/science.1123013.

Rathbun, J. A., D. M. Janes, S. W. Squyres, (1999), Formation of Beta Regio, Venus: Results from measuring strain. *J. Struct. Geol.* 104(E1), 1917-1927. doi:10.1029/1998/JE900026.

Rathbun, J. A., Musser, G. S., Squyres, S. W. (1998), Ice diapirs on Europa: Implications for liquid water. *Geophys. Res. Let.*, 25. 4157-4160. doi:10.1029/1998GL900135.

Roberts, J.H., and F. Nimmo, (2008a), Tidal heating and the long-term stability of a subsurface ocean on Enceladus. *Icarus* 194(2), 675–689. doi:10.1016/j.icarus.2007.11.010.

Roberts, J.H., and F. Nimmo, (2008b), Near-surface heating on Enceladus and the south polar thermal anomaly. *Geophys. Res. Let.* 35, L09201. doi:10.1029/2008GL033725.

Ross, M., Schubert, G. 1987. Tidal heating in an internal ocean model of Europa, *Nature*, 325, 133-134. doi:10.1038/325133a0

Schenk, P. and M. P. A. Jackson, (1993), Diapirism on Triton: A record of crustal layering and instability. *Geology*, 21. P. 299-302. doi: 10.1130/0091-7613(1993)021<0299:DOTARO>2.3.CO;2.

Schenk, P. and J. M. Moore, (2014), Topography of midsize icy satellites 2: Tethys and the effects of Odysseus, paper presented at *45th Lunar and Planetary Science Conference*, Houston, Texas, Abstract #2598.

Schulson, E. M., and P. Duvall, (2009), *Creep and Fracture of Ice,* Cambridge Univ. Press, Cambridge, U. K., p. 416. doi:10.1018/CBO9780511581397.

Smith-Konter, B., and R. T. Pappalardo, (2008), Tidally driven stress accumulation and shear failure of Enceladus's tiger stripes. *Icarus,* 198, 435-451. doi:10.1016/j.icarus.2008.07.005.

Solomon, S. C., S. E. Smrekar, D. L. Bindschadler, R. E. Grimm, W. M. Kaula, G. E. McGill, R. J. Phillips, R. S. Saunders, G. Schubert, S. W. Squyres, E. R. Stofan, (1992), Venus Tectonics: An Overview of Magellan Observations. *J. Geophys Res.* 97(E8), 13,199-13,255. doi:10.1029/92JE01418.

Spencer, J. R., J. C. Pearl, M. Segura, F. M. Flasar, A. Mamoutkine, P. Romani, B. J. Burrati, A. R. Hendrix, L. J. Spilker, R. M. C. Lopes, (2006), Cassini encounters Enceladus: Background and the discovery of a south polar hot spot. *Science, 311*, (5766), 1401-1405. doi:10.1126/science.1121661.

Spencer, J. R., Howett, C. J. A., Verbiscer, A., Hurford, T. A., Segura, M., Spencer, D. C. (2013), Encleadus heat flow from high spatial resolution thermal emission observations, paper presented at *European Planetary Science Congress,* London, United Kingdom, 8, EPSC2013-840-1.

Spitale, J. N., and C. C. Porco, (2007), Association of the jets of Enceladus with the warmest regions on its south-polar fractures. *Nature*, *449*, 695-697. doi:10.1038nature06217.

Squyres, S. W., Reynolds, R. T., Cassen, P. A., Peale, S. J., (1983), Liquid water and active resurfacing on Europa. *Nature*, 301, 225-226. doi:10.1038/301225a0.

Wahr, J., Z. A. Selvens, M. E. Mullen, A. C. Barr, G. C. Collins, M. M. Selvans, R. T. Pappalardo, (2009), Modeling stresses on satellites due to nonsynchronous rotation and orbital eccentricity using gravitational potential theory. *Icarus, 200(1)*, 188-206. doi:10.1016/j.icarus.2008.11.002.

Wyrick, D., D. A. Ferrill, A. P. Morris, S. L. Colton, D. W. Sims, (2004), Distribution, morphology, and origins of Martian pit crater chains. *J. Geophys. Res., 109,* E06005. doi:10.1029/2004JE002240.

Wyrick, D. Y., D. L. Buczkowski, L. F. Bleamaster, G. C. Collins, (2010), Pit crater chains across the solar system, paper presented at *41st Lunar and Planetary Science Conference*, in Houston, Texas, Abstract #1413.

Chapter 3

Estimating Regolith Thickness on Enceladus Using Pit Chains

Abstract

The cratered terrains of Enceladus's saturnian and anti-saturnian sides have previously been interpreted as ancient, but have been overlooked as tectonized areas despite being heavily dissected by features called pit chains. Enceladus is one of the few places in the outer solar system exhibiting pit chains, which are surface expressions of subsurface dilated fractures underlying a cover of loose regolith. Enceladus may have a uniquely thick cover of loose regolith sourced from the south polar jets which is important to characterize because of its effect on mantling and insulating the surface. We show that pit chains are among the youngest tectonic features on Enceladus's surface and that they can be used to directly infer regolith thickness across these terrains. We infer regolith thickness by measuring the slope angle and diameter of individual pits. We find that the slope angle varies spatially indicating a range of regolith cohesion. The distribution of pit depths (inferred from pit diameter and slope angel) indicate a heterogeneous distribution of regolith thicknesses across the surface.

3.1 Introduction

Enceladus's jet activity [*Porco et al.,* 2006] and thermal anomaly [*Spencer et al.,* 2006] within the south polar terrain (SPT) make Enceladus one of the few geologically active bodies in the solar system. These jets act as the primary source of fall-back material mantling Enceladus's surface, which may, in part, contribute to the observed muted morphologies (Fig 3.1) of craters [*Bray et al.,* 2007; *Kirchoff & Schenk,* 2009; *Bland et al.,* 2012] and tectonic structures.

Initial crater   Mantling of regolith   Further mantling
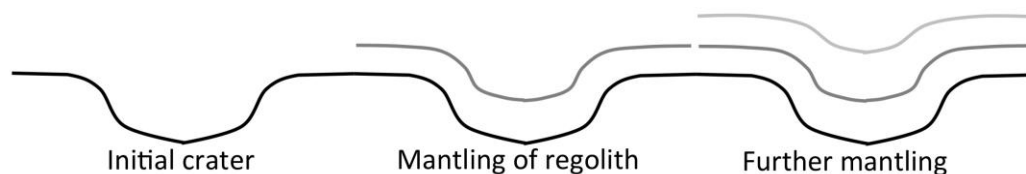
Figure 3.1: Schematic illustrating mantling of a surface by plume fall-back onto a crater. From right to left, an initial crater that is mantled with plume fall-back appears smaller and more shallow. Further mantling continues to diminish the appearance of the crater. This same processes would mute or diminish any surface topography or features.

Fall-back material creates a layer comprised of loose particles on the surface that we hereafter refer to as regolith. Regolith may be sourced from impact events, fall-back from E ring particles, and fall-back from the plumes themselves, however, the distribution and thickness of the regolith, regardless of source, is poorly understood. *Michaud et al.* [2008] first estimated an average regolith thickness across Enceladus's surface of ~250 m using features called *pit chains* (Fig. 3.2) and experimentally determined proxy by *Horstman & Melosh,* [1989]. This proxy suggests that regolith depth has a 1:1 correlation with average spacing between individual pits [*Horstman & Melosh,* 1989]. Regolith thicknesses are likely to vary spatially due to variations in jet localities and eruptive directionality [*Spitale & Porco*, 2007]. Based on jet localities and orientation, *Kempf et al.* [2010] model regolith deposition rates and infer increasing regolith thicknesses with increasing proximity to the SPT.
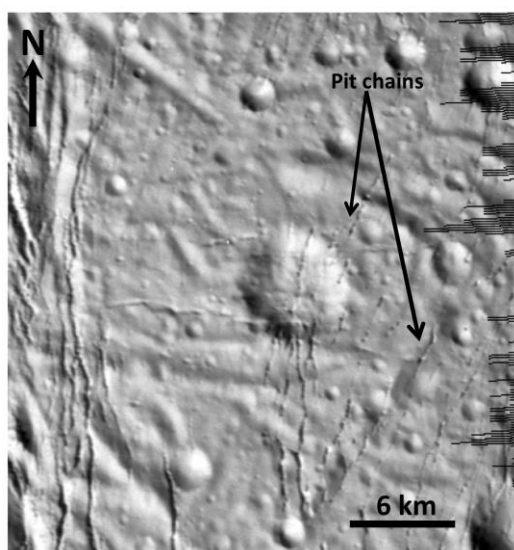
Figure 3.2: (a) Pit chains on Enceladus are composed of collinear isolated pits, highlighted by arrows. Image No. N1489050144.

The thickness of regolith cannot be detected remotely; therefore, an accurate method for measuring regolith thickness is needed that is capable of resolving variations in thickness across the surface which is important for determining whether the surface has been significantly modified by a layer of regolith. Regolith can act to mute surface morphologies by filling in topographic low points, eliminate short wavelength topography, and soften topographic highs. A mantled surface can closely resemble viscous relaxation, which in the case of craters would act to shallow craters and up-dome floors [*Smith et al.,* 1982; *Passey,* 1983; *Bland et al.,* 2012] (Fig. 3.1). If regolith thicknesses are found to be high across the surface, muted surface morphologies may have undergone less viscous relaxation than previously predicted [*Bland et al.,* 2012] which might require reexamining estimated heat flows based on surface feature morphologies. The processes by which the surface of Enceladus is being modified is essential to no only characterizing surface modification processes on Enceladus, but also constrain models to better estimate heat flow. We aim to characterize the global distribution of pit chains, their relative age

relationship with respect to other features and terrain types on the surface of Enceladus, and ultimately refine a method by which regolith depths (and distributions) can be measured.

3.2 Pit chains

Pit chains are linear troughs made up of circular to elliptical depressions [*Wyrick et al.,* 2004; *Ferrill et al.,* 2004; 2008] (Fig. 3.2). Individual pits and pit chains are distinguishable from impact craters and crater chains in that they lack raised crater rims, impact ejecta, or flow features [*Wyrick et al.,* 2004; *Michaud et al.,* 2008], such as those visible in impact generated pit crater chains like the Enki Catena crater chain on Ganymede [*Schenk et al.,* 1996]. Pit chains have been described on Venus [*Bleamaster & Hansen,* 2004], Earth [*Okubo & Martel,* 1998; *Ferrill et al.,* 2004, 2008; 2011], Mars [*Wyrick et al.,* 2004; *Ferrill et al.,* 2004, 2008], and several small solar system bodies, including Phobos [*Thomas,* 1979], Eros [*Prockter et al.,* 2002; *Buczkowski et al.,* 2008], Gaspra [*Veverka et al.,* 1994], Ida [*Sullivan et al.,* 1996], and Vesta [*Buczkowski et al.,* 2012a, b; 2013] [*Wyrick et al.* 2010]. A review by *Wyrick et al.* [2010] suggests pit chains may also exist on Europa, Ganymede, and Dione. However, the only documented occurrence of pit chains in the outer solar system is on Enceladus [*Michaud et al.,* 2008; *Wyrick et al.,* 2010] and possibly Tethys [*Schenk & Moore,* 2014].

3.2.1 Locations

Pit chains on Enceladus have previously been identified almost exclusively within the cratered terrains [*Michaud et al.,* 2008] and have been interpreted to be young. However, we observe pit chains at all stages of formation (see sections *3.2.2* and *3.2.3)* overprinting regions of the tectonized terrains (Fig. 3.3 a, b) [*Martin & Kattenhorn,* 2014] which are inferred to be relatively younger, 0.02-2 Ga [*Kirchoff & Schenk,* 2009], based on the low frequency of craters. We also find pit chains crosscutting the south polar dichotomy (Fig. 3.3 c, d), the northern boundary of the SPT, inferred to be geologically young region based on its association with the geologically active SPT. Therefore, pit chains crosscutting the south polar dichotomy imply that at least some stages of pit chain formation have occurred recently. Pit chains are also found at the boundaries between the cratered terrains and the

tectonized terrains (Fig. 3.3 e, f). While the general lack of pit chains in the tectonized terrains is intriguing, we focus here on the cratered terrains, where the densest populations of pit chains occur.
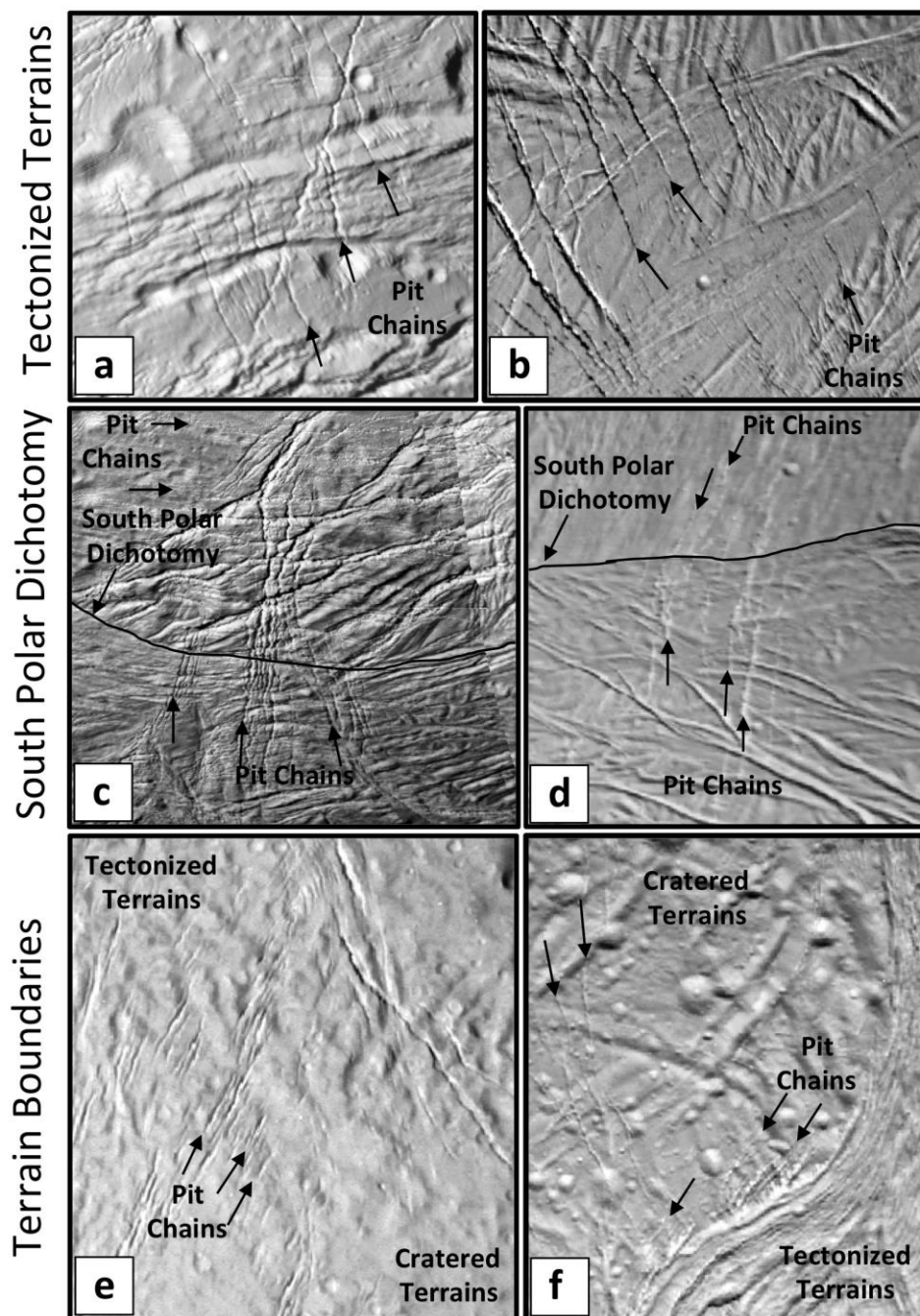
Figure 3.3: Pit chains are among the youngest features on the surface of Enceladus and are not restricted to the cratered terrains. (a, b) Pit chains crosscutting the tectonized terrains, which are considered to be young based on the general dearth of craters. (c, d) Pit chains overprint the geologically young south polar dichotomy, encompassing the south polar terrain. (e, f) Pit chains are also found at terrain boundaries, commonly in en echelon arrays. Cassini image numbers: (a) N1637465942; (b) N1487300854; (c) N1652859224; (d) N1487300107; (e) N1652863294; (f) N1487300482.

3.2.2 Formation mechanisms

Pit chains across the solar system can form by a variety of mechanisms, including collapse of a carapace above lava tubes, extension fractures, dilational faulting, karst dissolution, and dike intrusions associated with exsolved volatiles, cryosphere interactions, or plinian-style eruptions [*Wyrick et al.,* 2004]. On Mars, motion along high-angle normal faults underlying loose regolith likely causes drainage of overlying regolith into the resultant dilational space along the fault plane, forming approximately linear chains of pits [*Wyrick et al.,* 2004] (Fig. 2.4). Similarly, *Michaud et al.,* 2008 explored the range of formation mechanisms [*Wyrick et al.,* 2004] for pit chains on Enceladus. The absence of cryovolcanic features outside of the south polar terrains and a lack of preferred sources from which pit chains radiate, eliminate dike-related formation processes [*Michaud et al.,* 2008].
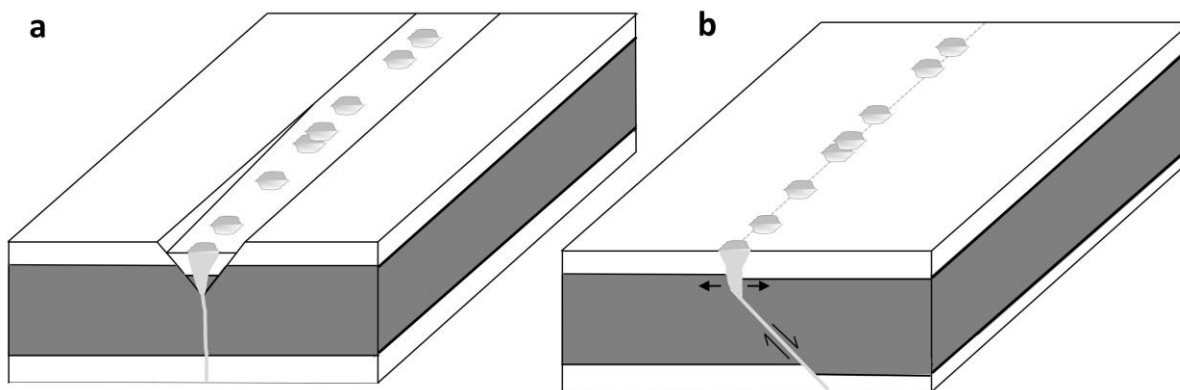
Figure 3.4: Conceptual formation mechanism for pit chains after *Wyrick et al.* **[2004]. Pit chains on Enceladus may form due to extension fracturing (a) or dilational faulting (b). (a) A subsurface tension crack overlain by a layer of loose regolith crates a void for which regolith to drain into creating pits. (b) Subsurface dilational faulting (subsurface fault indicated by the dashed line) is vertical near the surface creating a dilatational space (***e.g., Michaud et al.* [2008]).**

Additionally, collapse of lava tubes is unlikely for similar reasons: tubes tend to be non-linear in nature and converge on a single point source of origin which have not been observed for pit chains on Enceladus [*Michaud et al.,* 2008]. *Michaud et al.* [2008] therefore attribute the formation of pit chains on Enceladus in an analogous manner to those on Mars, formed by drainage of a layer of regolith created by plume fall-back and E ring material deposition into an underlying void related to dilational faulting (Fig. 3.4b) or extension fractures (Fig. 3.4a). This conclusion is consistent with experiments replicating pit chain formation [*Horstman & Melosh,* [1989; *Ferrill et al.* 2004]. We therefore consider pit chain formation

due to extension fractures or dilational faulting to be the most likely mechanism by which pit chains on Enceladus form.

3.2.3 Pit chain evolution

Pit chain formation due to extension fractures or dilational faulting is the favored formation mechanism for pit chains on Mars [*Wyrick et al.,* 2004]. This conclusion is consistent with experimental models whereby pit chains form by drainage of loose regolith into a dilational space [*Horstman & Melosh,* 1989; *Ferrill et al.,* 2004], the deformational sequence begins with the formation of individual, isolated pits (Fig. 3.5a) [*e.g. Nahm & Kattenhorn,* 2014].
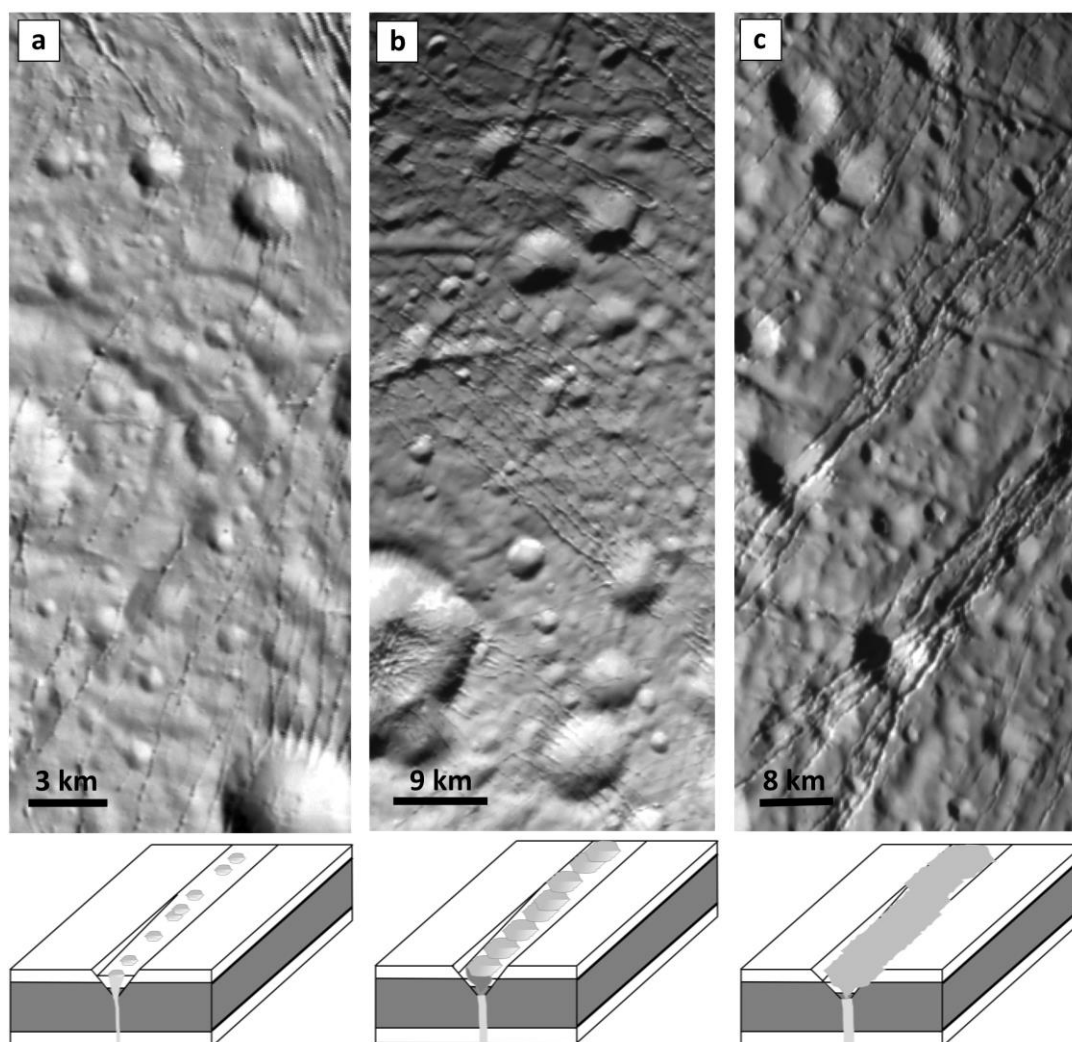
Figure 3.5: Examples of the three primary stages of pit chain evolution [*e.g., Michaud et al.,* 2008; *Nahm & Kattenhorn,* 2014; *Ferrill et al.,* 2004]. Block diagrams below each image illustrate the effect of increased dilation that result in (a) chains of isolated pits indicating the earliest stages of pit chain evolution. Image No. 1489050078. (b) Pit chains comprised of partially merged pits representing the intermediate stages of formation. Image No. N1500061010. (c) Fully merged pit chains characterized by scalloped edges along the trough rim are the most evolved stage of pit chain formation. Image No. N1500061010.

Continued dilation at the surface caused by ongoing dilation on the underlying normal fracture causes individual pits to increase in diameter and ultimately coalesce to become more elliptical, forming partially-merged pit chains (Fig. 3.5b). In the most evolved stages, related to the largest amounts of dilation and normal fault displacement, fully-merged pit chains form scalloped rims where individual pits can no longer be resolved (Fig. 3.5c) [*e.g. Michaud et al.,* 2008].

3.3 Regolith on Enceladus

3.3.1 Significance of regolith depth

The regolith may also be acting as a thermally insulating layer [*Bland et al.,* 2012], thus it is important to develop an accurate way of estimating the distribution of regolith. Resolving the regolith depth distribution across Enceladus's surface has implications for Enceladus's thermal history. Many craters within the cratered terrains exhibit subdued or relaxed morphologies [*Porco et al.,* 2006; *Bray et al.,* 2007; *Kirchoff & Schenk,* 2009; *Bland et al.,* 2012] attributed, in part, to viscous relaxation [*Kirchoff &* Schenk, 2009; *Bland et al.,* 2012]. However, mantling of the surface by E ring and plume material could also give craters a muted or relaxed appearance. In a study of 460 mapped craters [*Bray et al.,* 2007], 40% of the observed craters appeared to have undergone some amount of thermal relaxation or infill. The subdued appearance of these craters may have a latitudinal dependence; craters become increasingly more subdued south of 30°N, particularly south of 20°S [*Bray et al.,* 2007], which correlates well with regolith deposition models of *Kempf et al.* [2010], in which the amount of regolith on the surface increases with proximity to the SPT.

Moreover, Enceladus lacks a population of craters ≤2 km in diameter and ≥6 km in diameter as compared with other Saturnian satellites [*Kirchoff & Schenk,* 2009]. It is presumed that infilling of craters by plume fall-back is capable of erasing the smaller population (≤2km) of craters [*Bray et al.,* 2007; *Kirchoff & Schenk,* 2009]. However, neither infilling of craters by plume fall-back, nor viscous relaxation with high and constant heat fluxes, can independently completely erase the larger (≥6 km) population of craters [*Bland et al.,* 2012]. A combination of infilling and viscous relaxation may be able to erase craters of this size but is difficult with the currently estimated heat flows (~150 mWm^{-2}) and maximum

rates of regolith deposition regolith (10^{-3} mm yr^{-1}) [*Bland et al.,* 2012]. If the thickness and distribution of regolith on Enceladus can be measured, than estimates of the amount of relaxation craters has experienced may be revised: a heavily muted crater that is associated with a thick deposit of regolith will have the appearance of also being viscously relaxed. If the depth of the regolith is known at that location it can be subtracted from the apparent depth of the crater and the amount of relaxation the crater has experienced can be refined. Therefore the estimated heat flows that the surface has experienced may be improved upon. Additionally, large amounts of regolith may have an insulating effect making the temperature of the top portion of Enceladus's lithosphere warmer [*Bland et al., 2012*; *Passey & Shoemaker*, 1982; *Passey,* 1983]: Enceladus's surface temperature of 70 K may be nearer 120 K [*Bland et al.,* 2012; *Passey & Shoemaker,* 1982] which could aid in refining parameters for future theoretical explorations.

3.3.2 Sources of deposition

Regolith deposited on the surface of Enceladus may have originated from three different sources including plume fall-back, deposition of E ring material, and impact generated regolith. The jets are estimated to eject >150 kg/s [*Hansen et al.,* 2006], however models of jets only predict the deposition rates of fall-back directly to the surface [*Kempf et al.,* 2010]. *Kempf et al.,* [2010] model the fate of particles in the plumes of Enceladus, and find that ~10% of the material from each modeled jet escapes to the E ring, however no estimates were made of the fate of E ring particles once they have reached the ring. Additionally, impact ejecta is a likely source of regolith within the cratered terrains, but is not considered in models of regolith deposition [*Kempf et al.,* 2010]. However we may attempt to constrain the formation of impact generated regolith. Impact generated regolith on Earth's moon may vary from less than 10 meters [*Quaide & Oberbeck,* 1968; *Bart et al.,* 2011] to up to 30 meters in thickness [*Wilcox et al.,* 2005]. These regolith thicknesses are not negligible and must be considered when examining results from measurements of regolith thicknesses on Enceladus. The deposition of regolith on Enceladus's surface has a direct impact on the morphology of the surface and surface features. However, there is no direct way of estimating how long plume activity has been occurring, whether it occurs periodically or randomly, or whether Enceladus has experienced changing jet locations or directivity.

3.3.3 Predicted deposition rates

Models of regolith distribution across Enceladus's surface by *Kempf et al.* [2010] assume a single source of regolith production from Enceladus's plume activity. They find that fall-back from Enceladus's plumes is deposited more widely over the cratered terrains, with deposition rates as high as 1 mm/year nearest the south pole to as low as 10^{-5} mm/year north of 55°S. Interestingly however, there is also a depositional preference towards longitudes nearer the cratered terrains leaving the tectonized terrains north of the south polar dichotomy nearly untouched by regolith [*Kempf et al.,* 2010]. A 10 m-wide boulder would be completely covered in 10^5-10^6 years by a plume 100 m away [*Kempf et al., 2010*]. By analogy, a crater that is several hundreds of meters deep may be covered (but not buried) by a mantling of regolith in tens of millions of years, assuming plume activity has been continuous. However, *Kempf et al.* [2010] use a density close to that of pure water ice (900 kg/m^3) for fall-back particles, similar to that of glacial ice, which has a density of 830-917 kg/m^3 [*Cuffey & Paterson,* 2010]. New snow has a much lower density of 50-70 kg/m^3 and settled snow is closer to 200-300 kg/m^3 [*Cuffey & Paterson,* 2010]. If the volume of water exiting the plumes is >150 kg/s [*Hansen et al.,* 2006] remains constant, a lower density like that of new snow or settled snow might result in a greater regolith thickness. Therefore, the total accumulation of fall-back material estimated from *Kempf et al.* [2010] maybe an underestimation, but provides a useful model of predicted distribution and lower limits on regolith deposition rates.

3.4 Mapping

3.4.1 Data

High-resolution images (40-200 m/pixel) from the Cassini Imaging Science Subsystem (ISS) camera were used to produce global-scale, detailed maps of the distribution of pit chains exclusively across Enceladus. Raw images from the Planetary Data System (PDS) were processed using the USGS's Integrated Software for Images and Spectrometers (ISIS). Individual images were superimposed on a global mosaic of Enceladus [*Roatsch et al.,* 2013]. Features were mapped in an ArcGIS environment in a simple cylindrical projection.

3.4.2 Pit Chain Sets

Detailed fracture maps highlight the distribution and orientation exclusively of pit chains. All mapped pit chains were found to crosscut, and thus post-date, the formation of most craters as well as any tectonized terrains. Individual pit chains were mapped into *sets* based on their orientation and morphology. Fractures with similar orientations (within ±5°) were assigned to sets, based on the reasoning that similar orientations reflect the same stress conditions, implying temporal affinity. Isolated pit chains, partially-merged pit chains, and fully-merged pit chains were not mapped separately, but were included together within defined sets based on orientations. Nonetheless, these classification criteria were used to distinguish pit chains from other, trough-like or linear trough fractures [*e.g., Nahm & Kattenhorn,* 2014].
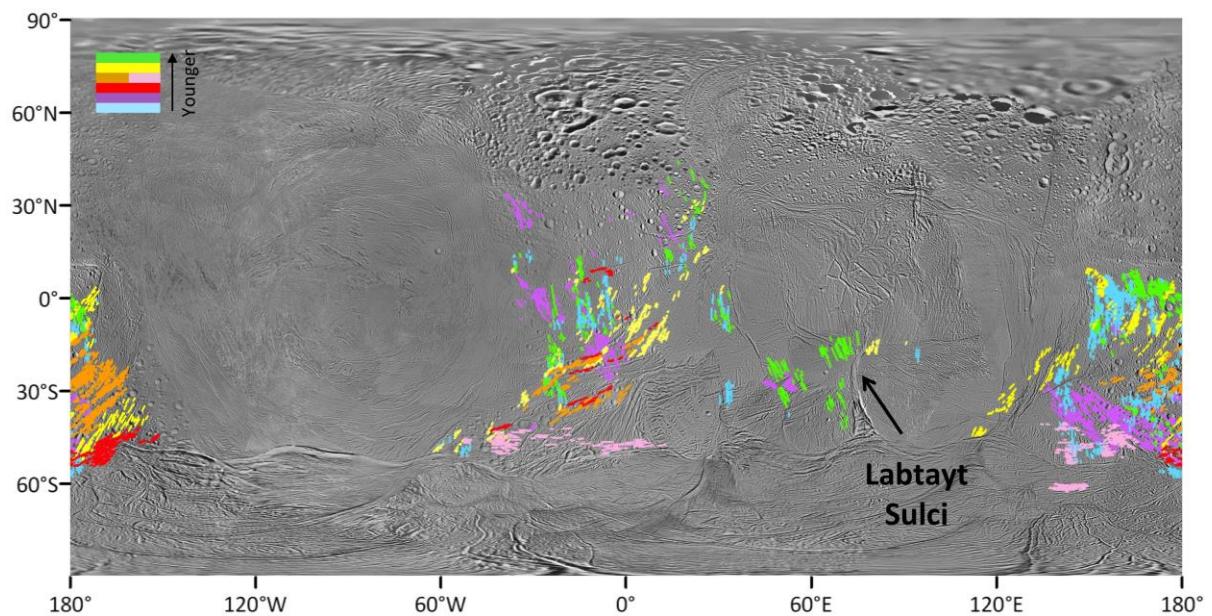
Figure 3.6: Results of global pit chain mapping. Pit chains are concentrated mostly within the cratered terrains, but some are observed within the trailing hemisphere tectonized terrains. Each pit chain is color coded to represent pit chain set, and relative age sequence from the first pit chain set to form to the earliest set of pit chains is blue, purple, red, orange, yellow, and green. Basemap credit: NASA/JPL-Caltech/SSI; *Roatsch et al.,* [2013].

Once pit chains sets were established, crosscutting relationships were used to determine a relative age sequence among the identified sets. Examples of crosscutting relationships include a pit chain terminating perpendicularly against a pre-existing pit chain, or curving to become parallel with the pre-existing fracture [e.g. *Cruikshank & Aydin*, 1995]. This

technique was similarly employed within the SPT by *Patthoff & Kattenhorn* [2011]. However, image resolution constraints, as well as limited contacts between individual pit chain sets with respect to one another, make it difficult to verify the relative age relationship of each pit chain set, especially between those on opposing cratered terrains that are separated by large expanses of tectonized terrain. Mapping was performed independently on each of the antipodal, cratered terrains to avoid bias when identifying pit chain sets. Hence, there were no preconceived assumptions about the orientations of sets within the opposing cratered terrains.

Global mapping of pit chains (Fig. 3.6) reveals a predominance of pit chains within the cratered terrains as noted by *Michaud et al.* [2008]. We additionally observe a population of pit chains in the tectonized terrains on the trailing hemisphere. Despite the limited presence of pit chains within the tectonized terrains, however, the affinity between cratered terrains and pit chains raises two important points: (1) cratered plains have a seemingly abundant mantle of loose regolith; and (2) the cratered plains are in the process of being dissected by pit chains despite the conventional assumption that they are not tectonized.

Fig. 3.6 illustrates the global distribution of pit chains across Enceladus. These maps also reveal a prolonged history of pit chain formation, with successive sets of pit chains showing a progressive change in orientation through time. Within each pit chains set, all states of evolution of pits are represented, regardless of where the set falls within the age sequence [*Martin & Kattenhorn,* 2014]. There are seven independent pit chain sets with distinct orientations. Sets from oldest to youngest are blue, purple, red, orange, yellow, and then green. This indicates that the orientation of pit chains changes temporally and progressively rotates through time. We interpret this pattern of pit chains to be consistent with forming in a nonsynchronous rotation stress field and is consistent with observations of fracture patterns within the south polar terrain [*Patthoff & Kattenhorn,* 2011]. In particular, a nonsynchronous rotation stress field can produce the anti-podal fracture patterns, where pit chains sets with similar orientations fall in the same place within the established relative age sequence. If nonsynchronous rotation is the mechanism for producing the patterns of pit chains, it would require 135° of rotation to form all 7 pit chain sets. An additional 120° of ice shell rotation would be required to bring the cratered terrains to their present longitude.

Table 3.1: A comparison of estimates of regolith thicknesses based on different methods. The average pit spacing method originates from experimental work by *Horstman & Melosh* [1989] whereas the assumed angle of repose method is based off work in-part by *Veverka et al.* [1994]. Measurements of regolith thickness by both methods for Eros and Gaspra are within an order of magnitude of one another.

Body	Regolith Thickness Method		Reference
	Average Pit Spacing	Assumed Angle of Repose	
Gaspra	~200 m	60-300 m	*Veverka et al.* [1994]
Ida	-	~30 m	*Sullivan et al.* [1996]
Phobos	~290-300 m	-	*Horstman & Melosh* [1989]
Eros	<100 m	30 m	*Prockter et al.* [2002]
Enceladus	250 m	-	*Michaud et al.* [2008]

3.5 Measuring regolith thickness

Observations of the small bodies Gaspra, Ida, Phobos, and Eros have all revealed the presence of pit chains (also called grooves, or pitted grooves), which likely form through a similar process by the drainage of loose regolith into an open fissure [*Horstman & Melosh*, 1989; *Veverka et al.,* 1994; *Sullivan et al.,* 1996; *Prockter et al.,* 2002]. These studies used two methods employing pit chains to estimate the amount of regolith on the surface (Table 3.1), which we divide these methods into two categories: the Average Pit Spacing method (Fig. 3.7a) and the Assumed Angle of Repose method. We compare these two methods with that of *Wyrick et al.,* [2004] who use sun angle and an assumed pit geometry to infer pit slope angle (i.e. inferred angle of repose), which we refer to as the Slope Angle method (Fig. 3.7b).

3.5.1 The Average Pit Spacing method

Horstman & Melosh, [1989] experimentally derived the Average Pit Spacing method by covering two ridged plates placed edge-to-edge with an overlying layer of material resembling regolith. The two plates were pulled apart to mimic a dilating fracture. They find a one-to-one correlation between regolith thickness and pit spacing (i.e., the distance between adjacent pit centers is equal to the thickness of the regolith at that location) at the point in time when the maximum number of pits had formed (Fig. 3.7a). This correlation is

independent of regolith density, grain size or shape, or angle of repose. Developed initially to assess the depth of regolith on the surface of Phobos, the Average Pit Spacing method for regolith thickness has been employed on Gaspra [*Veverka et al.,* 1994], Eros [*Prockter et al.,* 2002], and Enceladus [*Michaud et al.,* 2008].
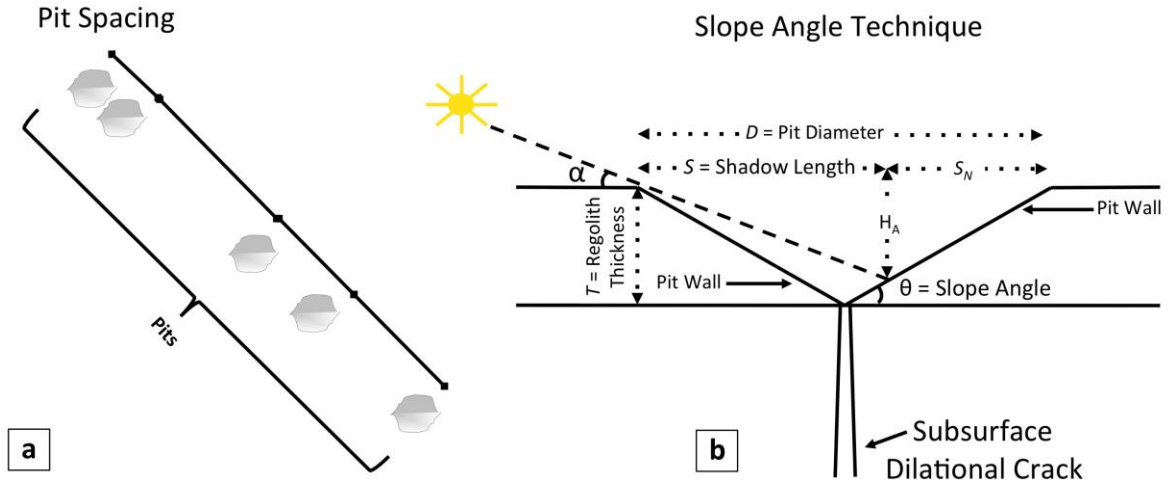
Figure 3.7: Techniques for estimating regolith thickness. (a) The Average Pit Spacing method [*Horstman & Melosh,* 1989]. (b) The Slope Angle method [*Wyrick et al.,* 2004] uses the sun angle (α), pit diameter (D), shadow length (S), length not in shadow (S$_N$), apparent height (H$_A$) to geometrically determine the slope angle (θ) of individual pits, which are assumed to be at the angle of repose at that location. Regolith thickness (T) is then determined trigonometrically.

3.5.2 The Assumed Angle of Repose method

The Assumed Angle of Repose method from *Veverka et al.,* [1994] uses pit chains on Gaspra to estimate regolith thicknesses by measuring the fracture width and assuming an angle of repose of the regolith (30°):

$$T = \left(\frac{w_f}{2}\right)\tan(\theta) \tag{1}$$

where T is the regolith thickness, w_f is the width of the fracture, and θ is the angle of repose. This technique was also employed for Ida [*Sullivan et al.,* 1996] and Eros [*Prockter et al.,* 2002], but cannot resolve spatial variability in regolith thickness across a surface, and requires assumptions about the nature of the regolith by estimating an angle of repose.

3.5.3 The Slope Angle Method

We use the technique of *Wyrick et al.*, [2004] to calculate regolith depths in the vicinity of mapped pit chains. This method assumes pits are shaped like circular right cones (the apex of the cone sits above the center of its circular base) (Fig. 3.7b). Given the sun angle, α, (90º minus the incidence angle), the measured pit diameter D, and the measured length of the shadow within the pit, S, the slope angle of the pit θ (i.e., the inferred angle of repose) can be calculated. The fraction of the pit not in shadow:

$$S_N = D - S \tag{2}$$

The apparent height of the pit is

$$H_A = S \tan \alpha. \tag{3}$$

The slope angle of the pit can then be determined using

$$\theta = \tan^{-1} \left[\frac{H_A}{S_N} \right]. \tag{4}$$

The thickness of the regolith is then

$$T = \left(\frac{D}{2} \right) \tan \theta. \tag{5}$$

3.5.4 Measurements

To compare, and test results from the Slope Angle method *Wyrick et al., [2004]* with that of the Pit Spacing method and the Assumed Angle of Repose method, measurements of pit spacing and pit diameter were required. Pit spacing was measured from the center of one pit to the center of another pit within a single pit chain. Because pits were assumed to be circular right cones, pit diameters were only measured on individual pits that appeared circular at the image resolution. The circle option within the polygon editor in ArcGIS was used to draw the edge of the pit on images in a simple cylindrical projection, from which the diameter of each

pit could be measured. Shadow lengths from inside the pit were measured in the direction of the sun azimuth, and the sun angle was obtained from the Planetary Data System header files.

3.6 Results

3.6.1 Regolith Thicknesses

The Pit Spacing method was used to calculate regolith thicknesses globally at locations where continuous chains of pits were observed. Pit spacing measurements resulted in a range of inferred regolith thicknesses from 377-1280 m (Fig. 3.8a). In contrast, in the Assumed Angle of Repose method, if a general angle of repose of loose sand (35°) is used, the range of regolith thickness is 195-432 m (Fig. 3.8b). Although both methods show similar ranges of regolith thickness within the same set, the Assumed Angle of Repose method shows more consistent regolith thicknesses within individual sets than the Pit Spacing method, which can be attributed to unevenly spaced pits within individual chains. The Slope Angle method [*Wyrick et al.* 2004] (Fig. 3.9) provides a more accurate estimate of regolith thickness at each pit, resulting in a range of inferred regolith thickness from 29-1640 m (Fig. 3.10). While this range is broad, most depths are distributed between 60 and 480 m; only 12% of the measured pits fall above this range. *Michaud et al.* [2008] used the Pit Spacing method to determine an average regolith depth of 250 m ±20 m across the cratered terrains, which falls within the range of depths measured across individual pits using individual slope angles.

Using the Slope Angle method, we measure slope angles (≈ angles of repose of the regolith) ranging from 10°–80° (Fig. 3.10a) with an average slope angle of 35°, which is similar to that of loose sand and consistent with observations of slope angles on Mars [*Wyrick et al.,* 2004]. These slope angles are distributed heterogeneously across Enceladus's surface, with generally lower angles in the cratered terrains and higher angles in the tectonized terrains.
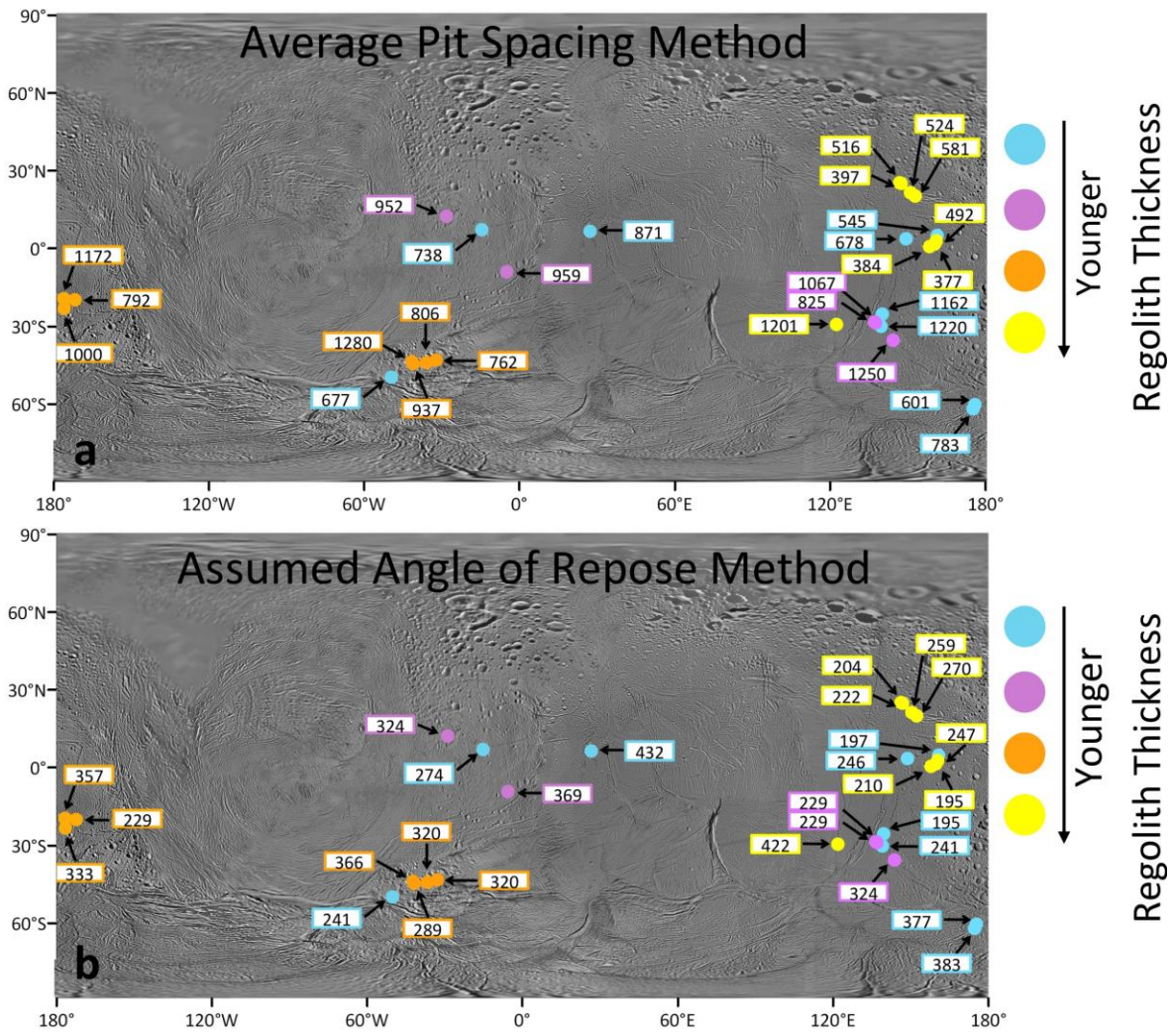
Figure 3.8: Results of regolith thicknesses inferred from the Average Pit Spacing and Assumed Angle of Repose method. Data from these proxies is overlain on a global mosaic of Enceladus courtesy of CICLOPS; Credit: NASA/JPL-Caltech/SSI; *Roatsch et al.,* [2013]. (a) The regolith thickness determined from the Average Pit Spacing method measured in meters. (b) The pits measured for the Assumed Angle of Repose method color coded by pit chain set. Colors indicate the pit chain set to which each pit belongs.
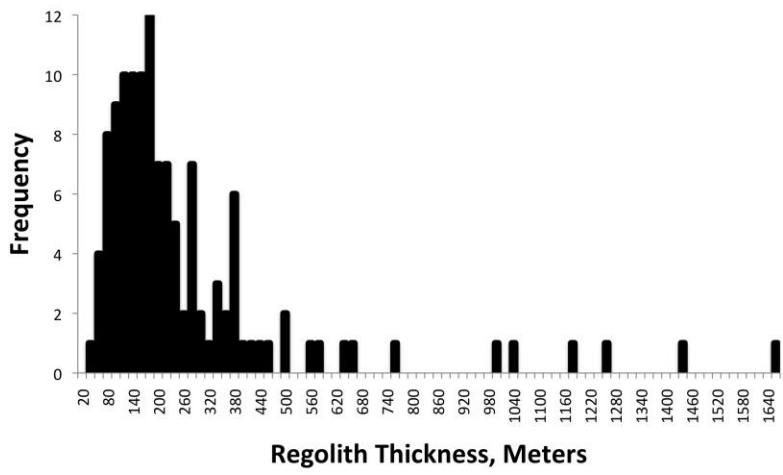
Figure 3.9: Histogram of regolith thickness from the Slope Angle Method.
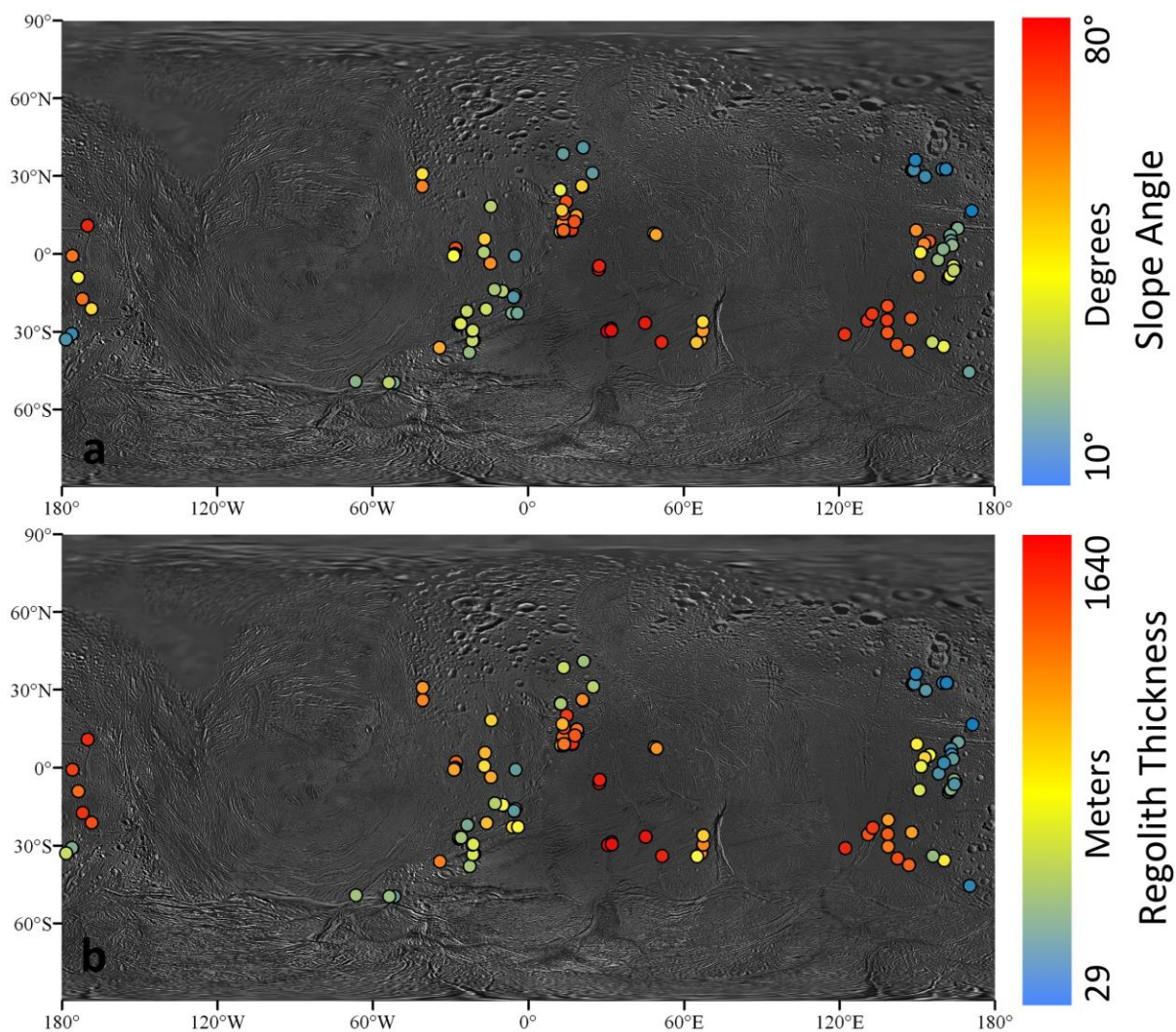
Figure 3.10: Results from the Slope Angle method [*Wyrick et al.,* 2004]. Before regolith thickness could be calculated, the slope angle had to be measured. (a) shows the distribution of slope angles measured for individual pits. Slopes angles range from 10°-80°. (b) Results of regolith thickness inferred from the Slope Angle method showing the thicknesses range from 29-1640 m.

3.7 Discussion

Using the Slope Angle method allows for more accurate measurements of regolith thickness at each pit, however, this technique revealed slope angles from 10°-80°. Then average angle of repose of loose sand is ~35°, so slope angles of up to 80° is difficult to reconcile for regolith on the surface assumed to be unconsolidated. Fig. 3.10 also demonstrates that higher slope angles in general relate to thicker regolith deposits. These regions of thicker regolith do not necessarily indicate that the total regolith accumulating is presently unconsolidated material. It is possible that regolith has annealed over time, and

reactivation of the underlying fracture would modify the original pit. This resulting geometry is inconsistent with the assumed pit geometry of a circular right cone, but may reconcile many of the steep sided pits inferred from the Slope Angle method. Therefore the method in which the regolith thickness was inferred may not be appropriate for these conditions, however image resolution is not sufficient to resolve pit geometry.

Pit chains on Enceladus are the likely result of dilational faulting or extensions fractures, which require a layer of loose regolith overlain a subsurface crack. Our detailed mapping of pit chains reveal a global distribution that extends over a wide range of latitudes, reaching as far as 55°N and as far south as to crosscut the south polar dichotomy. Pit chains may reach further north, however resolutions are not sufficient to resolve these features. The highest density of pit chains are found within the cratered terrains (Fig. 3.6) which suggests that the cratered terrains are overlain by a significant layer of regolith with a broad latitudinal extent. While pit chains have not been extensively observed within the tectonized terrains, their absence is not diagnostic of a lack of regolith.

The established history of pit chain formation (Fig. 3.6), where sets of pit chains formed with distinct orientations through time, indicates that there is a recorded history of tectonic deformation of the cratered terrains, which are overlooked as being heavily tectonized. If the pit chains require a minimum of 135° of ice shell rotation to form, and another 120° of ice shell rotation to reach their current longitude, than it can be inferred that the ice shell has rotated a minimum of 255°. If the nonsynchronous rotation period is on the order of 1 Myr (consistent with *Patthoff & Kattenhorn,* 2011 and *Martin & Kattenhorn,* 2014) than it would have taken a minimum of 708,000 years from the beginning of pit chain formation to their rotation into their current location. Pit chains are geologically young features, which suggests that the cratered terrains have recently undergone tectonic deformation. Since pit chains require the presence of regolith in order to form, their formation postdates regolith formation suggesting that perhaps regolith formation occurred longer than 708,000 years ago. The various stages of pit chain evolution observed within each set may also indicate that the tectonic dissection of the cratered terrains has been contemporaneous with the emplacement of regolith over some length of time.

Pit chains provide a tool with which to determine the depth of the regolith in which they form. We compared the results of measurements of regolith thickness from three different

techniques, the Average Pit Spacing method, the Assumed Angle of Repose method, and the Slope Angle method. The Assumed Angle of Repose method (Fig. 3.8b) gave more consistent results within individual pit chain sets than the Average Pit Spacing method (Fig. 3.8a). *Wyrick et al.* [2004] shows a wide range of measured pit slope angles ranging from 9°-74° for pits on Mars suggesting differences in the nature of the regolith across the surface. Using the Assumed Angle of Repose is unable to accommodate differences in angles of repose across a surface. Additionally, the Average Pit Spacing method is based of experimental work that does not accurately reflect how fractures form. Fractures are typically segmented, with the maximum amount of opening occurring in the center of the fracture, decreasing toward each fault tip. As fractures propagate, fracture segments merge, creating fracture patterns that are more complex than an idealized single, continuous crack. Furthermore, these studies provide no physical basis for the relationship between pit spacing and regolith depth. Moreover, this relationship was not observed in subsequent analog studies [*Ferrill et al.,* 2004]. Our observations of pit spacing on Enceladus reveal inconsistent spacings within a single pit chain, and we therefore determine that the Slope Angle method provides a far more accurate representation of regolith thicknesses across the surface.

A comparison of our results for regolith thicknesses with those determined from models of plume deposition rates [*Kempf et al.,* 2010] shows a good agreement [Fig. 3.11], primarily within the anti-Saturn cratered terrains. Lower deposition rates (and thicknesses) from *Kempf et al.,* [2010] models correlate well with regolith thicknesses inferred from the Slope Angle method (Fig. 3.9 and 3.10) [*Wyrick et al.,* 2004]. This correlation is less pronounced on the sub-Saturn side and are offset from the modeled results by 30°–60° in longitude (Fig. 3.11). Measured regolith depths from the Slope Angle method show a latitudinal dependence of regolith thickness on the anti-Saturn side, lower thicknesses are found with increasing distance from the SPT consistent with *Kempf et al.,* [2010]. This result is also consistent with observations of muted craters by *Bray et al.* [2007] who find less muted craters further from the SPT consistent with shallower regolith depths.

The maximum plume fall-back deposition rates modeled by *Kempf et al.* [2010] are 1 mm/yr within the SPT. The lowest deposition rates are 10^{-5} mm/yr, reaching as far north as 55°N. The maximum regolith thickness that we calculated is 1640 m located at 30.6°E and 29.8°S. Based on the range of fall-back accumulation rates of *Kempf et al.* [2010], it would

take between 1 Myr to 164 Gyr to deposit this amount of regolith. 480 m of regolith deposited at the lowest deposition rates would require 48 Gyr. Clearly, the lower end of the inferred fall-back accumulation rates are not capable of explaining regolith thickness, even on the time scale of the solar system. Moreover, given the dearth of fresh craters in regolith material in the cratered terrains and the muted morphology of the majority of the craters, as well as the likelihood of annealing of loose regolith over long time periods in response to Enceladus's heat flow, it seems unlikely that the loose regolith thickness we measure represents accumulation over the entire history of Enceladus.
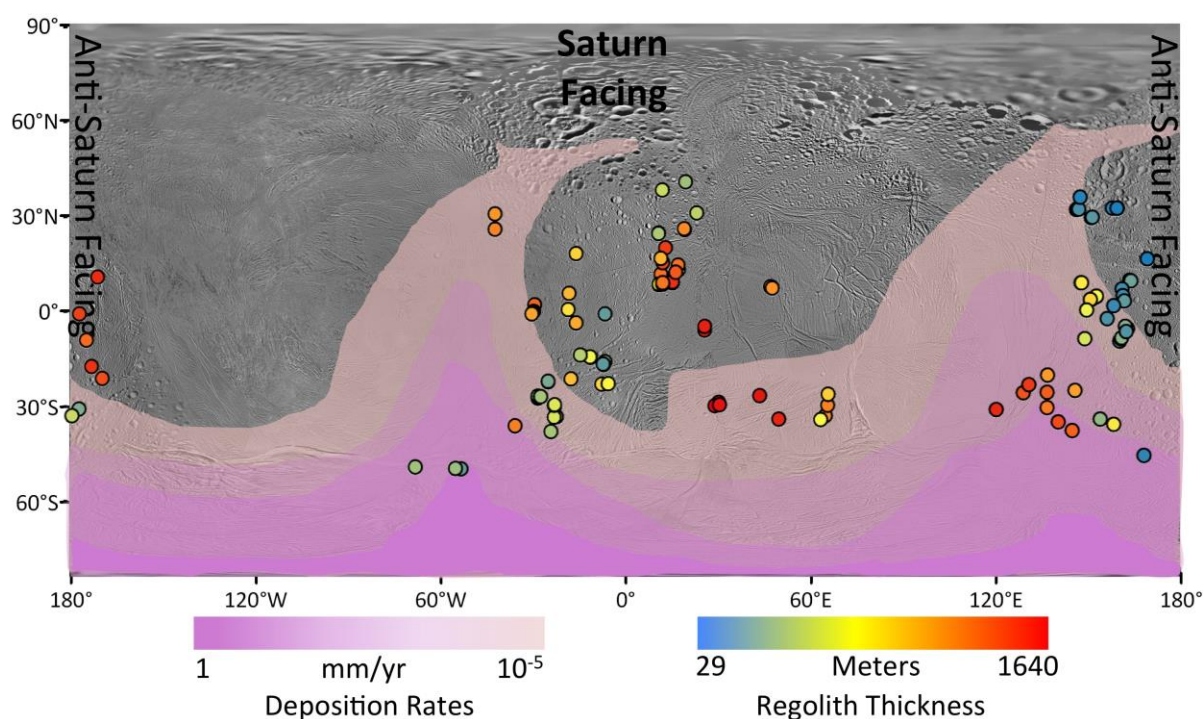
Figure 3.11: Results of regolith thickness from the Slope Angle method are overlaid on the modeled distribution rates of regolith deposition [after *Kempf et al.,* 2010]. The range of deposition rates from the lowest rates of 10^{-5} mm/year in the lightest purple to rates as high as 1 mm/yr in the darkest purple which indicates increasing regolith thicknesses with decreasing distance from the SPT. We find pit chains occurring where models [*Kempf et al.,* 2010] suggest no regolith would likely accumulate. On the anti-Saturn cratered terrains we see a progressive increase of regolith depth with increasing proximity to the SPT, however this relationship does not hold as well for the Saturn facing cratered terrains. Warmer colors indicate lower deposition rates, cooler colors indicate higher deposition rates. The rates of regolith deposition increase with increasing proximity to the south polar terrain.

If regolith accumulation is potentially correlated to plume fall-back (Fig. 3.11), the time frame of regolith deposition must be considered in the context of the likely timescale of the activity of the eruptive jets in the SPT. 153° of ice shell rotation has been interpreted by

Patthoff & Kattenhorn, [2011] for the formation of the paleo-tiger stripes to the present day active tiger stripes. For a similar 1 Myr nonsynchronous rotation period, it would require a 425,000 yrs for the regolith to form. This is less than our estimated 708,000 yrs, but within the same order of magnitude. This indicates that the plume activity within the SPT has likely been active for at least 425,000 yrs feeding regolith to the surface required for the formation of pit chains. However it would be difficult to accumulate as much as 1640 m of regolith within this time frame with even the most optimistic accumulation rates of 1mm/yr [*Kempf et al.,* 2010]. Within the time span of SPT activity, 1640 m of regolith in 425,000 would required deposition rates of 3.8 mm/yr. 1640 m is one of the anomalously high values of measured regolith thickness, and to produce 480 m of regolith would require deposition rates of 1.1 mm/yr. *Kempf et al.* [2010] assumed the density of the fall-back material to be near the density of glacial ice rather which is likely too high: although the regolith is comprised mostly of water [*Waite et al.,* 2006] it is difficult to envision water expelled from individual jets taking on a form other than that of a snow-like material. Thus, it may be that the deposition rates determined from modeling are underestimated, allowing for thicker accumulation of regolith build-up over shorter time periods. This may explain the disparity in the overall regolith thicknesses, but does not address the differences in hemispherical distributions. However, if nonsynchronous rotation is occurring [e.g., *Patthoff & Kattenhorn*, 2011], it would be more likely that the longitudinal distribution of regolith would be more homogenous. The model by *Kempf et al.,* [2010] shows two lobes of regolith accumulation roughly aligned with the cratered terrains. If NSR is occurring it is unlikely that preferential deposition of regolith would occur only on the cratered terrains. If Enceladus's ice shell completed one entire rotation while plume activity occurred, there should be no preferential deposition of regolith.

Regardless of the process or processes by which regolith is produced on Enceladus, the significant thicknesses we estimate have implications for the mantling of surface features such as craters. Craters ≤2 km and ≥6 km appear to be scarce in Enceladus's cratering record [*Kirchoff & Schenk,* 2009] with respect to other Saturnian satellites. Proposed hypotheses for the lack of craters of these sizes include burial by regolith deposition and viscous relaxation of crater-related topography [*Bray et al.,* 2007; *Kirchoff & Schenk,* 2009; *Bland et al.,* 2012]. If we assume a rim to crater floor depth-to-diameter ratio of 0.2 [*Bland et al.,* 2012], it would

require 400 m and 1200 m of regolith to completely eliminate the surface expression of a 2 km crater and a 6 km crater, respectively. Thus deposition of regolith could have resulted in erasing craters ≤2 km in diameter. However, considering that only 12% of our calculated regolith thicknesses exceed 500 m, it is unlikely that regolith deposition can explain the lack of craters >6 km in diameter. It is more likely that regolith deposition is responsible for erasing craters ≤2 km where 400 m of regolith is well within the range of thicknesses. We therefore agree with *Bland et al.* [2012] that it is unlikely that regolith deposition alone can explain the lack of craters of ≥6km, but neither can viscous relaxation even under the most optimistic conditions. Hence, a combination of the two processes may be required to produce the muted crater morphologies observed on Enceladus, with mantling by regolith in the cratered terrains being a young and ongoing process, accompanied by geologically recent tectonic dissection and the formation of pit chains.

Conclusions

We present a global distribution of pit chains across the surface of Enceladus, which exist over a wide range of latitudes and preferentially form within the cratered terrains likely due to a greater presence of regolith in these terrains. Additionally, the present of pit chains mostly in the cratered terrains indicates that there has been recent tectonic activity within the cratered terrains, which are overlooked as being heavily tectonized. We infer the regolith depths across the surface of Enceladus from three techniques, the Average Pit Spacing method, the Assumed Angle of Repose method and the Slope Angle method. We find the Slope Angle method is the most accurate way of calculating regolith thickness. We find that regolith depth varies heterogeneously across Enceladus's surface, ranging from 29-1640 m. Within the anti-Saturn cratered terrains, regolith thicknesses increase with decreasing distance from to the south polar terrain consistent with models regolith deposition and observations of muted crater morphologies. The inferred amount of regolith accumulation is sufficient to explain the dearth of craters ≤2 km in diameter, but significant amounts of viscous relaxation in addition to mantling may be required to explain the lack of ≥6 km diameter craters on Enceladus. The presence of regolith therefore provides evidence for muting surface morphologies and is therefore capable of insulating Enceladus's surface which will likely help constrain models of heat flow.

References

Bart, G. D., R. D. Nickerson, M. T. Lawder, H. J. Melosh, (2011), Global survey of lunar regolith depths from LROC images. *Icarus*, 215, 485-490. Doi: 10.1016/j.icarus.2011.07.017.

Bland, M. T., K. N. Singer, W. B. McKinnon, P. M. Schenk, (2012), Enceladus' extreme heat flux as revealed by its relaxed craters. *Geophys. Res. Lett., 39,* L17204, doi:10.1029/2012GL052736.

Bleamaster, Leslie, F. III and Hansen, V. L. (1994), Effects of crustal heterogeneity on the morphology of Chasmata, Venus. *J. Geophys. Res.*, 109. E02004. Doi:10.1029/2003JE002193.

Bray, V. J., D. E. Smith, E. P. Turtle, J. E. Perry, J. A. Rathbun, A. N. Barnash, P. Helfenstein, C. C. Porco, (2007), Impact crater morphology variations on Enceladus, paper presented at the *38ᵗʰ Lunar and Planetary Science Conference*, Abstract #1873.

Buczkowski, D. L., Barnouin-Jha, O. S., Prockter, L. M. (2008), 433 Eros lineaments: Global mapping and analysis. *Icarus*, 193. 39-52. Doi: 10.1016/j.icarus.2007.06.028.

Buczkowski, D. L., D. Y. Wyricks, K. A. Iyer, E. G. Kahn, J. E. C. Scully, A. Nathues, R. W. Gaskell, T. Roatsch, F. Preusker, P. M. Schenk, L. Le Corre, V. Reddy, R. A. Yingst, S. Mest, D. A. Williams, W. B. Garry, O. S. Barnouin, R. Jaumann, C. A Raymond, C. T. Russell. (2012 a), Large-scale troughs on Vesta: A signature of planetary tectonics. *Geophys. Res. Let.*, Vol. 39, L18205, doi:10.1029/2012GL052959.

Buczkowski, D. L., D. Y. Wyrick, F. Capaccioni, J. E. C. Scully, D. A. Williams, H. Hiesinger, W. B. Garry, R. A. Yingst, L. Le Corre, A. Nathues, P. M. Schenk, R. Jaumann, C. A. Raymond, C. M. Pieters, T. Roatsch, F. Preusker, C. T. Russell. (2012 b), Geologic mapping of the AV-9 Numisia Quadrangle of asteroid 4Vesta, *43ʳᵈ Lunar and Planetary Science Conference*, Abstract # 2263.

Buczkowski, D. L., M. C. DeSanctis, C. A. Raymond, D. Y. Wyrick, E. Ammannito, A. Frigeri, D. Williams, C. T. Russell, (2013), Brumalia Tholus: An Indication of Magmatic Intrusion on Vesta. *44th Lunar and Planetary Science Conference*, Abstract #1996.

Cruikshank, K. M. and A. Aydin, (1995), Unweaving the joints in Entrada Sandstone, Arches National Park, Utah, U.S.A. *J. Struc. Geol.*, 17, 409-421.

Cuffey, K. M. & Paterson, W. S. B. (2010), The physics of Glaciers. Butterworth-Heinemann, Oxford. p-12.

Ferrill, D. A., A. P. Morris, D. Y. Wyrick, D. W. Sims, N. M. Franklin, (2004), Dilational fault slip and pit chain formation on Mars. *GSA Today, 14 (*10), 4-12, doi:10.1130/1052-5173(2004)014<4:DFSAPC>2.0.CO;2.

Ferrill, D. A. Wyrick, D. Y., Smart, K. J. (2008), Coseismic pit crater, normal fault, and extensional fissure formation in unconsolidated sediment and basalt in Northern Iceland. *American Geophysical Union, Fall Meeting.* Abstract #T24A-05.

Ferrill, D. A., D. Y. Wyrick, K. J. Smart, (2011), Coseismic, dilational-fault and extension-fracture related pit chain formation in Iceland: Analog for pit chains on Mars. *Lithosphere,* v. 3, no. 2, 133-142. doi:10.1130/L123.1

Grant, J. V., & Kattenhorn, S. A. (2004), Evolution of vertical faults at an extensional plate boundary, southwest Iceland. *J. Struct. Geol.*, 26, 537-557. doi: 10.1016/j.jsg.2003.07.003.

Hansen, C. J., L. Esposito, A. I. F. Steward, J. Colwell, A. Hendrix, W. Pryor, D. Shemansky, R. West, (2006), Enceladus' water vapor plume. *Science,* 311, 1422-1425. doi:10.1126/science.1121254.

Horstman, K. C., Melosh, H. J. (1989), Drainage pits in cohesionless materials: implications for the surface of Phobos. *J. Geophys. Res.*, 94, 12,433-12,441. doi: 10.1029/JB094iB09p12433.

Kempf, S. Beckmann, U., Schmidt, J. 2010. How the Enceladus dust plume feeds Saturn's E ring. *Icarus*, 206. 446-457. doi: 10.1016/j.icarus.2009.09.016.

Kirchoff, M. R., and P. Schenk, (2009), Crater modification and geologic activity in Enceladus' heavily cratered plains: Evidence from the impact crater distribution, *Icarus*, *202*, 656-668 doi:10.1016/j.icarus.2009.03.034.

Martel, S. J., & Langley, J. S. (2006), Propagation of normal faults to the surface in basalt, Koae fault system, Hawaii. *J. Struct. Geol.*, 28, 2123-2143. doi:10.1016/j.jsg.2005.12.004.

Martin, E. S. and S. A. Kattenhorn (2014), A history of pit chain formation within Enceladus's cratered terrains suggests a nonsynchronous rotation stress field. *45th Lunar and Planetary Science Conferences*, Abstract #1083.

Michaud, R. L., R. T. Pappalardo, and G. C. Collins, (2008), Pit chains on Enceladus: a discussion of their origin, *39th Lunar and Planetary Science Conference*, Abstract #1678.

Nahm, A. L. and S. A. Kattenhorn, (2014), A classification and characterization scheme for tectonic structures on Enceladus. *45th Lunar and Planetary Science Conference*, Abstract #1072.

Okubo, C. H., Martel, S. T. (1998), Pit crater formation on Kilauea volcano, Hawaii. *Journal of Volcanology and Geothermal Research*, 86. 1-18. doi:10.1016/S0377-0273(98)00070-5.

Passey, Q. R., (1983), Viscosity of the lithosphere of Enceladus, *Icarus*, 53, 105-120. doi:10.1016/0019-1035(83)90024-6.

Passey, Q. R., & E. M. Shoemaker, (1982), Craters and basins on Ganymede and Callisto: Morphological indicators of crustal evolution, in *Sattelites of Jupiter,* edited by D. Morrison, pp. 379-434, Univ. of Ariz. Press, Tucson.

Patthoff, D. A., Kattenhorn, S. A. (2011), A fracture history on Enceladus provides evidence for a global ocean. *Geophys. Res. Let.*, 38, L18201. doi:10.1029/2011GL048387.

Porco, C. C., P. Helfenstein, P. C. Thomas, A. P. Ingersoll, J. Wisdom, R. West, G. Neukum, T. Denk, R. Wagner, T. Roatsch, S. Kieffer, E. Turtle, A. McEwen, T. V. Johnson, J. Rathbun, J. Veverka, D. Wilson, J. Perry, J. Spitale, A. Brahic, J. A. Burns, A. D. DelGenio, L. Dones, C. D. Murray, S. Squyres, (2006), Cassini observes the active south pole of Enceladus. *Science*, 311, 1393-1401. doi:10.1126/science.1123013.

Prockter, L., P. Thomas, M. Robinson, J. Joseph, A. Milne, B. Bussey, J. Veverka, A. Cheng (2002), Surface expressions of structural features on Eros. *Icarus*, 155, 75-93. doi:10.1006/icar.2001.6770.

Quaide W. L. and V. R. Oberbeck, (1968), Thickness determinations of the lunar surface layer from lunar impact craters. *J. Geophys. Res.* 73:5247-5270. doi: 10.1029/JB073i016p05247.

Roatsch, Th., Wählisch, M., Giese, B., Hoffmeister, A., Matz, K., -D., Scholten, F., Kuhn, A., Wagner, R., Neukum, G., Helfenstein, P., Porco, C., (2008), High-resolution Enceladus atlas derived from Cassini-ISS images. *Planetary and Space Science*, 56, 109-116.

Roatsch, Th., Jaumann, R., Stephan, K. Thomas, P.C., (2009), Cartographic mapping of the icy satellites using ISS and VIMS data, in *Saturn from Cassini-Huygens*. Springer, Dordrecht. 763-781.

Roatsch, Th., E. Kersten, A. Hoffmeister, M. Wählisch, K.-D. Matz, C. C. Porco, (2013), Recent improvements of the Saturnian satellites atlases: Mimas, Enceladus, and Dione. *Planetary and Space Science*, 77, 118-125. doi:10.1016/j.pss.2012.02.016.

Rowland, J. V., E. Baker, C. J. Ebinger, D. Keir, T. Kidane, J. Biggs, N. Hayward, T. J. Wright, (2007), Fault growth at a nascent slow-spreading ridge: 2005 Dabbahu rifting episode, Afar. *Geophys. J. Int.*, 171, 1226-1246. doi:10.1111/j.1365-246X.2007.03584.x.

Schenk, P. M., E. Asphaug, W. B. McKinnon, H. J. Melosh, P. R. Weissman, (1996), Cometary nuclei and tidal disruption: The geologic record of crater chains on Callisto and Ganymede. *Icarus*, 121, 249-274. doi:10.1006/icar.1996.0084.

Schenk P. M., & J. M. Moore, (2014), Topography of midsized icy satellites 2: Tethys and the effects of Odysseus. *45th Lunar and Planetary Science Conference,* Abstract # 2598.

Smith, B. A., L. Soderblom, R. Batson, P. Bridges, J. Inge, H. Masursky, E. Shoemaker, R. Beebe, J. Boyce, G. Briggs, A. Bunker, S. A. Collins, C. J. Hansen, T. V. Johnson, J. L. Mitchell, R. J. Terrile, A. F. Cook II, J. Cuzzi, J. B. Pollack, G. E. Danielson, A. P. Ingersoll, M. E. Davies, G. E. Hunt, D. Morrison, T. Owen, C. Sagan, J. Veverka, R. Strom, V. E. Suomi, (1982), A new look at the Saturn system: The Voyager 2 images, *Science,* 215, 504-537.

Spencer, J. R., J. C. Pearl, M. Segura, F. M. Flasar, A. Mamoutkine, P. Romani, B. J. Buratti, A. R. Hendrix, L. J. Spilker, R. M. C. Lopes. (2006), Cassini encounters Enceladus: Background and the discovery of a south polar hot spot. *Science,* 311, (5766), 1401-1405. doi:10.1126/science.1121661.

Spitale, J. N and C. C. Porco, (2007), Association of the jets of Enceladus with the warmest regions on its south-polar fractures, *Nature*, 449, 695-697, doi:10.1038/nature06217.

Sullivan, R., Greeley, R., Pappalardo, R., Asphaug, E., Moore, J. M., Morrison, D., Belton, M. J. S., Carr, M., Chapman, C. R., Geissler, P., Greenberg, R., Granahan, J., Head, J. W. III., Kirk, R., McEwen, A., Lee, P., Thomas, P. C., Veverka, J. (1996), Geology of 243 Ida. *Icarus*, 120. 119-139. doi:10.1006/icar.1996.0041.

Thomas, P. Veverka, J., Bloom, A. Duxbury, T. (1979), Grooves on Phobos: Their distribution, morphology and possible origin. *J. Geophys. Res.*, 84. 8457-8477. doi:10.1029/JB084iB14p08457.

Veverka, J., Thomas, P., Simonelli, D., Belton, M.J.S., Carr, M., Chapman, C., Davies, M.E., Greeley, R., Greenberg, R., Head, J., Klaasen, K., Johnson, T.V., Morrison, D., Neukum, G., (1994), Discovery of grooves on Gaspra. *Icarus* 107, 399–411. doi:10.1006/icar.1994.1007.

Waite, J. H., M. R. Combi, W-H., Ip, T. E. Cravens, R. L. McNutt, W. Kasprzak, R. Yelle, J. Luhmann, H. Niemann, D. Gell, B. Magee, G. Fletcher, J. Lunine, W-L, Tseng, (2006), Cassini ion and neutral mass spectrometer: Enceladus plume composition and structure. *Science*, 311, 1419-1422. doi:10.1126/science.1121290.

Wilcox, B. B., M. S. Robinson, P. C. Thomas, B. R. Hawke, (2005), Constraints on the depth and variability of the lunar regolith. *Meteoritics and Planetary Science* 40, Nr 5, 659-710. doi: 10.1111/j.1945-5100.2005.tb00974.x.

Wyrick, D., D. A. Ferrill, A. P. Morris, S. L. Colton, D. W. Sims, (2004), Distribution, morphology, and origins of Martian pit crater chains. *J. Geophys. Res., 109,* E06005, doi:10.1029/2004JE002240.

Wyrick, D. Y., D. L. Buczkowski, L. F. Bleamaster, G. C. Collins. (2010), Pit crater chains across the solar system. *41st Lunar and Planetary Science Conference* Abstract, #1413.

Chapter 4

Global strike-slip fault distribution on Enceladus

Abstract

We present the first global distribution of strike-slip faults on Enceladus. We characterize the distribution of strike-slip faults on Enceladus and find that they can be broken down into three broad categories: tectonic terrain boundaries, reactivated linear features, and primary strike-slip faults. All three types of features are found predominantly within, or within close proximity to, the anti-podal cratered terrains. to explore the driving mechanisms, including the possibility of a global stress field to explain their distribution. We find that most of the strike-slip faults on Enceladus are inconsistent with a global stress field.

4.1 Introduction

Strike-slip faults have played a role in modifying the surfaces of many icy bodies, including Europa [*Hoppa et al.,* 1999; *Kattenhorn,* 2004; *Sarid et al.,* 2002], Ganymede [*Pappalardo et al.,* 1998], Triton [*Croft,* 1993], and Enceladus [*Smith-Konter & Pappalardo,* 2008; *Hurford et al.,* 2007; 2012] (Fig. 1). Strike-slip faults indicate that despite extension being a dominant tectonic process on icy bodies, lateral motion is an important component in the deformation of icy shells. However, only cursory analysis of strike-slip faults has been completed outside of the south polar terrain (SPT) [*Kargel & Pozio,* 1996]; strike-slip faults have been primarily explored within the south polar terrain [*Smith-Konter & Pappalardo,* 2008]. The SPT encompasses the four prominent 'tiger stripes' [*Porco et al.,* 2006], the likely source of the plume activity [*Spitale &* Porco, 2007], and 'paleo' tiger stripes [*Patthoff & Kattenhorn*, 2011] enclosed by the south polar dichotomy. The tiger stripes likely formed within a nonsynchronous rotation stress field [*Patthoff & Kattenhorn,* 2011] and strike-slip motions along the tiger stripes are likely induced by tidal stresses [*Nimmo et al., 2007; Hurford et al.,* 2007] caused by changes in Enceladus's tidal bulge due to its eccentric orbit. Fracture histories preserved in icy shells (including extension fractures and all types of faulting) can be used to identify the stress mechanisms responsible for creating them.
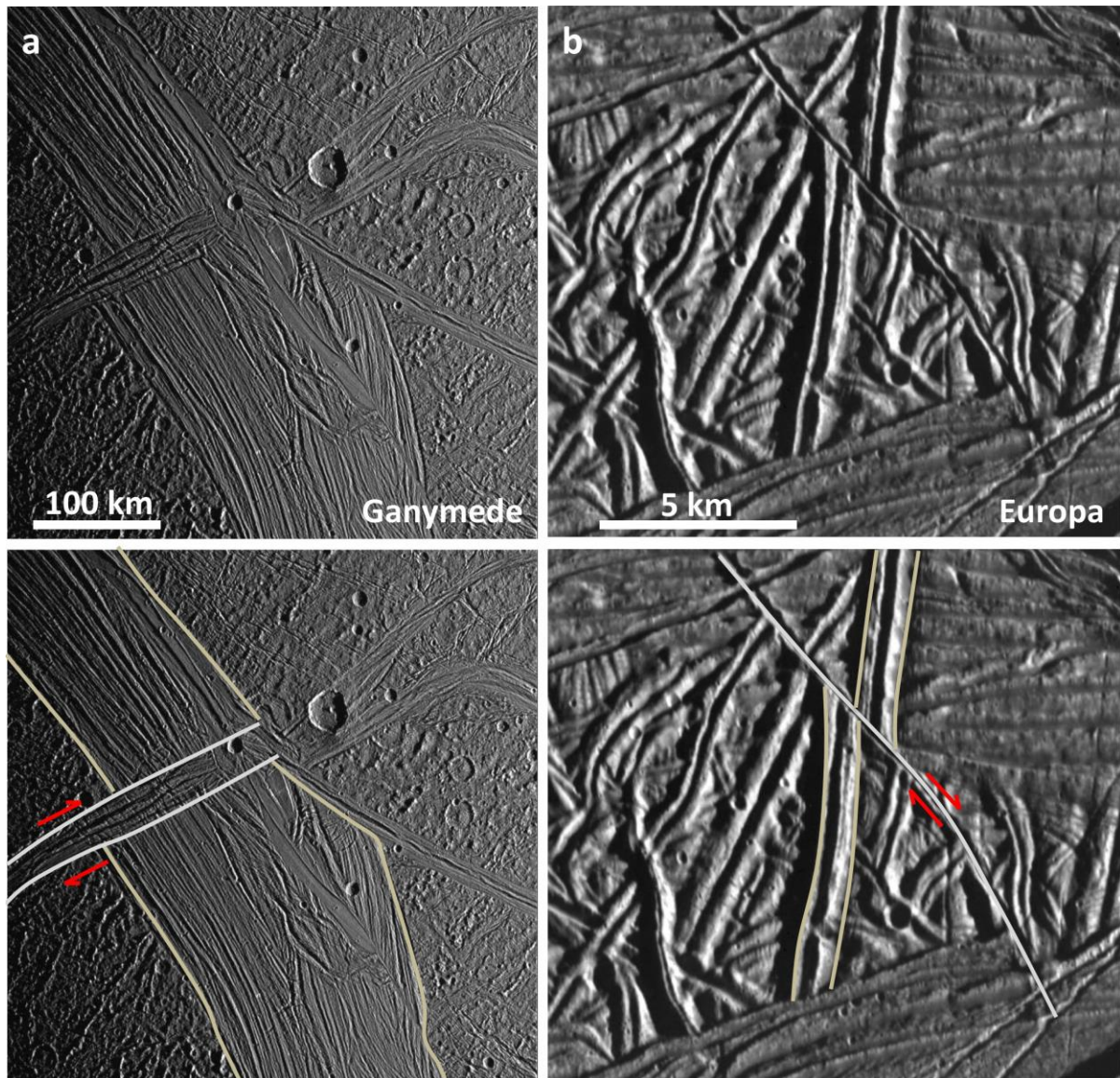
Figure 4.1: Examples of strike-slip faults on a. **Ganymede (Image PIA01619) and** b. **Europa (Image PIA00849), with characteristic lateral offsets.**

Possible driving mechanisms at the global scale include polar wander, despinning, shell volume changes, orbital recession/decay, diurnal tidal factors, nonsynchronous rotation (NSR) [*Kattenhorn & Hurford,* 2009; *Collins et al.,* 2010], obliquity, libration, and precession [*Rhoden et al.,* 2012]. For example, the formation of the fractures within the SPT has been attributed to NSR (which infers a global subsurface ocean) [*Patthoff & Kattenhorn*, 2011], with diurnal tidal stresses inducing daily shearing along the tiger stripes [*Hurford et al.,* 2007] that could result in strike-slip motions. Lateral tectonics are an important

component of the deformation history of Enceladus's ice shell, but have yet to be explored with a perspective beyond the SPT. We aim to characterize strike-slip-faults on Enceladus, many of which appear to be latitudinally extensive with respect to the size of Enceladus, in contrast to similar fracture types on other icy bodies. We illustrate their spatial distribution, and explore whether their development is consistent with the global stress mechanisms suggested to be driving fracture formation and activity within the SPT, or if other processes (including local or regional driving forces) are responsible for their development.

On Europa, strike-slip faults have been used to understand the global stress fields responsible for their development on the surface [*Hoppa et al.,* 1999; *Sarid et al.,* 2002; *Kattenhorn,* 2004; *Rhoden et al.,* 2011]. Analyses of the distribution of strike-slip faults on Europa revealed a prevalence of right-lateral strike-slip faults in the southern hemisphere and predominantly left-lateral strike-slip faults in the northern hemisphere; strike-slip faults in equatorial regions could be either right- or left-lateral [*Hoppa et al.,* 1999]. This pattern was found to be consistent with the process of tidal walking, whereby stresses induced by diurnal tidal forcing, caused by an eccentric orbit, control strike-slip motions based on the sense of shear stresses resolved onto faults of different orientations. Moreover, contemporary diurnal stresses show a longitudinal mismatch between the predicted shearing sense on many strike-slip faults and their observed sense of lateral offset, implying that they were rotated into their current longitudinal positions by NSR subsequent to their initial development [*Hoppa et al.,* 1999]. The inference of NSR on Europa from strike-slip fault patterns is also one of the many lines of evidence that suggests that Europa also has a global subsurface ocean [*Pappalardo et al.,* 1999]. Deviations from this general pattern occur mostly in the equatorial regions of Europa where sense of slip is dictated by fault orientation, but may also be explained by polar wander, obliquity, libration, or precession [*Rhoden et al.,* 2011; 2012; *Rhoden & Hurford,* 2013].

Strike-slip faults are widespread on Enceladus, but their distribution, and the distribution of slip sense has not been previously explored. Strike-slip faults on Enceladus lack the characteristic lateral offsets as on other icy moons (Fig. 4.1). Alternative diagnostic structures typical of strike-slip faults must be relied upon to first identify strike-slip faults and secondly their sense of motion.

4.2 Strike-slip faults

Broadly, strike-slip faults occur when the intermediate tensile stress (σ_2) is vertical with displacement being right- or left-lateral. No net extension or contraction of the crust occurs unless there is an oblique component of motion along the fault. Strike-slip faults can form at both large and small scales in both oceanic and continental crust. On Earth, strike-slip faults can form transform plate boundaries, or may act as linking features between extending terrains like mid-ocean ridges and continental rift zones. Tear faults may form in contractional regimes like fold and thrust belts, near-parallel to the direction of regional displacement. Strike-slip faults will ultimately form in regions where the orientations of the principle stresses favor it.

4.2.1 Tailcracks

Tailcracks (also referred to as wing cracks, kinks, and horsetail fractures [*Cruikshank et al.,* 1991; *Willemese et al.,* 1997]) and anti-cracks are secondary fractures associated with the near-tip regions of strike-slip faults, and can be used to identify the sense of slip of a fault in the absence of visible offsets [*Kattenhorn,* 2004, *Kattenhorn & Marshall,* 2006; *Groenleer & Kattenhorn,* 2008] (Fig. 4.2). Tailcracks are tension cracks that form at the tips of slipping faults due to a concentration of stresses at the fault tip [*Pollard & Aydin,* 1988*; Cruikshank et al.,* 1991] (Fig. 4.2a). The point where the tailcrack and fault plane intersect is defined by the angle θ, called the tailcrack angle, and is theoretically 70.5° if no dilation occurs on the primary fault [*Erdogan & Sih,* 1963; *Lawn & Wilshaw,* 1975; *Pollard & Segall,* 1987]. Deviations from 70.5° can be used to infer the relative amounts of opening and shearing occurring along these faults (Fig. 4.2b). Mode I refers to the motion along an extension fracture (opening), perpendicular to the fracture plane. Modes II and III refer to shearing motion which occurs perpendicular to (mode II) or parallel (mode III) to the fracture plane. *Kattenhorn* [2004] found examples of tailcracks on the icy surface of Europa and used tailcrack geometries (Mode I fractures) to conclude that dilation was a significant concurrent component of motion along many strike-slip faults.
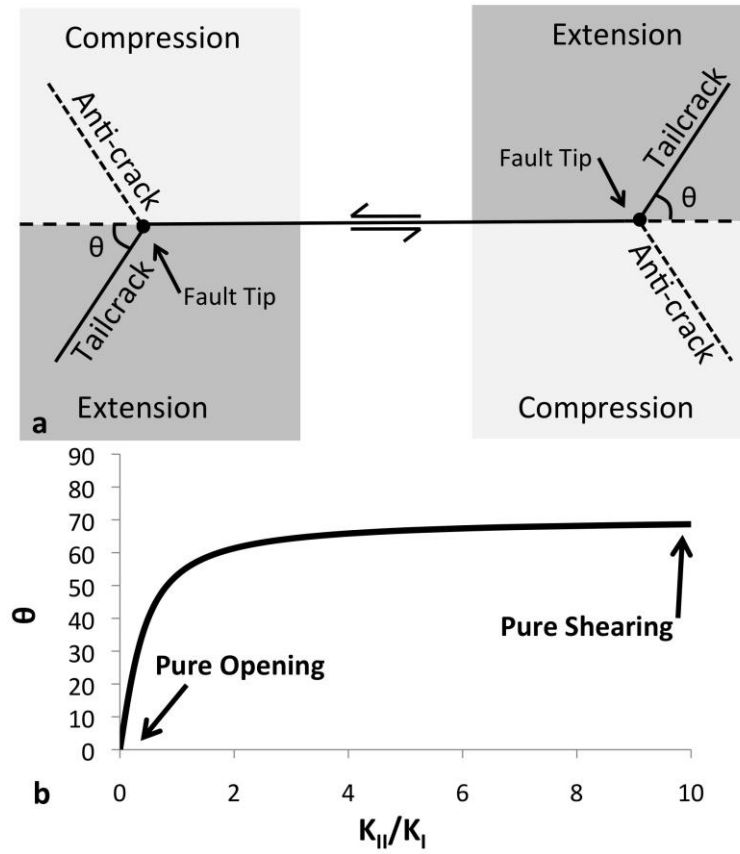
Figure 4.2: a. Tailcracks form due to the concentration of stress at the tip of a fault. Illustrated is a left-lateral strike-slip fault (after Kattenhorn, 2004). Dark gray regions highlight extensional areas where tailcracks may develop; light gray regions represent compressional areas where anti-cracks could form. b. Predicted tailcrack angles relative to fault strike plotted against the relative amounts of concurrent opening and shearing. K_{II}/K_I is the ratio of stress intensity factors of mode-I opening (K_I) and mode-II shearing (K_{II}). The tailcrack angle will approach 70.5° with pure shearing.
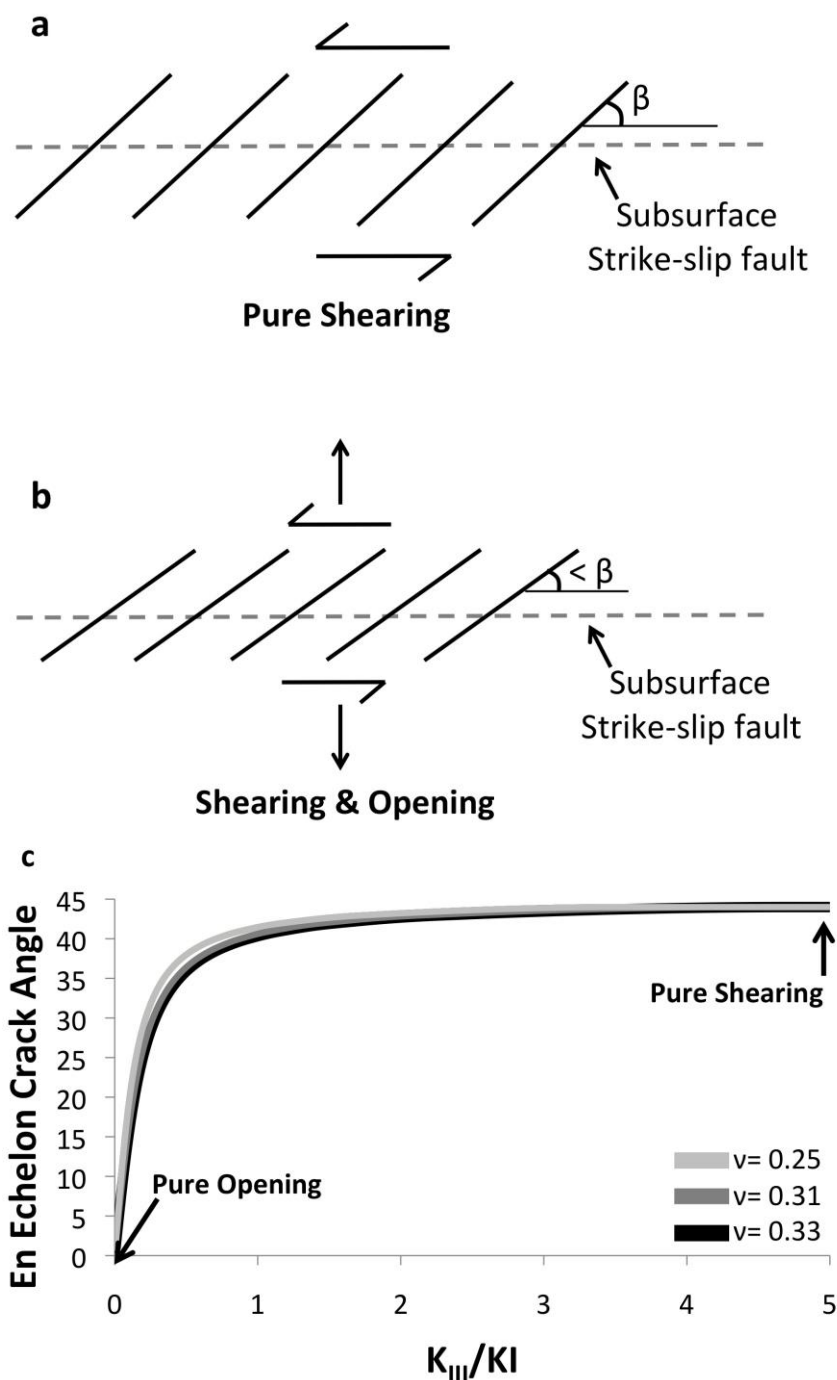
Figure 4.3: a. En echelon cracks form at 45° to the strike of a subsurface strike-slip fault experiencing shearing. b. For a strike-slip fault experiencing a component of opening, the angle of en echelon cracks will be less than 45° [*Olson & Pollard,* 1991; *Cruikshank et al.,* 1991]. c. The en echelon crack angle can be predicted using the K_{III}/K_I ratio of the stress intensity factors of mode-I opening (K_I) and mode-III shearing (K_{III}) [*Pollard et al.,* 1982]. The K_{III}/K_I relies on the Poisson's ratios which for low temperature ice are unknown, but can be estimated shown here, light gray indicates v=0.25, a general value for rock; dark gray is v=0.31 for ice [*Mitri & Showman,* 2008; *Manga &* Wang, 2007]; black is v=0.33 for ice [*Schulson,* 2001]. The Poisson's ratios have relatively little effect on the relationship between K_{III}/K_I and en echelon crack angle.

4.2.2 En echelon cracks

In this work we assume that linear arrangements of en echelon cracks are the surface manifestation of a subsurface strike-slip fault, first noted in experimental work by *Riedel* [1929] and *Cloos* [1955], and commonly observed along terrestrial strike-slip faults. En echelon cracks in particular are on type of a group of fractures called Riedel shears, which are secondary fractures that form in response to underlying shear fractures first recognized by Riedel [1929]. There are a variety of Riedel shears most notably R-shears and R'-shears, conjugate fractures with synthetic and anti-thetic motion respectively. Additionally, synthetic P-shears form at low angles to the parent crack and T-fractures, which are tension fractures that form at 45° to the parent crack; the sense of step of the T-fractures is opposite to the shear direction of the underlying fault. We interpret the en echelon cracks on Enceladus to be T-fractures, thus indicated the presence of a subsurface shear zone. En echelon cracks in this scenario are mode I features. Hence, they form perpendicular to the direction of local maximum horizontal tension (σ_1), and parallel to the local maximum horizontal compression (σ_3). This relationship produces en echelon cracks stepping in the opposite direction from the sense of slip: left-stepping en echelon cracks result from right-lateral strike-slip motion, and right-stepping cracks result from left-lateral motion (Fig. 4.3). En echelon cracks are a particularly useful tool in identifying strike-slip motion in the absence of lateral offsets. Arrays of en echelon cracks have also been observed at the terminations of sheared joints [*Cruikshank & Aydin*, 1995], and can occur as a peripheral breakdown fringe along the edges of a parent crack (e.g., joints, veins, igneous intrusions) in response to a rotation of the principal stresses during the growth process [*Pollard et al.,* 1982; *Sommer,* 1969; *Nicholson & Pollard*, 1985].

If en echelon cracks form above a subsurface shear fracture undergoing purely strike-slip motions, the angle between the trend of the subsurface fault and the echelon crack (the en echelon crack angle) will be 45° [*Ramsey,* 1980; *Olson & Pollard,* 1991] (Fig. 4.3a). A deviation from 45° implies a component of dilation: the en echelon crack angle will be <45° if there is a component of fault-perpendicular tension and dilation (Fig. 4.3b) and > 45° if there is a component of contraction (Fig. 4.3c).

4.3 Strike-slip fault mapping

Mapping was completed on the global mosaic of Enceladus [*Roatsch et al.,* 2013] from the NASA Planetary Data System's (PDS) Imaging Node Planetary Image Atlas. It has a resolution of 110 m/pixel, which is lower than many of the individual images used to create the mosaic. We performed a global survey of strike-slip faults with the exception of the SPT. The low resolution within the north polar region made it difficult to determine the presence of strike-slip faults, however, occasional offsets have been observed within the SPT [*Patthoff & Kattenhorn,* 2011] but were not comparable (image resolutions within the SPT can be as low as <10 meters per pixel) to the scale of strike-slip faulting observed elsewhere on Enceladus and were therefore not included in this work. Therefore, individual images of target locations were retrieved from the PDS and processed using the Integrated Software for Imagers and Spectrometers (ISIS) developed by the United States Geological Survey. Data was then imported into an ArcGIS environment where the combination of the global mosaic and individual high-resolution images (40-200 m/pixel) allowed for the most detailed analysis of strike-slip faults.

Visible offsets are a common way of identifying strike-slip motion in the solar system, and are ubiquitous on Europa [*e.g., Kattenhorn,* 2002, 2004], and in some cases have been used in the SPT to determine relative ages [*Patthoff & Kattenhorn,* 2011]. However, despite myriad crosscutting features observed at <100 m/pixel, no large offsets were identified. Despite the relatively common nature of strike-slip faults characterized by significant lateral offsets on bodies like Ganymede and Europa (Fig. 4.1) it is unlikely that that lack of similar features on Enceladus is a function of image resolution and coverage. This is suggestive of the dominance of the extensional environments characteristic of icy bodies in the out solar system, and perhaps a fundamentally different process driving strike-slip faulting on Enceladus. The absence of visible offsets on Enceladus requires the use of other kinematic indicators, namely tailcracks and en echelon fractures, to identify the presence of strike-slip motion along a fracture and also to determine the sense of slip.
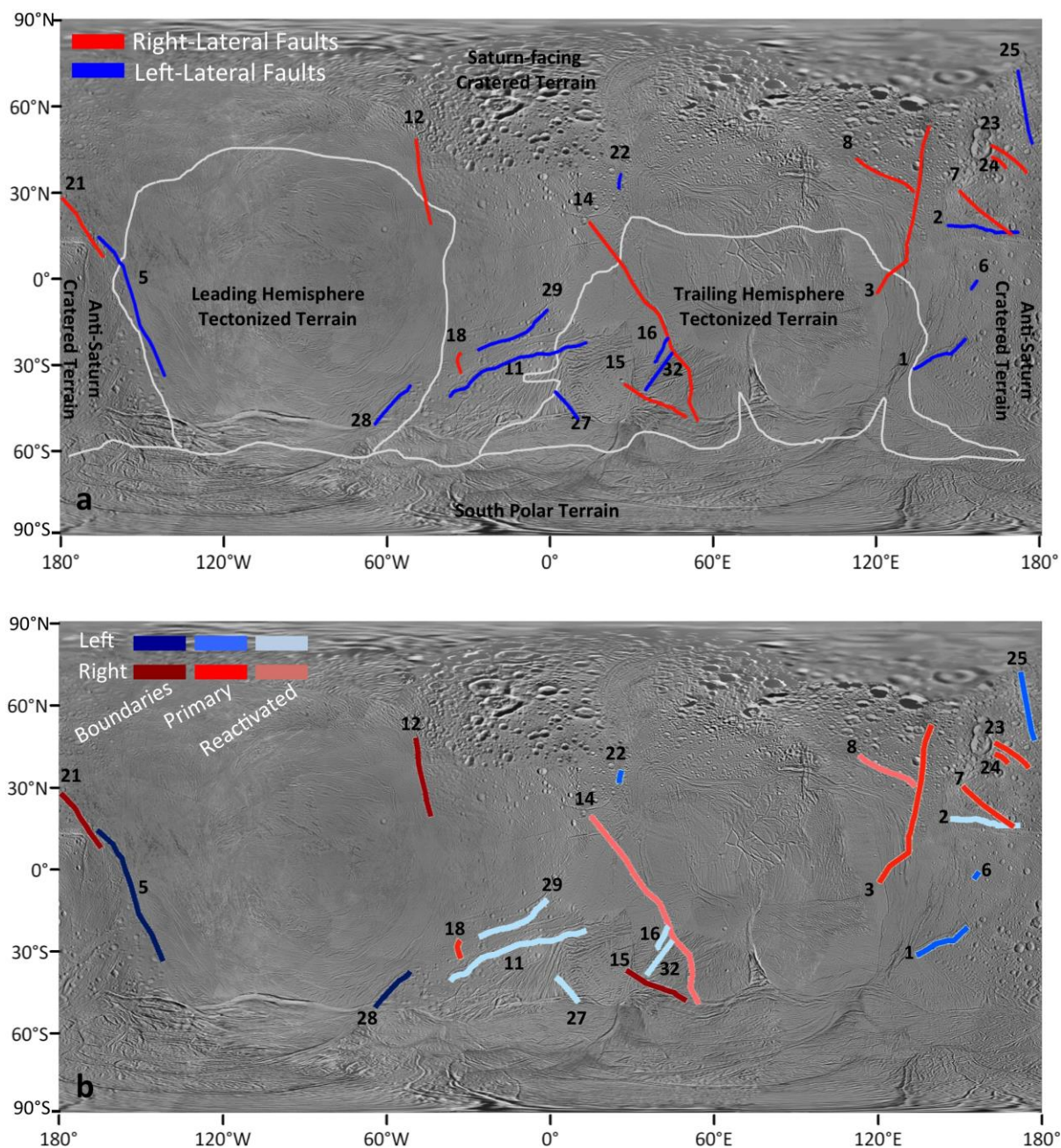
Figure 4.4: The global distribution of strike-slip faults on Enceladus. (a) **Brittle failure of ice Red indicates right-lateral strike-slip faults and blue indicates left-lateral strike-slip faults. Numbers correspond to unique fault identification numbers. Note the dearth of strike-slip faults within the tectonized terrains and the polar regions. Image Credit: NASA/JPL-Caltech/SSI; global mosaic by** *Roatsch et al.*[2013]. (b) **Strike-slip fault distributions: tectonic terrain boundaries (dark tones), primary strike-slip faults (medium tones), and reactivated linear features (light tones). Tectonic terrain boundaries appear on either side of the leading tectonized terrains. Reactivated linear features appear primarily near the south polar dichotomy within the Saturn-side cratered terrains. Primary strike-slip faults appear mostly in the anti-Saturn cratered terrains, mostly north of the equator.**

4.4 Strike-slip fault distribution

Twenty-two individual features were identified globally that could convincingly be characterized as strike-slip faults (Fig. 4.4). Strike-slip faults are located primarily between 120°E and 120°W and between 60°W and 60°W: both regions being composed predominantly of cratered terrains. There is a dearth of strike-slip faults within the tectonized terrains near 90°W and 90°E and within the polar regions north and south of 60°N and 60°S, respectively. The apparent lack of strike-slip faults in the north polar region may be explained, in part, by limited data coverage. The SPT, characterized by the prominent tiger stripes and south polar dichotomy, yielded no discrete strike-slip faults. This does not suggest that the SPT is devoid of shear: previous work has indicated that the tiger stripes may be undergoing strike-slip motions [*Patthoff & Kattenhorn,* 2011; *Hurford et al.,* 2007; 2012]. Additionally, there is no preference for left-lateral vs. right-lateral strike-slip faults in either the northern or southern hemispheres, as has been reported for Europa [*Hoppa et al.,* 1999], nor are there morphologic equivalents of Europa's band-like strike-slip faults [*Kattenhorn,* 2004]. There is no preferential fault orientation or range of lengths.

Based on the 22 mapped strike-slip faults, three different classes of faults were identified: (1) those defining major tectonic domain boundaries, (2) reactivated linear features, and (3) primary strike-slip faults. Tectonic domain boundaries comprise 23% of the strike-slip faults, 36% are reactivated linear features, and 41% are primary strike-slip faults (Fig. 4.4).

4.4.1 Tectonic terrain boundary strike-slip faults

The abrupt boundaries between Enceladus's tectonized and cratered terrains have not been previously investigated in detail. Close examination of these borders reveals sets of en echelon cracks suggestive of shear along a subsurface strike-slip fault. One tectonic terrain boundary (28) (Fig. 4.4) may have a possible tailcrack (Fig. 4.5a). The lack of observed lateral offsets at terrain boundaries is intriguing and perhaps suggests that there is a significant component of dilation occurring along these fractures. We refer to such strike-slip faults as tectonic terrain boundaries (Fig. 4.5). Tectonic terrain boundary strike-slip faults delineate the leading hemisphere tectonized terrain with both left-lateral (5 in Fig. 4.4b) and right-lateral (12 and 21 in Fig. 4.4b) examples. These faults potentially accommodate a broad-scale northward motion of the tectonized terrain they encompass (Fig. 4.4), although

the competing motions of adjacent faults 5 and 21 suggest additional complexity. Two tectonic terrain boundary faults intersect the south polar dichotomy, a left-lateral fault at 60°W (28 in Fig. 4.4b) which lies between the leading tectonized terrain, and Saturn facing cratered terrains and a right-lateral fault (15 in Fig. 4.4b) at 60°E which extends from the south polar dichotomy into the trailing hemisphere tectonized terrains.
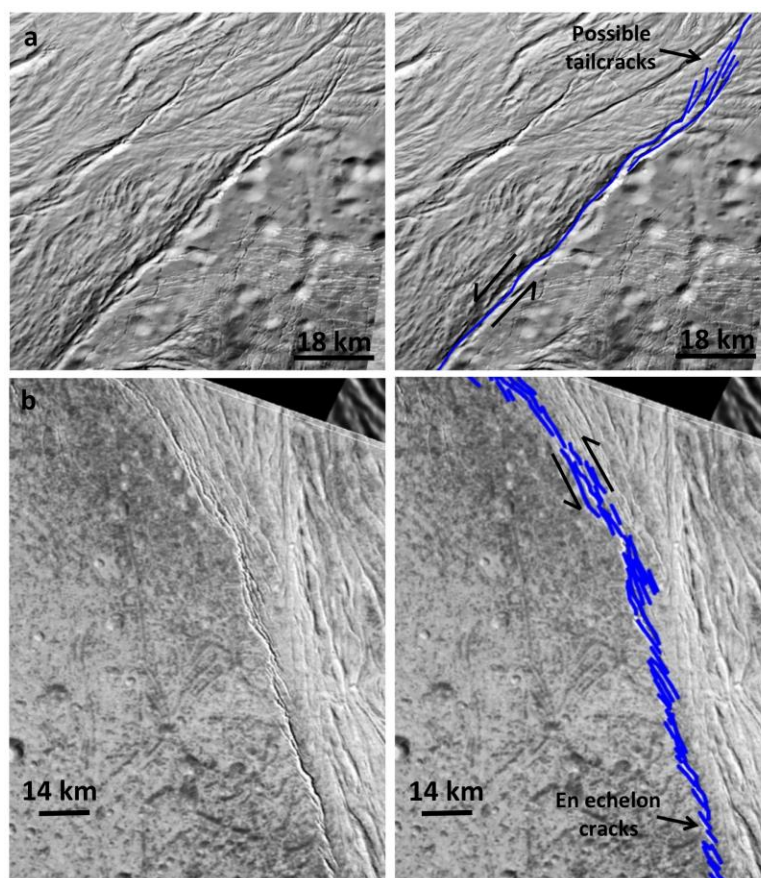
Figure 4.5: Two left-lateral examples of tectonic terrain boundary strike-slip faults on Enceladus. a. A tectonic domain boundary separating cratered terrain from tectonic terrain, centered at 58° W and 44° S (28 in Fig. 4). Image No. N1660434444. b. A tectonic domain boundary centered at 153° W and 6° S (5 in Fig. 4), characterized by a series of en echelon cracks. Image No. N167591706.

4.4.2 Reactivated linear features

A reactivated linear feature is a fracture that experienced shear after its initial formation. Multiple stages of motion likely indicate a changing stress field (Fig. 4.6). As is characteristic of strike-slip faults on Enceladus, reactivated linear features are identified by secondary en echelon cracks or tailcracks due to subsequent shear along a pre-existing fracture. Pre-existing fractures are identified by their relative age with respect to surrounding structures and the amount of displacement accommodated by the fracture(s). Figure 4.6 shows a zone of broad troughs or furrows likely indicating extension (2 in Fig. 4.4) that preceded shear along this feature, resulting in tailcracks on the eastern end of the fracture.

Reactivated linear features are distributed primarily within the cratered terrains. In particular, a high concentration of left-lateral reactivated linear features occur in the southern

hemisphere of Saturn-facing cratered terrains (Fig. 4.4b). Faults 29 and 11 (both left-lateral) are associated with swaths of tectonized terrains crossing deep into the Saturn-facing cratered terrains, and can be traced continuously into the tectonized terrains. This region of left-lateral faults is bounded on the eastern edge by a right-lateral, reactivated fault (14 in Fig. 4.4b), the longest strike-slip fault mapped extending 350 km, comprised of 50-100 km segments. Only two reactivated features occur within close proximity to the anti-Saturn cratered terrains (2 and 8 in Fig. 4.4b).
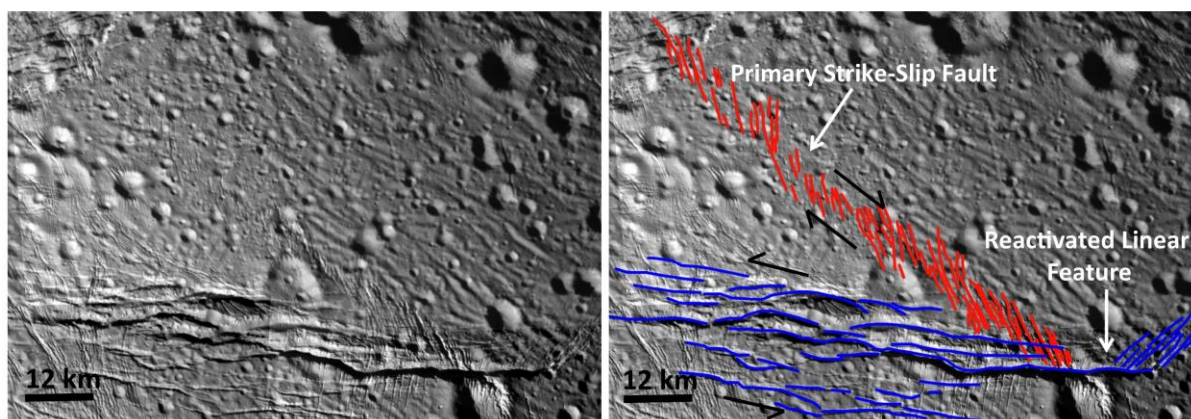
Figure 4.6: Two crosscutting strike-slip faults with kinematic indicators showing an opposite sense of shear. Left-stepping en echelon cracks indicate right-lateral motion on a NW-SE oriented structure. The reactivated linear feature shows tailcracks indicative of left-lateral motion. Centered at 158°E and 17°N. Image No. N1489050254.

4.4.3 Primary strike-slip faults

Primary strike-slip faults are those faults that do not comprise a tectonic domain boundary and do not exhibit signs of forming by the reactivation of a preexisting surface fracture (Fig. 4.7). They initially broke through to the surface as mode I cracks as the result of a subsurface shear fracture, and have not experienced any obvious reversal of sense of slip in the interim. Nonetheless, the classification of this particular style of strike-slip fault is guided only by secondary fractures (en echelon cracks and tailcracks) as the surface manifestation of a subsurface structure. En echelon cracks in particular are interpreted to be T-fractures, which form arrays of opening en echelon cracks as the result of shear motion on a subsurface parent crack. It is possible, however, that these features develop in response to the reactivation of ancient subsurface or heavily mantled faults; however, this cannot be reconciled with the available data sets. Even if reactivation of an inherited crustal fabric is

involved in the development of some of these structures, we nonetheless distinguish them from 'reactivated linear features' to imply that breakthrough to the surface occurred during shearing, as opposed to the shearing of a feature already present at the surface.

Primary strike-slip faults are found within close proximity to both the Saturn- and anti-Saturn cratered terrains. However, the highest concentration of primary strike-slip faults are near the anti-Saturn cratered terrains (Fig. 4.4b), with 7 primary strike slip faults in contrast to the 1 primary strike-slip fault on the Saturn facing cratered terrains. Additionally, the primary strike-slip faults in the anti-Saturn cratered terrains are generally north of the equator in contrast to reactivated primary strike-slip faults, which are predominantly found south of the equator in the Saturn facing cratered terrains. Fault 25 is a left-lateral strike-slip fault that can be traced deep into the north polar regions. The largest being a right-lateral fault that extends from the equator to ~60°N (3 in Fig. 4.4b), and is 270 km long.

Figure 4.7: Primary strike-slip faults. (a) **Strike-slip fault at 145°E, 26°S, characterized by a broad splay of tailcracks. Image No. N1500061771.** (b) **Array of right-stepping, en echelon cracks suggestive of left-lateral subsurface shear at 156°E, 2°S. Image No. N1489050475.**

4.5 Normal and shear stresses along strike-slip faults

The tiger stripes in Enceladus's SPT have been suggested to undergo both shearing and dilation on a diurnal timescale [*Nimmo et al.,* 2007, *Smith-Konter & Pappalardo,* 2008; *Hurford et al.,* 2007; 2012], potentially affecting the timing and duration of plume eruptions from the tiger stripe cracks. It

follows that other tectonic structures on Enceladus may also have experienced components of both shearing and dilation, although not necessarily exclusively in response to diurnal tidal forcing. Secondary features (tailcracks and en echelon cracks) associated with strike-slip faults present the opportunity to measure relative amounts shear and opening that occurred along the fault [*Kattenhorn,* 2004; *Pollard et al.,* 1982]. This ratio (from observations) can be compared with similar ratios generated from models of a global field. We measured either tailcrack angles (θ) or en echelon crack angles (β) (whichever was present) along mapped strike-slip faults on Enceladus in a Mercator projection (which preserves angles), reprojected about the center of each fault, and compared these angles to theoretical predictions based on linear elastic fracture mechanics.

4.5.1 Inferring a normal-vs.-shear stress ratio from observations

Slip along a fracture is dictated by the normal and shear stresses (σ_n and σ_s respectively) which are related to the components of stress and fault orientation by the Mohr equations. As a fault slips, stresses are concentrated at the tips typically creating a radial stress perturbation; if tailcracks form, they will form perpendicular to the direction of the maximum circumferential stress. To be predictive about the tailcrack angle therefore, the circumferential stress must be calculated which is related to the stress intensity factors for opening (K_I) and shearing (K_{II}). The tailcrack angle is related to the ratio of σ_s/σ_n by the maximum circumferential stress criterion [*Erdogan & Sih,* 1963; *Pollard & Segall,* 1987; *Willemse & Pollard*, 1998], and by maximizing the circumferential stress, the tailcrack angle is mathematically related to the ratio of K_{II}/K_I [see *Groenleer & Kattenhorn,* 2008]. Thus for an observed tailcrack angle θ (Fig. 4.2), the ratio of the stress intensity factor K_I, for mode I (opening), and the stress intensity factory for mode II K_{II}, (shearing) K_{II}, can be calculated. A stress intensity factor (K_I, K_{II}, and K_{III}) is the magnitude of a local stress in the vicinity of the fracture tip: K_I, K_{II}, and K_{III} are the measure of the magnitude of mode I, II, or III stress respectively. The ratio of $K_{(II\ or\ III)}/K_I$ represents the ratio of the relative amounts of mode II or III shearing to opening. This is appropriate for tailcracks and en echelon cracks, which are mode I fractures secondary to a primary crack. The parent crack will be shearing, mode II or a mode III motion based on the tipline orientation relative to shearing: tailcracks form relative to a parent crack with a vertical tipline and en echelon cracks form above an

underlying fault with a horizontal tipline. In the case of tailcracks, the primary crack is behaving as mode II and for en echelon cracks, the primary cracks is behaving as mode III. Therefore, to calculate the relative amounts of opening and shearing at tailcracks and en echelon cracks the K_{II}/K_I and K_{III}/K_I ratios are used respectively.

After *Groenleer & Kattenhorn,* [2008]:

$$\frac{K_{II}}{K_I} = \frac{sin\left(\frac{\theta}{2}\right) \times cos\left(\frac{\theta}{2}\right)}{3sin^2\left(\frac{\theta}{2}\right) - 1} \tag{1}$$

where θ is the tailcrack angle.

Similarly, for the case of dilational en echelon surface fractures and a primary crack experiencing a component of dilation, the en echelon crack angle β (Fig. 4.3), can be used to calculate the ratio of K_{III} (the stress intensity factory for mode III shearing) to K_I [*Pollard et al.,* 1982]:

$$\frac{K_{III}}{K_I} = tan(2\beta) \times \left(\frac{1}{2} - v\right) \tag{2}$$

where v is Poisson's ratio.

However, eqn. 2 is only relevant if the normal stress acting on the primary crack is tensile (i.e., experiencing a component of dilation). The K_{II}/K_I and K_{III}/K_I ratios derived from equations (1) and (2) are based on the observed geometries of fractures related to strike-slip faults. Analogous, theoretical ratios of shear to normal motion can be calculated from modeled stress fields to determine if predictions can be reconciled with observations. The observed K_{II}/K_I and K_{III}/K_I ratios can be compared to the theoretical σ_s/σ_n because they all relate the relative quantities of shear and normal motion along a given fault. In a tension positive sign convention, K_{III}/K_I implies the normal stress is positive, and can be compared to the σ_s/σ_n if the absolute value of the shear stress is used because it is not known a priori if the parent crack is dilating. Additionally for the σ_s/σ_n, a positive ratio does not always imply that the normal stress is tensile and this must be verified in order to make a direct comparison between K_{III}/K_I and σ_s/σ_n. A negative normal stress indicates a compressive stress, which

would require the Riedel Shear Zone Criteria to determine if the observed en echelon cracks match other expected geometries for the sense of shear like R, R', or P shears [*e.g., Riedel,* 1929]. The global distribution of strike-slip faults on Europa has been attributed to a global stress field related to tidal distortion of the ice shell above a liquid ocean [*Hoppa et al.,* 1999]. The fracture patterns and geologic activity within the south polar terrains of Enceladus have been previously documented to be the compatible with formation due to stresses induced by both NSR and diurnal tidal deformation [*Patthoff & Kattenhorn,* 2011]. Calculated diurnal stresses in the SPT do not exceed ~80 kPa [*Smith-Konter & Pappalardo,* 2008], which are not sufficient to overcome the tensile strength of ice, potentially in the range ~1-3 MPa [*Schulson & Duvall,* 2009]. Additionally, fractures that form as the result of diurnal stresses are likely to be arcuate like cycloids on Europa [*Marshall & Kattenhorn,* 2005; *Groenleer & Kattenhorn,* 2008] which are not observed suggesting that diurnal stresses are not a major driving force in the initiation of fractures on Enceladus. Outside the SPT where the ice shell is likely thicker, diurnal stresses are even lower, <10 kPa (Martin & Kattenhorn, 2014), and so are even less likely to create fractures in the ice shell. Nonetheless, such stresses may potentially cause motion along pre-existing fractures, as has been suggested for controlling the timing of jet activity in the SPT (*Hurford et al., 2007; 2012*).

4.5.2 Inferring a normal-vs.-shear stress ratio from stress models

The fracture patterns, including the tiger stripes, preserved within the SPT are suggested to have been created within a NSR stress field [*Patthoff & Kattenhorn,* 2011], and motions along the tiger stripes have been attributed to diurnal tidal stresses [*Nimmo et al.,* 2007, *Smith-Konter & Pappalardo,* 2008; *Hurford et al.,* 2007; 2012]. Both NSR and diurnal tides produce global-scale stress fields which would likely produce other fracture patterns that may be preserved outside of the SPT. *Martin & Kattenhorn,* [2014] demonstrate that the global distribution of pit chains across Enceladus is consistent with a NSR stress field. The magnitude of diurnal tidal stresses is unlikely to exceed ~80 kPa [*Smith-Konter & Pappalardo,* 2008], therefore we assess the global distribution of strike-slip faults within the context of a NSR stress field. SatStressGUI [*Kay & Kattenhorn,* 2010] based on SatStress, an open source program for calculating global stresses in the ice shell of a tidally-deforming moon [*Wahr et al.,* 2009], can be used to calculate global stress fields due to diurnal tides or

NSR. Similarly, SatStressGUI can be used to assess the likelihood that diurnal tidal stresses are driving shearing along pre-existing faults, or whether motion is consistent with the tidal walking model suggested for strike-slip faults on Europa [*Hoppa et al.,* 1999]. The program uses a 4-layer model to represent the satellite interior, comprising upper and lower ice shells, an inner layer we assume to be a global subsurface ocean, and a rocky core. We used the point calculation function within SatStressGUI to determine the stress tensor at a chosen coordinate (the location of a strike-slip fault). Given no absolute knowledge of the NSR characteristics of the ice shell, we select a hypothetical NSR period of 1 Myr, which allows sufficient stress to accrue to enable fracturing, prior to the viscoelastic relaxation of such stresses [*Kay*, 2010]. Additionally, we select rheological parameters for low temperature ice (Table 4.1) for each of the four layers: the upper and lower ice shell, an assumed global ocean, and a core. For each layer, a density, shear modulus, Lamé Parameter, viscosity, Young's Modulus, and Poisson's Ratio are assigned.

Table 4.1: Parameters used to calculate point stresses at Enceladus's surface using SatStressGUI [*Wahr et al.*, 2009; *Kay & Kattenhorn*, 2010]. ρ is density, G is the shear modulus, λ is the Lamé Parameter, η is the viscosity, E is Young's Modulus, and ν is Poisson's Ratio. Rheological properties consistent with previous work [*Olgin et al.,* 2011; *Smith-Konter & Pappalardo* 2008; *Nimmo et al.,* 2007]

	$\rho(kg/m^3)$	G (Pa)	λ (Pa)	Thickness	η (Pa·s)	E	ν (Pa)
Upper Ice Shell	917	3.5×10^9	6.8×10^9	$2 \times 10^3 - 8 \times 10^3$	1×10^{23}	9.3107×10^9	3.301×10^{-1}
Lower Ice Shell	917	3.5×10^9	6.8×10^9	$2.2 \times 10^4 - 7.8 \times 10^4$	1×10^{17}	9.3107×10^9	3.301×10^{-1}
Ocean	1000	-	2×10^9	$1 \times 10^4 - 7.2 \times 10^4$	-	-	-
Core	3500	1×10^{12}	4×10^{10}	1.56×10^5	-	-	-

After building a satellite in SatStressGUI, the stress mechanism (NSR and/or diurnal), and period are selected. SatStressGUI adopts a tension positive sign convention. Using the point calculator function, for a given fault location, σ_1, σ_3, and a variable α (the orientation of σ_1 measured clockwise form due north (0°)) were calculated. The Mohr equations relate the magnitude of the principal stresses (from SatStressGUI) to resolve the amount of normal (σ_n) and shear (σ_s) stress on the fault.

$$\sigma_n = \frac{\sigma_1 + \sigma_3}{2} + \frac{\sigma_1 - \sigma_3}{2} cos(2\Theta) \tag{3}$$

$$\sigma_s = \frac{\sigma_1 - \sigma_3}{2} sin(2\Theta) \tag{4}$$

Θ is the angle between α and the normal vector to the fault. We compare the ratio σ_s/σ_n from a modeled NSR stress field with the K_{II}/K_I and K_{III}/K_I ratios from observations to determine if a theoretical ratio matches ratios inferred from observations. If a match occurs, it suggests that an NSR stress field could have formed the strike-slip fault in that orientation. The point in the NSR stress field where the theoretical ratios match the inferred ratios indicates a longitude, in the NSR stress field where the observed amounts of opening and shearing are achieved. We then determine the likelihood that the strike-slip fault in its current orientation could have formed at that longitude with the observed sense of slip. A match in slip-sense would indicate that that strike-slip fault is consistent with forming as a result of NSR stresses.

4.5.3 Strike-slip faults in the context of an NSR stress field

For each fault where en echelon crack or tailcrack angles were measured, the theoretical σ_s/σ_n ratio (at 15 different longitudes spread out over 180° of the NSR stress field) was compared with the observed K_{II}/K_I or K_{III}/K_I ratios. If there was a longitude at which the observed ratio matched the theoretical ratio, the sense of slip the fault would experience at that location was verified. If the sense of slip was consisted with what was observed, that fault was deemed to be consistent with formation in an NSR stress field. If the sense of slip did not match observations, the fault was deemed inconsistent with formation due to an NSR stress field. Faults 1 and 2 (Fig. 4.4) are consistent with formation in an NSR stress field (Table 2) (Fig. 4.8); both their observed and theoretical ratios of shear to normal motion are similar. Similarly, Fault 1 is a primary strike slip fault located in the southwestern region of the anti-Saturn cratered terrains. Fault 2 is a reactivated linear feature located in the northwest regions of the anti-Saturn cratered terrains. Both 1 and 2 are roughly oriented E-W and indicate left-lateral motion. For fault 1, $\sigma_s/\sigma_n = -0.6$ and $K_{II}/K_I = -0.82$ at a longitude of $-81.18°$ in the NSR stress field (Fig. 4.8) would produce left-lateral motion, consistent with the observed slip sense. Fault 2 had an observed $K_{II}/K_I = -0.69$ and $\sigma_s/\sigma_n = -0.39$ at an NSR longitude of $-65.65°$, consistent with the observed left-lateral motion. With the exception of fault 2, reactivated linear features are inconsistent with formation in an NSR stress field as

evidenced by the wrong slip-sense at the NSR longitude where $\sigma_s/\sigma_n = K_{II}/K_I$. For the same reason, tectonic terrain boundaries and some primary strike-slip faults (3 and 7). Despite having theoretical and observed rations of shearing and normal stress on the fault, if the fault will not slip with the observed slip sense, it could not have formed in that location. Faults 6 and 18 cannot be matched with an NSR longitude and corresponding σ_s/σ_n consistent with the inferred K_{III}/K_I for these faults. Faults 7 and 29 appear twice each as there were two longitudes in the NSR stress field where the σ_s/σ_n were similar to the $K_{II(I)}/K_I$.

Table 4.2: A summary of the results from observed en echelon crack and tailcrack angles. Each fault has an assigned identification number (Fig. 4), and was delineated by type of strike-slip fault. The NSR longitude is the point in the NSR stress field where the theoretical σ_s/σ_n for that particular fault orientation is approximately equal to $K_{II(I)}/K_I$ or K_{III}/K_I deduced from en echelon or tailcrack geometries. The observed slip sense is that indicated by secondary fractures (en echelon cracks and tailcracks) whereas the NSR slip sense is that dictated by the sign of the shear stress that resolves onto the fault when placed in the theoretical NSR stress field at the indicated NSR longitude. Faults highlighted in gray indicate faults whose sense of slip is consistent with a NSR stress field. Faults 7 and 29 appear twice, as there were two longitudes within the NSR stress field were the observed ratios of shear to opening matched the theoretical ratios.

|		Fault ID	Type	NSR Long.	Center Lat.	Crack Angle	Obs. Slip Sense	NSR Slip Sense	$\frac{\sigma_s}{\sigma_n}$	$\frac{K_{II}}{K_I}$	$\frac{K_{III}}{K_I}$
Secondary Crack Types	Tail-crack	1	Primary	-81.18	-26.5	50°	Left	Left	-0.6	-0.82	-
		2	Reactivated	-65.65	17.51	47°	Left	Left	-0.39	-0.69	-
		3	Primary	-91.24	21.91	45°	Right	Left	-0.70	-0.63	
		28	Boundary	46.79	-43.58	19°	Left	Right	-0.30	-0.18	-
	En Echelon crack	5	Boundary	-17.4	-8.6	28°	Left	Right	0.46	-	0.25
		6	Primary	-	-2.15	12°	Left	-	-	-	0.07
		7	Primary	159.87	22.57	32°	Right	Left	0.34	-	0.35
		7	Primary	-20.13	22.57	32°	Right	Left	0.34	-	0.35
		8	Reactivated	170.13	35.85	28°	Right	Left	0.25	-	0.25
		18	Primary	-	-29.21	40°	Right	-	-	-	0.96
		21	Boundary	-36.86	18.2	29°	Right	Left	0.35	-	0.27
		27	Reactivated	53.71	-43.82	16°	Left	Right	0.13	-	0.11
		29	Reactivated	167.25	-20.14	17°	Left	Right	0.13	-	0.11
		29	Reactivated	-12.25	-20.14	17°	Left	Right	0.13	-	0.11
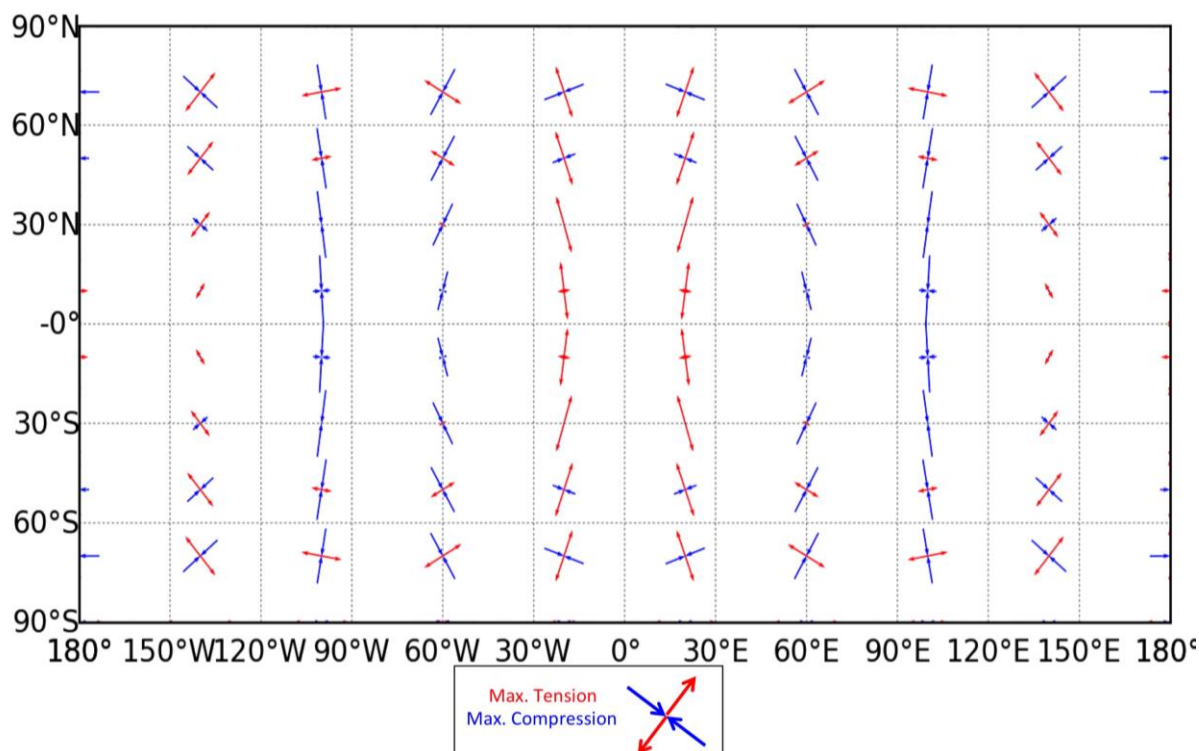
Figure 4.8: A sample NSR stress field for Enceladus produced in SatStressGUI [*Kay & Kattenhorn,* 2010; *Whar et al.,* 2009] with a 1 Myr period. Ticks represent the orientation of the principal stresses: red is maximum tension and blue is maximum compression.

4.6 Discussion

The spatial distribution of the three different strike-slip fault types identified on Enceladus does not appear random (Fig. 4.4). There are few strike-slip faults within the tectonized terrains. There are examples of strike-slip faults that partially cross into the tectonized terrains, but they are always closely associated with a terrain boundary. Some faults within the tectonized terrains (fault 3 & 14) have a broad latitudinal extent perhaps suggesting that something other than a global stress mechanism is controlling that formation: in the case of an NSR stress field, strike-slip faults that cross several lines of longitude would be expect to change their sense of slip. The lack of strike-slip faults within the tectonized terrains may be an indication of some large-scale crustal thickness difference between the terrain types, or simply an issue of the image resolutions in the tectonized terrains. Close examination of high-resolution images within the tectonized terrains did not reveal even small-scale strike-slip structures. The global distribution of strike-slip faults may therefore

indicate some kind of difference in mechanical behavior between terrain types (such as ice shell thickness or inherited crustal weaknesses).

While we consider the role NSR plays in the distribution of strike-slip faults on Enceladus, there are additional mechanisms that are capable of producing global scale stress fields including polar wander, diurnal tidal stresses (tidal walking model [*Hoppa et al.,* 1999]), despinning, orbital recession, internal differentiation, and ice shell thickening [*Kattenhorn & Hurford,* 2009; *Collins et al.,* 2010]. The global distribution of strike-slip faults on Europa have been attributed to the tidal walking model [*Hoppa et al.,* 1999], where faults undergo a ratcheting motion as the orientations of the principal stresses and their magnitudes undergo a 180° of rotation during one orbit. This model will also produce predominantly left-lateral strike-slip faults in the northern hemisphere and right-lateral strike-slip faults in the southern hemisphere [*Hoppa et al.,* 1999]. Not only is this pattern not observed on Enceladus, it cannot explain long strike-slip faults with a consistent sense of slip: fault 14 (350 km long) crosses the equator where it would be expected to changes its sense of slip which is not observed.

The tidal walking model may explain the general distribution of Europa's strike-slip faults, however *Kattenhorn* [2004] found that only band-like strike-slip faults appeared to match the tidal walking model. Polar wander and obliquity have been explored has also been suggested as a possible mechanism for forming the distribution of strike-slip faults on Europa [*Rhoden et al.,* 2011; 2012]. On Enceladus, polar wander has been suggested to be the likely explanation for the location of the SPT [*Nimmo & Pappalardo,* 2006]. If the reorientation of the SPT to the south pole was the same event that induced the geologic activity of this terrain, then this event may have occurred less than 1 Mya [*Patthoff & Kattenhorn,* 2011]. If the strike-slip faults on Enceladus were associated with this reorientation event, it would follow that initiation of strike-slip faulting was also recent. This is consistent with observations of strike-slip faults on Enceladus which appear to crosscut many surrounding features, and many of the en echelon cracks and tailcracks are features called pit chains which are found to be some of the youngest features on the surface [*Martin & Kattenhorn,* 2013]. Polar wander can likely produce stresses up to 10 MPa [*Nimmo & Pappalardo*, 2006; *Melosh,* 1980]. *Matsuyama & Nimmo*, [2008] explored the stress fields produced by various amounts of reorientation and found that regions of shearing would occur in the present day

cratered terrains. Further work is necessary to determine whether the orientations of observed strike-slip faults and their sense of slip are consistent with predicted orientations.

By definition, tectonic terrain boundaries are located at the boundaries between disparate terrains; however, this type of fault appears to occur only on the leading hemisphere (21, 5, 28, and 12), and very near the Saturn-facing portion of the south polar dichotomy (15). It is likely that fault 5 extends far into the northern hemisphere. The opposing sense of slip of these bounding faults (12 and 5) could be an indication that this portions of Enceladus's ice shell in the leading hemisphere are moving northward in a rigid plate-like manner, suggesting large-scale motion of the brittle portion of the ice shell. This motion is perpendicular to the orientation of the current tiger stripes suggesting that the opening of the tiger stripes is in-part driving northward motion of the leading hemisphere tectonized terrains. The funiscular or 'ropy' terrains [*Spencer et al.,* 2009] are comprised of short wavelength, sub-parallel features interpreted to be folds [*Spencer et al.,* 2009; *Barr & Preuss,* 2010; *Bland & McKinnon,* 2014] between the tiger stripes in the SPT. If the funiscular terrains are the result of compression due to opening along the tiger stripe it may also drive the leading hemisphere tectonized terrains northward, consistent with the observed tectonic terrain boundary strike-slip faults.

A closer look at the K_{III}/K_I ratios reveals that all but three are less than 0.35, which correspond to en echelon crack angles between 12° and 29°. This suggests that perhaps these en echelon cracks, rather than being Riedel T-fractures which typically form at 45° to the parent crack may be low angle R-shears (which form synthetic to the parent crack) or P-shears which typically form at 15°-20° synthetic to the parent crack. The are no indications that these en echelon crack arrays have undergone any shear motion and is why they were interpreted to be T-fractures. However, the lack of lateral offsets indicative of shear along these crack arrays, may be a factor of image resolution and the lack of pre-existing structures to be offset.

While the generally antipodal nature of their global distribution is similar to that of the global distribution of features called pit chains, pit chains are likely forming in response to NSR stresses [*Martin & Kattenhorn*, 2014]. The more important commonality between pit chains and strike-slip faults appears to be the antipodal locations of cratered terrains in which they predominantly form. The dearth of both feature types in the tectonized terrains cannot

be ruled out as being an observational problem (features may be difficult to see in the highly disrupted tectonized terrains), or is perhaps related to thicker regolith deposits in the cratered terrains [*Martin & Kattenhorn,* 2013], within which surface cracks related to strike-slip shearing may be more readily apparent. Hence, despite the spatial distribution similarity with pit chains, there appears to be some mechanism(s) other than NSR responsible for the formation, orientations, and reactivation of many (but not necessarily all) strike-slip faults on Enceladus. This result contrasts with the results of strike-slip fault analysis on Europa, which suggest that the global distribution of strike-slip faults is consistent with the tidal walking model driven by tidal stresses [*Hoppa et al.,* 1999; *Kattenhorn,* 2004]. In part both the tidal walking model [*Hoppa et al.,* 1999] and analysis of band-like faults suggest that dilation is a significant component of motion along these strike-slip faults on Europa [*Kattenhorn,* 2004]. Similarly, we find that dilation along strike-slip faults on Enceladus is a common component of motion. Alternative global stress contributors that may be important for strike-slip faults on Europa include changes in spin pole direction and obliquity [*Rhoden et al.,* 2011; 2012].

The lack of continuity between the global distribution of strike-slip faults on Enceladus with a global stress field suggests that perhaps a more regional stress field or regional perturbation to a global stress field may be a better match to the distribution. Regional perturbations to a global stress field may occur for many reasons, in much the same way stress concentrations occur at the tips of a strike-slip fault to produce tailcracks. An inherited crustal fabric, or motion along a nearby fault may be sufficient to perturb a remote stress field. An example of this may be Fault 2 is which is identified as a reactivated linear feature and is consistent with having formed in response to an NSR stress field (Fig. 4.4; Table 2). It is closely associated with fault 7, a primary strike-slip fault that is not consistent with having formed in response to NSR. The close proximity of fault 2 and & 7 suggest that perhaps It might be possible to reconcile this apparent discrepancy by considering whether fault 2 either during its initial formation, or during its reactivation, was locally capable of perturbing the global stress field. Strike-slip faults on Earth have been shown to locally perturb a stress field causing slip along neighboring faults [*Stein et al.,* 1992]. The 1992 Landers earthquake in California likely changed the stress field around the San Andreas fault system [*Stein et al.,* 1992] affect motion around surrounding faults. Similarly, tectonic terrain boundaries shown

here to be characterized by en echelon cracks or tailcracks indicative of shear may produce perturbations to a global or a regional stress field.

The fracture patterns and geologic activity within the south polar terrains have been previously documented to be the result of stresses induced by both NSR and diurnal tidal deformation [*Patthoff & Kattenhorn,* 2011]. As these same mechanisms are the main control on strike-slip fault patterns on Europa, the lack of a match between strike-slip patterns on Europa and Enceladus is intriguing. *Kattenhorn* [2004] noted that only band-like strike-slip faults followed the tidal walking model presented for Europa [*Hoppa et al.,* 1999], and that ridge-like strike-slip faults are the result of another stress mechanism. Similarly, the pattern of strike-slip faults on Enceladus suggests a different stress mechanism, or combination of mechanisms is required to produce the observed distributions.

There are therefore a variety of local and global mechanisms that might be controlling the distribution of strike-slip faults on Enceladus. It is especially intriguing that the pattern of strike-slip faults is dissimilar to that on Europa, and inconsistent with diurnal and NSR stress fields, as these two global stress mechanisms have been attributed to the formation of the fracture patterns with the SPT, and the global distribution of pit chains. Therefore the distribution of strike-slip faults on Enceladus is evidence for additional mechanism(s) modifying Enceladus's surface, which require further exploration to reveal.

Conclusions

Strike-slip faults on Enceladus lack the characteristic lateral offsets, which are typical of strike-slip faults on other icy bodies like Ganymede and Europa. Strike-slip faults on Enceladus are characterized by en echelon cracks and tailcracks indicative of strike-slip motion on a subsurface fault. Therefore, we use secondary fractures, tailcracks and en echelon cracks, to identify strike-slip faults on Enceladus, and produce the first ever global map of strike-slip fault distributions on Enceladus. We find that strike-slip faults fall into three separate classes: tectonic domain boundaries, reactivated linear features, and primary strike-slip faults and are found primarily within the cratered terrains on the Saturn-facing and anti-Saturn hemispheres. Global patterns of strike-slip faults on Europa have been attributed to a global stress field. Previous geologic evidence for NSR suggests the presence of a global stress field. We therefore test the consistency of the distribution of strike-slip faults on

Enceladus with a NSR stress field. We find that in general, the global distribution of strike-slip faults is inconsistent with formation within an NSR stress field. The tidal walking model proposed for Europa is also an unlikely global stress mechanism, however polar wander is a candidate that warrants further exploration. Alternative mechanisms for producing the observed distribution might also include localized perturbations of the remote field generated by near-by features. Additionally, the three strike-slip fault types identified may be indicative of formation due to different stress mechanisms: the strike-slip faults bounding the leading hemisphere tectonized terrains suggest northward movement of the ice shell which is perpendicular to the orientation of the present day tiger stripes.

Acknowledgments

References

Barr, A. C. & L. J. Preuss, (2010), On the origin of south polar folds on Enceladus. *Icarus*, 499-503. doi:10.1016/j.icarus.2010.03.038.

Bland, M. T., & W. B. McKinnon, (2014), Constraining the heat flux between Enceladus' Tiger Stripes: Numerical modeling of funiscular plains formation. *Lunar Planetary Science Conference,* Abstract #2079.

Cloos, E., (1955), Experimental analysis of fracture patterns. *Bull. Geol. Soc. Am.* 66, 241-258. doi:10.1130/0016-7606(1955)66[241:EAOFP]2.0.CO;2.

Collins, G. C., W. B. McKinnon, J. M. Moore, F. Nimmo, R. T. Pappalardo, L. M. Prockter, P. M. Schenk, (2010), Tectonics of the outer planet satellites, in *Solar System Tectonics* (T. Watters and R. Schultz, eds.), Cambridge University Press.

Croft, S. K., J. S. Kargel, R. L. Kirk, J. M. Moore, P. M. Schenk, R. G. Strom, (1993), The Geology of Trition, in *Neptune and Triton* (D. P. Cruikshank, eds.), University of Arizona Press, 879-947.

Cruikshank, K.M., G. Zhao, A. M. Johnson, (1991), Analysis of minor fractures associated with joints and faulted joints. *J. Struct. Geol.* 13, 865–886. doi:10.1016/0191-8141(91)90083-U.

Cruikshank, K. M., & A. Aydin, (1995), Unweaving the joints in Entrada Sandstone, Arches National Park, Utah. *J. Struct. Geol.* 17, 3, 409-421. doi:10.1016/0191-8141(94)00061-4.

Erdogan, F., and C. G. Sih, (1963), On the crack extension in plates under plane loading and transverse shear. *J. Bas. Eng.*, 85, 519-527. doi:10.1115/1.3656897.

Figueredo, P. H., and R. Greeley, (2000), Geologic mapping of the northern leading hemisphere of Europa from Galileo solid-state imaging data, *J. Geophys. Res.* 105, 22,629-22,646. doi:10.1029/1999JE001107.

Groenleer, J. M., and S. A. Kattenhorn, (2008), Cycloid crack sequences on Europa: Relationship to stress history and constraints on growth mechanics based on cusp angles. *Icarus,* 193, 158-181. doi:10.1016/j.icarus.2007.08.032.

Hoppa, G., B. R. Tufts, R. Greenberg, P. Geissler, (1999), Strike-slip faults on Europa: Global shear patterns driven by tidal stress. *Icarus*, 141, 287-298. doi:10.1006/icar.1999.6185.

Hurford, T. A., P. Helfenstein, G. V. Hoppa, R. Greenberg, B. G. Bills, (2007), Eruptions arising from tidally controlled periodic openings of rifts on Enceladus. *Nature*, 447. 293-294. doi:10.1038/nature05821.

Hurford, T. A., P. Helfenstein, J. N. Spitale, (2012), Tidal control of jet eruptions on Enceladus as observed by Cassini ISS between 2005 and 2007. *Icarus*, 220, 896-903, doi:10.1016/j.icarus2010.06.022.

Kattenhorn, S. A., (2002), Nonsynchronous rotation evidence and fracture history in the Bright Plains region, Europa. *Icarus*, 157, 490-506. doi:10.1006/icar.2002.6825.

Kattenhorn, S. A., (2004), Strike-slip fault evolution on Europa: evidence from tailcrack geometries. *Icarus* 172, 582-602. doi:10.1016/j.icarus.2004.07.005.

Kattenhorn, S. A., and S. T. Marshall, (2006), Fault-induced perturbed stress fields and associated tensile and compressive deformation at fault tips in the ice shell of Europa: implications for fault mechanics. *J. Struc. Geol.* 28, 2204-2221. doi:10.1016/j.jsg.2005.11.010.

Kattenhorn, S. A. and T. A. Hurford, (2009), Tectonics of Europa. *In*: Europa, Pappalardo, R. T., McKinnon, W. B., Khurana, K., eds, University of Arizona Press, 199-236.

Kay, J. P., (2010), The case for recent tectonic activity on Jupiter's moon Europa. Moscow, ID: Unpublished masters thesis.

Lawn, B. R., & T. R. Wilshaw, (1975), Fracture of Brittle Solids. New York; Cambridge University Press.

Manga, M., and C.-Y. Wang, (2007), Pressurized oceans and the eruption of liquid water on Europa and Enceladus. *Geophys. Res. Let.,* 34, L07202. doi:10.1029/2007GL029297.

Marshall, S. T., and S. A. Kattenhorn, (2005), A revised model for cycloid growth mechanics on Europa: Evidence from surface morphologies and geometries. *Icarus*, 177, 397-412.

Martin, E. S. and S. A. Kattenhorn, (2013), Estimating regolith thickness on Enceladus using the angle of repose of individual pits within pit chains. *Geological Society of America Abstracts with Programs*, 45, 7, p.704, Paper #305-4.

Martin, E. S. and S. A. Kattenhorn, (2014), A history of pit chain formation within Enceladus's cratered terrains suggests a nonsynchronous rotation stress field. *45th Lunar and Planetary Science Conferences*, Abstract #1083.

Matsuyama, I., and F. Nimmo, (2008), Tectonic patterns on reoriented and despun planetary bodies. *Icarus*, 195, 459-473. doi:10.1016/j.icarus.2007.12.003.

Melosh, H. J., (1980), Tectonic patterns on a reoriented planet: Mars. *Icarus,* 44, 3, 745-751. doi:10.1016/0019-1035(80)90121-4.

Mitri, G. and A. P. Showman, (2008), A model for the temperature-dependence of tidal dissipation in convective plumes on icy satellites: Implications for Europa and Enceladus. *Icarus*, 195, 758-764.

Nicholson, R., and D. D. Pollard, (1985), Dilation and linkage of echelon cracks, *J. Struct. Geolg*. 7, 5, 583-590.

Nimmo, F., and R. T. Pappalardo, (2006), Diapir-induced reorientation of Saturn's moon Enceladus. *Nature,* 441, 614-616. doi:10.1038/nature04821.

Nimmo, F., J. R., Spencer, R. T. Pappalardo, M. E. Mullen, (2007), Shear heating as the origin of the plumes and heat flux on Enceladus. *Nature*, 447, 289-291. doi:10.1038/nature05783.

Olgin, J. G., B. R. Smith-Konter, R. T. Pappalardo, (2011), Limits of Enceladus's ice shell thickness from tidally driven tiger stripe shear failure. *Geophys Res. Let.,* 38, L02201. doi:10.1029/2010GL044950.

Olson, J. E., & D. D. Pollard, (1991), The initiation and growth of en echelon veins. *J. Struct. Geolg*. 13, 5, 595-608. doi:10.1016/0191-814(91)90046-L.

Pappalardo, R. T., J. W. Head, G. C. Collins, R. L. Kirk, G. Neukum, J. Oberst, B. Giese, R. Greeley, C. R. Chapman, P. Helfenstein, J. M. Moore, A. McEwen, B. R. Tufts, D. A. Senske, H. H. Berneman, K. Klaasen, (1998), Grooved terrain on Ganymede: First results from 8 Galileo high-resolution imaging, *Icarus,* 135, 276-302. doi:10.1006/icar.1998.5966.

Patthoff, D. A., & S. K. Kattenhorn, (2011), A fracture history on Enceladus provides evidence for a global ocean. *Geophys. Res. Let.*, 38, L18201. doi:10.1029/2011GL048387.

Patthoff, D. A., (2013), Tectonic history of the south polar terrain of Saturn's moon Enceladus and evidence for a global ocean. (Unpublished doctoral dissertation). University of Idaho, Moscow, ID.

Pollard D. D., P. Segall, P. Delaney, (1982), Formation and interpretation of dilatant echelon cracks. *Bull. Geol. Soc. Am.* 93, 1291-1303. doi:10.1130/0016-7606(1982)93<1291:FAIODE>2.0.CO;2.

Pollard, D. D., & A. Aydin, (1988), Progress in understanding jointing over the past century. *Geol. Soc. Am. Bull.* 100, 1181-1204. doi:10.1130/0016-7606(1988)100<1181:PIUJOT>2.3.CO;2.

Pollard, D. D., and P. Segall, (1987), Theoretical displacements and stresses near fractures in rock: with applications to faults, joints, veins, dikes, and solution surfaces. *In,* Fracture mechanics of rock, B. K., Atkinson eds. Academic Press, London. 277-349.

Porco, C. C., P. Helfenstein, P. C. Thomas, A. P. Ingersoll, J. Wisdom, R. West, G. Neukum, T. Denk, R. Wagner, T. Roatsch, S. Kieffer, E. Turtle, A. McEwen, T. V. Johnson, J. Rathbun, J. Veverka, D. Wilson, J. Perry, J. Spitale, A. Brahic, J. A. Burns, A. D. DelGenio, L. Dones, C. D. Murray, S. Squyres, (2006), Cassini observes the active south pole of Enceladus. *Science*, 311, 1393-1401. doi:10.1126/science.1123013.

Ramsay, J. G., (1980), The crack-seal mechanism of rock deformation. *Nature,* 284, 135-139. doi:10.1038/284135aO.

Riedel, W., (1929), Zur mechanic geologischer Brucherscheinungen (Ein Beitrag zum Problem der Fiederspatten). *Zentbl. Miner. Geol. Paläeont. Abh.* B, 354-368.

Rhoden, A. R., T. A. Hurford, M. Manga, (2011), Strike-slip fault patterns on Europa: Obliquity or polar wander? *Icarus*, 211. 636-647. doi:10.1016/j.icarus.2010.11.002.

Rhoden, A. R., G. Wurman, M. Manga, E. M. Huff, T. A. Hurford, (2012), Shell tectonics: a mechanical model for strike-slip displacement on Europa. *Icarus*, 218 (1), 297-307. doi:10.1016/j.icarus.2011.12.015.

Rhoden, R. R., and T. A. Hurford, (2013), Lineament azimuths on Europa: Implications for obliquity and non-synchronous rotation. *Icarus*, 226, 841-859. doi:10.1016/j.icarus.2013.06.029.

Roatsch, Th., E. Kersten, A. Hoffmeister, M. Wählisch, K.-D. Matz, C. C. Porco, (2013), Recent improvements of the Saturnian satellites atlases: Mimas, Enceladus, and Dione. *Planetary and Space Science*, 77, 118-125. doi:10.1016/j.pss.2012.02.016.

Sarid, A.R., R. Greenberg, G. V. Hoppa, T. A. Hurford, B. R. Tufts, P. Geissler, (2002), Polar wander and surface convergence of Europa's ice shell: Evidence from a survey of strike-slip displacement. *Icarus,* 158, 24–41. doi:10.1006/icar.2002.6873.

Schulson, E. M., (2001), Brittle failure of Ice, *Eng. Fract. Mech.,* 68, 1839-1887. doi:10.1016/S0013-7944(01)00037-6.

Schulson, E. M., and P. Duvall, (2009), Creep and Fracture of Ice, 416 pp., Cambridge Univ. Press, Cambridge, U. K, doi:10.1017/CBO9780511581397.

Smith-Konter, B., and R. T. Pappalardo, (2008), Tidally driven stress accumulation and shear failure of Enceladus's tiger stripes. *Icarus*, 198, 435-451. doi:10.1016/j.icarus.2008.07.005.

Sommer, E., (1969), Formation of fracture lances in glass. *Engng Fract. Mech.* 1, 539-546. doi:10.1016/0013-7944(69)90010-1.

Spencer, J. R., A. C. Barr, L. W. Esposito, P. Helfenstein, A. P. Ingersoll, R. Jaumann, C. P. McKay, F. Nimmo, J. H. Waite, (2009), Enceladus: An active cryovolcanic satellite. In: Saturn after Cassini-Huygens. Springer, New York, pp. 683-722.

Spitale, J. N., and C. C. Porco, (2007), Association of the jets of Enceladus with the warmest regions on its south-polar fractures. *Nature*, 449, 695-697. doi:10.1038/nature06217.

Stein, R. S., G. C. P. King, and J. Lin, (1992), Change in failure stress on the southern San Andreas fault system caused by the 1992 Magnitude=7.4 Landers earthquake. *Science*, 258, 1328-1332. doi:10.1126/science.258.5086.1328.

Wahr, J., Z. A. Selvens, M. E. Mullen, A. C. Barr, G. C. Collins, M. M. Selvans, R. T. Pappalardo, (2009), Modeling stresses on satellites due to nonsynchronous rotation and orbital eccentricity using gravitational potential theory. *Icarus, 200(1)*, 188-206, doi:10.1016/j.icarus.2008.11.002.

Willemse, E. J. M., D. C. P. Peacock, A. Aydin, (1997), Nucleation and growth of strike-slip faults in limestone from Somerset, U.K.. *J. Struct. Geol*. 19, 1461-1477. doi:10.1016/S0191-814(97)00056-4.